

Optimization of the time response of Gas Electron Multiplier detectors

Jan Eysermans

Supervisor: Dr. Michael Tytgat

Counsellor: Sinem Salva

Master's dissertation submitted in order to obtain the academic degree of
Master of Science in Engineering Physics

WE05

Chairman: Prof. dr. Dirk Ryckbosch

Faculty of Engineering and Architecture

Academic year 2013-2014



Optimization of the time response of Gas Electron Multiplier detectors

Jan Eysermans

Supervisor: Dr. Michael Tytgat

Counsellor: Sinem Salva

Master's dissertation submitted in order to obtain the academic degree of
Master of Science in Engineering Physics

WE05

Chairman: Prof. dr. Dirk Ryckbosch

Faculty of Engineering and Architecture

Academic year 2013-2014



Acknowledgments

Writing this master thesis means the end of five years of education and the start of a new story. Many people were involved during this project and the past years which I would now like to thank.

First of all, I would like to thank Michael Tytgat for the opportunity to work on this subject, the support during the past year and the discussions in the office. Furthermore I would like to thank Marcello Maggi for his email support and the discussions at CERN. Although not directly involved with this master thesis, I would like to thank the people at CERN, Nicolas, Gabriella and Isabel. I have gained a lot of knowledge and skills during my stays at CERN and during the many meetings we had this year.

Special thanks to my family and friends:

Eerst en vooral zou ik mijn ouders willen bedanken voor hun onafgebroken ondersteuning en de vrijheid die ze me gegeven hebben doorheen al de jaren. Zonder enige twijfel wil ik ook mijn naaste familie bedanken, Ann, Iris, Inne, Serge en Wim (Louis, Pauline en Ernest included). Ook Eline wil ik heel hard bedanken voor de steun tijdens de voorbije jaren en tijdens de drukke studeerperioden. Tenslotte wil ik ook mijn medestudenten bedanken voor de interessante gesprekken en de leuke momenten van de afgelopen jaren.

Reprints and permissions

The author(s) gives (give) permission to make this master dissertation available for consultation and to copy parts of this master dissertation for personal use. In the case of any other use, the limitations of the copyright have to be respected, in particular with regard to the obligation to state expressly the source when quoting results from this master dissertation.

Synopsis

Title

Optimization of the time response of Gas Electron Multiplier detectors

Author

Jan Eysermans

Promotor

dr. Michael Tytgat

Mentors

Sinem Salva

Abstract

The recently developed Gas Electron Multiplier (GEM) is a promising gaseous particle detector which is proposed for the upgrade of the Compact Muon Solenoid (CMS) at the CERN Large Hadron Collider. Due to its excellent rate capabilities, radiation resistance and the capability to operate in high magnetic fields, it can cope with the expected high radiation environment in the CMS forward region during the high luminosity phase of the collider. In this paper, the time response of GEM detectors is studied using simulations. A method is developed to compare the timing properties of different gas mixtures and is applied to different GEM configurations.

Keywords

GEM, time resolution, Garfield++, CMS

Optimization of the time response of Gas Electron Multiplier detectors

Jan Eysermans

Supervisor: Michael Tytgat

Abstract—The recently developed Gas Electron Multiplier (GEM) is a promising gaseous particle detector which is proposed for the upgrade of the Compact Muon Solenoid (CMS) at the CERN Large Hadron Collider. Due to its excellent rate capabilities, radiation resistance and the capability to operate in high magnetic fields, it can cope with the expected high radiation environment in the CMS forward region during the high luminosity phase of the collider. In this paper, the time response of GEM detectors is studied using simulations. A method is developed to compare the timing properties of different gas mixtures and is applied to different GEM configurations.

Index Terms—GEM, time resolution, Garfield++, CMS

I. INTRODUCTION

As a member of the Micro-Pattern Gas Detector (MPGD) family, the Gas Electron Multiplier (GEM) is the latest development in this category. It can cope with high particle rates up to several tens of kHz/cm², an excellent spatial resolution in the order of 100 μm can be obtained together with a time resolution of 5 ns. Because of its radiation resistance and the capability to operate in high magnetic fields, the GEM was proposed for the upgrade of the muon system in the Compact Muon Solenoid (CMS), one of the four main experiments at the CERN Large Hadron Collider (LHC) [1]. The upgrade will be performed during the Long Shutdown 2 (LS2) in 2018–2019 and comprises the installation of new detectors in the high η-region. Due to the LHC luminosity upgrade during LS2, high particle fluxes are expected in this high η-region and GEM detectors were proposed for the upgrade installation.

In this paper, the time characteristics of GEM detectors is investigated through simulations. The purpose is to investigate and optimize the time resolution, preferably without greenhouse gases. After introducing the GEM detector, we report general simulation results on a single GEM with a standard gas mixture of Ar–CO₂. Afterwards, the timing characteristics are investigated and the uncertainties are explained leading to the definition of the time resolution. From this discussion, an algorithm

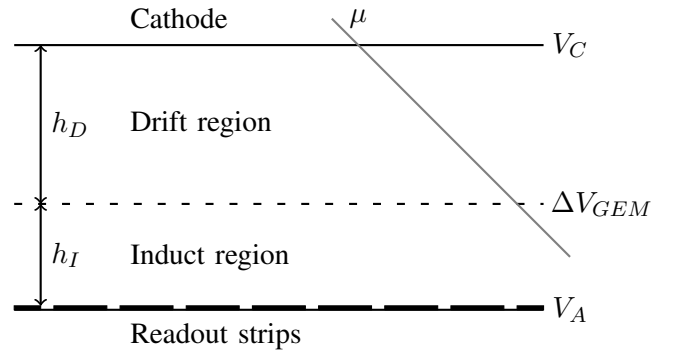


Fig. 1. Cross section of a single GEM detector with readout strips. An incident muon ionizes the gas in the drift region producing primary electrons which drift to the GEM holes.

is developed to search for an optimal gas mixture and the optimization of the GEM voltages and dimensions. This method will be applied on different gas mixtures and GEM configurations.

Several programs were used to simulate the GEM detector. ANSYS Inc. was used to calculate the electrostatic field (potential) and to define the GEM geometry. The solution can be imported in Garfield++, which simulates the primary ionization, charge transport and signal creation. This software package combines different standalone programs such as HEED and Magboltz for the simulation of the primary ionization and charge transport respectively. Finally, ROOT was used to analyze the results. To work efficiently with these programs, a local simulation environment was set up which acts as an interface between the different software packages.

II. THE GAS ELECTRON MULTIPLIER

The GEM detector was developed by F. Sauli in 1997 at CERN [2]. A cross sectional diagram of a single GEM is shown in Fig. 1. A GEM foil is located between two parallel plates, the cathode and the anode respectively. The volume in between is filled with gas. The upper volume is called the drift region and its thickness h_D is typically a few mm. The lower volume, the induction

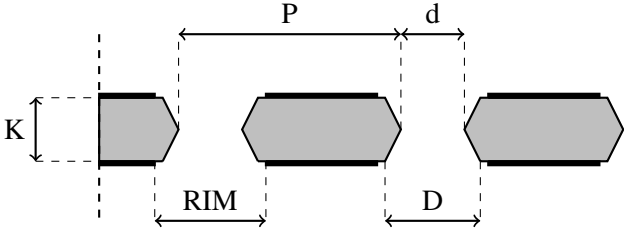


Fig. 2. Cross section of the GEM foil with holes and $5 \mu\text{m}$ coated electrodes (in black). Typical dimensions are $P = 140 \mu\text{m}$, $K = 50 \mu\text{m}$, $\text{RIM} = 70 \mu\text{m}$, $D = 70 \mu\text{m}$ and $d = 50 \mu\text{m}$.

region has a thickness h_I which is typically one or two mm. The GEM foil, the characteristic element of this type of detector, is made of a thin insulating polymer (kapton) coated with copper on both sides. Circular holes are perforated in the foil with a density of 50 to 100 holes mm^{-2} . The cross section of such a foil is shown in Fig. 2 and the common dimensions are listed in the caption. The holes are conically shaped due to the manufacturing process. A high voltage is applied on the anode, cathode and both GEM foil electrodes resulting in a strong electric field up to 100 kV/cm in the holes due to its small thickness. The electric field in the drift and induction region is typically 3–8 kV/cm.

When a charged particle passes through the detector, the gas becomes ionized in the vicinity of its path in the drift region. The generated primary and secondary electrons drift towards the GEM holes according to the electric field lines where an avalanche process will develop due to the high electric field. The avalanche electrons drift towards the anode and a signal will be induced during their drift time. The hole can be regarded as a single amplification channel with a gain depending on the applied GEM voltage and the gas mixture. Because some field lines in the hole terminates on the kapton or on the GEM foil electrodes, it is possible that electrons generated in the avalanche will be trapped in the kapton layer or captured on the GEM foil electrodes. As a result, the gain will be lower and the effective gain is defined as a fraction of the total gas gain G , i.e. $G_{\text{eff}} = \xi G$.

The gain can be increased by inserting multiple GEM foils in the gas volume. For n GEM foils installed, n GEM potentials must be defined as well as $n - 1$ intermediate potentials between the GEM foils. These regions between the foils are called the transfer regions. If equal voltages are applied over the GEM foils and the drift, transfer and induction voltages are approximately equal, the gain can be calculated in first order with a power law: $G_{\text{tot}} = G^n$, with G the (effective) gain of one GEM layer and n the amount of layers installed.

III. SINGLE GEM SIMULATIONS

A single GEM detector is used to discuss general simulation results. The dimensions are listed in Table I. A gas mixture of Ar–CO₂ is used with a composition of 75–25% at standard temperature and pressure (STP, i.e. $p = 1 \text{ atm}$ and $T = 293.15 \text{ K}$). Muons with an energy of 100 GeV are perpendicularly incident on the detector. In order to increase the statistics, the simulation has been repeated over 100 iterations.

TABLE I
SINGLE GEM DIMENSIONS AND ELECTROSTATICS.

h_T	2 mm	d	$55 \mu\text{m}$
h_I	1 mm	D	$85 \mu\text{m}$
P	$140 \mu\text{m}$	RIM	$85 \mu\text{m}$
K	$50 \mu\text{m}$	Metal	$5 \mu\text{m}$
V_{drift}	270 V	E_{drift}	1.35 kV/cm
V_{induct}	400 V	E_{induct}	4 kV/cm
V_{GEM}	460 V	E_{GEM}	92 kV/cm

A. Primary ionization

From the theory of primary ionization, the amount of clusters over a track length L is described by a Poisson distribution with mean L/λ . The parameter λ^{-1} is the cluster density, i.e. the amount of clusters per unit length, and depends on the gas mixture, the charged particle and its energy. For Ar–CO₂ (75–25), the cluster density is equal to 37.78 cm^{-1} , yielding a mean amount of clusters of 7.556. The simulated cluster distribution is shown in Fig. 3 (top) and is fitted to a Poisson distribution. A mean of 7.66 is observed which is in close agreement with the calculated value. To increase the efficiency and optimize the time resolution, the cluster density must be as high as possible (see section IV).

B. Townsend avalanche and gain

In Fig. 3 (bottom), the avalanche size for each primary electron is plotted and fitted to a Polya distribution which describes the gain fluctuations in avalanche processes. The mean μ of this distribution is equal to the gas gain G and depends on the GEM voltage V_{GEM} and the gas mixture via the Townsend coefficient α . The effective gain can be calculated as the fraction ξ of electrons which drift towards the anode and is equal to $\xi = 0.40484$. Hence, the effective gain is calculated as $G_{\text{eff}} = \xi G = 69.31$.

The spread of the electrons on the anode is a measure for the spatial resolution and an RMS of $120 \mu\text{m}$ is found in both directions in the transverse plane. This proves the excellent spatial resolution of GEM detectors.

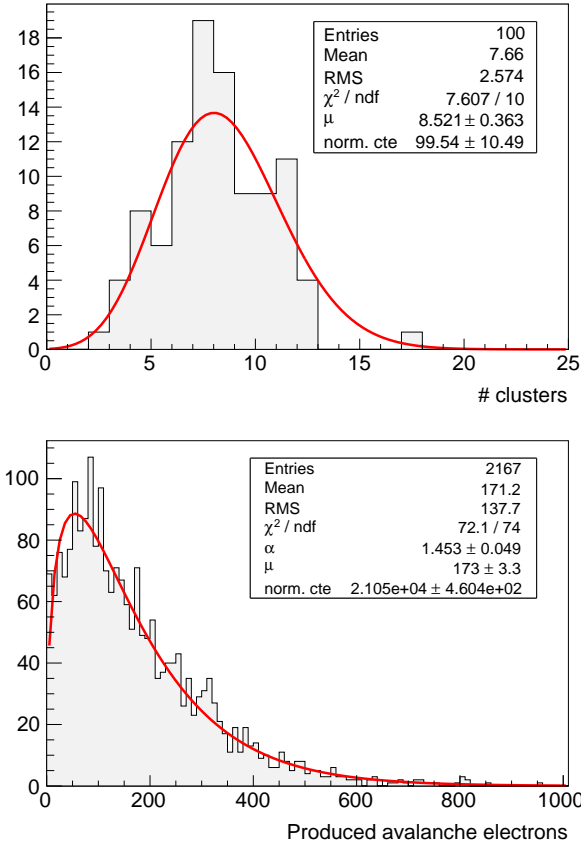


Fig. 3. Garfield++ simulations results: total cluster size fitted to a Poisson distribution (top) and avalanche size per primary electron fitted to a Polya distribution describing the gain fluctuations (bottom).

C. Induced signal

According to the Shockley-Ramo theorem, a (constant) signal will be induced on the anode during the time the swarm of electrons created in the avalanche drift from the GEM hole to the anode. The signal is proportional to the total charge Q , the electric field and the drift velocity in the induction region. In order to obtain fast pulses, the drift velocity $v_d(|\vec{E}|)$ must be chosen as high as possible.

In Fig. 4 (top), the induced charge on the anode from a single primary electron is shown, which was released in the half of the drift region. During the drift time towards the GEM hole, almost no signal is induced because the charge is masked by the top GEM foil electrode. Hence, the time offset can be calculated as:

$$\Delta t_1 = \frac{d_{\text{drift}}/2}{v_{d,\text{drift}}} = \frac{0.1 \text{ cm}}{45 \mu\text{m} \cdot \text{ns}^{-1}} = 22.22 \text{ ns}, \quad (1)$$

with $45 \mu\text{m} \cdot \text{ns}^{-1}$ the drift velocity at the drift region electric field (i.e. 1.35 kV/cm). Within an error of 3 ns, due to the non-uniform electric field and drift velocity, this value is in agreement the time offset of 18–19 ns, as shown in Fig. 4 (top). The duration of the pulse is

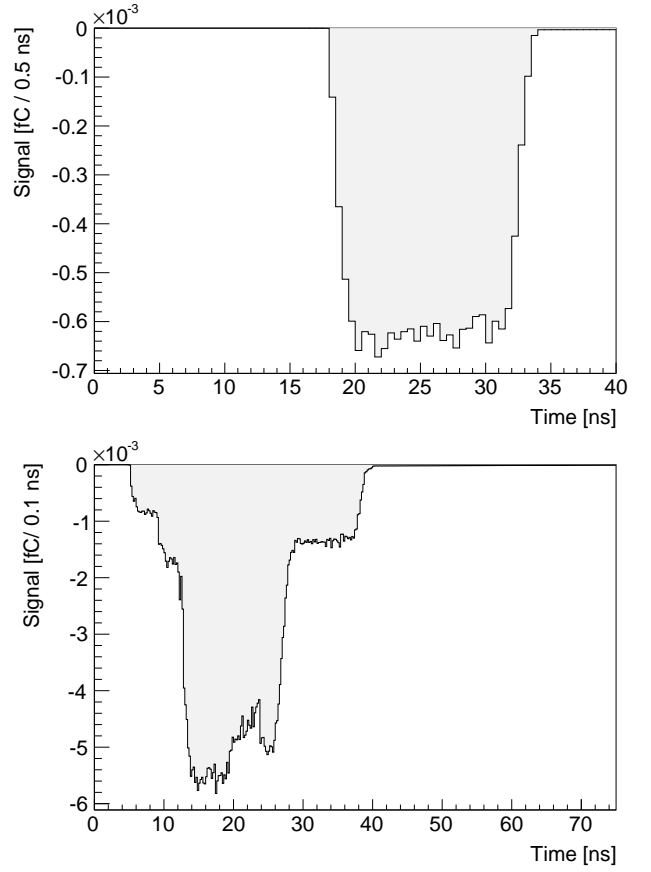


Fig. 4. Garfield++ simulations results : induced signal from a single primary electron (top) and random induced signal from a perpendicularly incident muon (bottom).

equal to the drift time of the swarm of electrons in the induction region:

$$\Delta t_2 = \frac{d_{\text{induct}}}{v_{d,\text{induct}}} = \frac{0.1 \text{ cm}}{70 \mu\text{m} \cdot \text{ns}^{-1}} = 14.29 \text{ ns}, \quad (2)$$

with $70 \mu\text{m} \cdot \text{ns}^{-1}$ the drift velocity at an electric field of 4 kV/cm, i.e. the electric field in the induction region. This is in close agreement with a duration of 15 ns, as can be seen from Fig. 4 (top). We conclude that the raw induced signal on the anode from a single primary electron is block shaped and can be described in first order by the kinematics of the charges in the drift and induction region.

When a charged particle passes through the drift region, multiple primary and secondary electrons are almost instantaneously created in the drift region, each triggering an avalanche and inducing a signal on the anode. The total induced charge is a superposition in time of the individual induced charges. An example of such superposition is shown in Fig. 4 (bottom), where the induced signal of a 100 GeV muon is shown.

IV. TIME RESOLUTION

The raw signal pulse is processed by the electronics to amplify and deform the signal to a desired shape (e.g. Gaussian). Afterwards, a discriminator is used which imposes a threshold on the signal. The time when the signal exceeds the threshold value is registered and can be used as a reference to determine the time when the charged particle passed through the detector. The value of the discriminator depends on the electronics and must be as low as possible in order to obtain accurate time measurements. Due to the stochastic nature of the processes involved in a gaseous detector, the signals and the time measurement are subjected to uncertainties. Indeed, primary ionization fluctuations, gain variations, diffusion processes and electronic noise will lead to an uncertainty of the time coordinate measurement. The combined effects result in a spread of the time measurement which is defined as the time resolution.

The dominant effect on the time resolution is the time jitter derived from primary ionization. It is clear that the last cluster in the drift region, close to the GEM foil, will induce the first signal on the readout electrode. As discussed before, the time when the induced signal starts to develop is almost equal to the time needed to drift towards the GEM hole. Because the primary ionization is a stochastic process governed by Poisson statistics, the position of the last cluster differs from event to event as well as the drift time and thus the initial time of the induced pulse. The spread of the last cluster in the z -coordinate (perpendicular to the GEM foil) is denoted as σ_z^I and arises more generally from a probability density function $P(z, \theta, L, \lambda)$. The distribution depends on the charged particle, incident angle θ and the thickness L of the drift region. Furthermore it depends on the gas mixture through λ^{-1} , because a higher cluster density yields a lower spread and thus σ_z^I decreases when λ^{-1} increases. In the first instance, we can assume the primary electrons drift towards the GEM hole with a constant drift velocity v_d . The spread of the initial time of the induced signal σ_t^I is equal to the spread in drift time of the last ionization cluster. The latter can be written as a function of σ_z^I and v_d according to:

$$\sigma_t^I = \frac{\sigma_z^I}{v_d}. \quad (3)$$

We will call σ_t^I the intrinsic time resolution of the GEM detector and it represents a value for the global time resolution, without taking diffusion and gain variations, attachment and the electronics into account. This quantity is used in the next section to compare different gas mixtures.

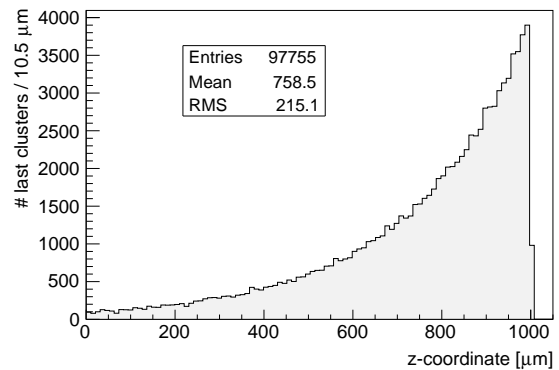


Fig. 5. Simulated $P(z, \theta, L, \lambda)$ distribution for an Ar-CO₂ mixture where 10^5 perpendicularly muons are incident on a triple GEM with 1 mm drift region thickness.

The distribution $P(z, \theta, L, \lambda)$ is shown in Fig. 5 for the Ar-CO₂ (75-25) mixture, obtained by simulating 100 GeV muons on a single GEM with 1 mm drift region thickness. If the electric field in the drift region is equal to 1.35 kV/cm, the corresponding drift velocity is equal to $v_D = 45 \mu\text{m/ns}$ and the intrinsic time resolution can be calculated as $\sigma_t^I = 214.8 \mu\text{m}/45 \mu\text{m} \cdot \text{s}^{-1} = 4.77 \text{ ns}$.

V. TIME RESOLUTION OPTIMIZATION

From the previous section and general considerations, the following algorithm is proposed to improve the time resolution. It comprises the selection of a suitable gas mixture and the adjustment of the GEM voltages and/or dimensions.

- 1) Select a gas mixture, preferable mixtures with a high cluster density λ^{-1} , high drift velocity v_d , high Townsend coefficient α and low attachment coefficient η .
- 2) Calculate the gas parameters v_d , α and η as a function of the electric field with Magboltz.
- 3) In the electric field region of 1–10 kV/cm, find the electric field value which maximizes drift velocity.
- 4) Calculate σ_z^I with HEED and calculate the intrinsic time resolution σ_t^I .
- 5) Select a GEM geometry and determine the drift and induction voltages needed to achieve the electric fields in the previous step.
- 6) Select a GEM voltage based on the value of α to achieve an appropriate gas and effective gain.
- 7) Compute the electrostatic field with ANSYS and simulate the GEM with Garfield++.
- 8) Extract the effective gain. Adjust the GEM voltage V_{GEM} if necessary when the gain is too low and repeat the previous step.
- 9) Extract timing information from the induced and convoluted pulses and compare to σ_t^I .

TABLE II
RESULTS OF GAS TABLES AND σ_z^I FOR VARIOUS GAS MIXTURES. (*) PENNING TRANSFER IS INCLUDED IN THIS SIMULATION.

Gas mixture	$v_{d,\max}$ [$\mu\text{m}/\text{ns}$]	$E(v_{d,\max})$ [kV/cm]	σ_z^I [μm]	σ_t^I μm [ns]	G_{eff}	V_{GEM} [V]
Ar-CO ₂ 75-25	75	7.0	214.8	2.90	72.73*	450
C ₅ H ₁₂	55	4.0	74.29	1.35	19.82	800
C ₄ H ₁₀	54	6.0	89.17	1.65	9.82	600
CO ₂ *	90	8.0	193.6	2.15	n.a.	n.a.
C ₄ H ₁₀ -C ₅ H ₁₂ 60-40	55	4.2	82.0	1.49	20.92	700
CO ₂ -C ₅ H ₁₂ 40-60	58	8.0	100.5	1.73	34.06	650
Ar-C ₅ H ₁₂ 40-60	55	2.1	105.9	1.93	10.77	600
Xe-C ₅ H ₁₂ 40-60	51	4.1	94.88	1.86	25.39	650
Ar-C ₄ H ₁₀ 20-80	54	4.5	101.7	1.88	n.a.	n.a.
Xe-C ₄ H ₁₀ 20-80	52	4.5	99.43	1.91	n.a.	n.a.
CF ₄	145	5.0	145.3	1.00	52.91	600
C ₅ H ₁₂ -CF ₄ 40-60	100	5.5	103.5	1.04	8.32	550
Xe-C ₅ H ₁₂ -CF ₄ 40-20-40	90	4.1	127.8	1.42	18.92	500

This algorithm was applied to different gas mixtures. Only the optimal gas mixtures are discussed here, and the results are listed in Table II. For the simulations, a single GEM was used with standard GEM foil dimensions (see Fig. 2) and $h_D = h_I = 1$ mm. The drift and induction voltages were adjusted as described in the algorithm. A suitable GEM voltage was chosen based on Townsend coefficient. The simulation was performed with perpendicularly incident 100 GeV muons (i.e. ideal circumstances).

In the discussion below, a distinction has been made between greenhouse and non-greenhouse gas mixtures because greenhouse gas mixtures are not recommended for future usage. Non-ideal circumstances such as the incident angle, the initial muon energy and the drift region thickness are briefly discussed in the last section.

A. Non-greenhouse gas mixtures

Based on the cluster density, C₅H₁₂ (pentane) and C₄H₁₀ (butane) are the best gases with cluster densities of 137 cm⁻¹ and 111 cm⁻¹ respectively. Intrinsic time resolutions of 1.35 ns and 1.65 ns were obtained respectively (see table). However, because the Townsend coefficient of both gases is relative low, high GEM voltages in the order of 700–900 V are needed. To reduce the GEM voltage, other gas constituents such as Ar, Xe or CO₂ must be added to increase the value of α . With the CO₂-C₅H₁₂ (40–60) and Xe-C₅H₁₂ (40–60) mixtures, time resolutions in the order of 1.8 ns were obtained, with adjusted GEM voltages equal to 650–750 V. However, Xe-C₅H₁₂ is more suitable because the drift and induction fields must be equal to 4.1 kV/cm in contrast to 8 kV/cm for CO₂-C₅H₁₂. Another promising gas mixture is C₄H₁₀-C₅H₁₂ 60–40 with an

intrinsic time resolution equal to 1.5 ns. Again, high GEM voltages are needed to obtain a sufficient gain. Based on the Townsend coefficient, it is expected that the Ar/Xe-C₄H₁₀ 20–80 mixtures, which have a good time resolution in the order of 1.9 ns, could operate with lower GEM voltages. However, these simulations still needs to be performed.

B. Greenhouse gas mixtures

With a cluster density of 143 cm⁻¹, C₃F₈ is a promising gas with an intrinsic time resolution of 620 ps. However, the eight fluoride atoms result in a very high attachment coefficient over the entire electric field region, with a maximum of $\eta = 840$ cm⁻¹. It is expected that many electrons will be attached leading to low gain values. Indeed, after simulating a GEM with pure C₃F₈, all the electrons were attached (even after varying the drift region voltage) and a gain of zero was obtained. The same behavior was observed with C₂F₆ ($\lambda^{-1} = 143$ cm⁻¹ and $\eta_{\max} = 110$ cm⁻¹). Additional constituents with Ar, Xe or CO₂ were proposed and simulated, but the attachment remained high and low gain values were obtained.

On the other hand, CF₄ is proven to be an excellent a gas with a large drift velocity of 145 $\mu\text{m}/\text{ns}$ at 5 kV/cm. Furthermore, it has a high Townsend coefficient and a relative low attachment in contrast to C₃F₈ and C₂F₆. It can be used as a standalone gas yielding an intrinsic time resolution of 1 ns. Moreover, different compositions of CF₄ with, for example, C₅H₁₂ or Xe were proposed, yielding a time resolution in the order of 1–1.4 ns (see table). Further research needs to be performed in order to reduce the amount of CF₄ because it is a strong greenhouse gas.

C. Non-ideal circumstances

The dependence of σ_z^I on different nonidealities were investigated through simulations. A small dependence of σ_z^I on the drift region thickness was observed with gases having low cluster densities, but almost immediately converged to a constant value when higher drift region thicknesses were used. The dependence on the muon energy was found to be negligible as the cluster density λ^{-1} is almost constant for muons with energies above 1 GeV. The incident angle clearly influences the spread σ_z^I because non-perpendicularly incident muons will leave a larger ionization track length in the drift region, which result in a decrease of σ_z^I . However, large incident angles tend to spread out the primary ionization in the transverse direction, yielding a degradation of the spatial resolution and the charge collected on the readout strips.

VI. CONCLUSIONS AND OUTLOOK

In this paper we developed an algorithm to compare different gas mixtures in order to optimize the time resolution of the Gas Electron Multiplier (GEM) with the use of simulations. After a short introduction on the GEM detector and elementary simulations, the method on how to extract timing information from the signal pulses was explained and a brief review on the stochastic processes in a gaseous detector led to the definition of

the time resolution. The stochastic nature of the primary ionization was explained in more detail and the intrinsic time resolution was defined. From this discussion, an algorithm was developed to optimize the intrinsic time resolution and was applied to different greenhouse and non-greenhouse gas mixtures. C_5H_{12} , C_4H_{10} and CF_4 were promising gas constituents yielding intrinsic time resolutions below 2 ns. Different compositions were calculated in ideal circumstances and the GEM voltage was adjusted. Afterwards, nonidealities were briefly explained.

The intrinsic time resolution does not take any electronic equipment into account, as well as gain and diffusion variations were neglected. It is clear that the intrinsic time resolution must be compared to experimental results and the algorithm deduced in this chapter must be verified.

REFERENCES

- [1] D. Abbaneo, S. Bally, H. Postema, A. Conde Garcia, J. Chatelain *et al.*, "Characterization of GEM Detectors for Application in the CMS Muon Detection System," *IEEE Nucl.Sci.Symp.Conf.Rec.*, vol. 2010, pp. 1416–1422, 2010.
- [2] F.Sauli, "Gem: A new concept for electron amplification in gas detectors," *Nucl. Instrum. Methods Phys. Res., A*, vol. 386, no. CERN-EP-2000-031. CERN-SL-2000-008-EA. 1-2, pp. 531–534, 1997.

Optimalisatie van de tijdscharacteristieken van Gas Electron Multiplier detectoren

Jan Eysermans

Mentor: Michael Tytgat

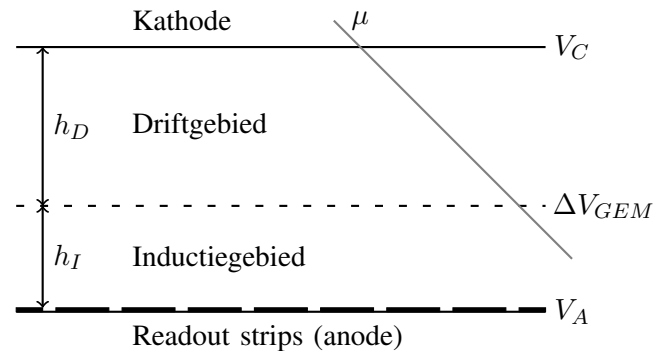
Samenvatting—De recent ontwikkelde Gas Electron Multiplier (GEM) is een kandidaat-gasdetector voor de upgrade van de Compact Muon Solenoid (CMS) aan de CERN Large Hadron Collider. Uitstekende eigenschappen zoals een hoge deeltjesflux en een hoge stralingsweerstand maakt de GEM-detector geschikt voor de hoge stralingsomgeving die verwacht wordt in het voorwaartse gebied in CMS tijdens de hoge luminositeitsfase van de versneller. In deze paper worden de tijdscharacteristieken van GEM-detectoren bestudeerd a.d.h.v. simulaties. Om de tijdscharacteristieken van verschillende gassen te vergelijken werd een methode ontwikkeld die zal worden toegepast op verschillende gassen en GEM-configuraties.

Index Terms—GEM, tijdsresolutie, Garfield++, CMS

I. INTRODUCTIE

De Gas Electron Multiplier (GEM) is een recente ontwikkeling binnen de categorie van de Micro-Pattern Gas Detectors (MPGD). De GEM-detector kan functioneren in een hoge deeltjesflux tot enkele tientallen kHz/cm^2 , een uitstekende plaatsresolutie in de orde van 100μ kan behaald worden alsook een tijdsresolutie van 5 ns . Wegens zijn grote stralingsweerstand en de mogelijkheid tot operatie in hoog magnetische velden werd de GEM-detector voorgedragen als kandidaat voor de upgrade van de muondetectoren in de Compact Muon Solenoid (CMS), één van de grote experimenten aan de CERN Large Hadron Collider (LHC) [1]. Deze upgrade zal plaatsvinden tijdens de Long Shutdown 2 (LS2) in 2018–2019 en bevat de installatie van nieuwe detectoren in het voorwaartse gebied. Wegens de LHC-luminositeitsupgrade tijdens LS2 zal een hoge deeltjesflux verwacht worden in dit gebied en GEM-detectoren werden voorgesteld voor de installatie tijdens de upgrade.

In deze paper worden de tijdscharacteristieken van de GEM-detectoren bestudeerd met simulaties. Het doel is om de oorzaak van de tijdscharacteristieken te onderzoeken en deze te optimaliseren, bij voorkeur zonder het gebruik van broeikasgassen. Eerst wordt de GEM-detector kort beschreven en elementaire resultaten van de simulaties worden besproken. Vervolgens worden de



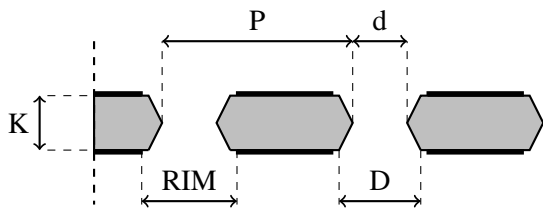
Figuur 1. Schematische doorsnede van een single GEM met readout strips. Een invallend muon ioniseert het gas in het driftgebied met de vorming van primaire elektronen die driften naar de GEM-gaten.

onzekerheden op deze tijdscharacteristieken onderzocht, wat automatisch zal leiden tot de definitie van de tijdsresolutie. Uit deze discussie zal een algoritme worden afgeleid om te zoeken naar geschikte gasmengsels en het optimaliseren van de aangelegde GEM-spanningen en dimensies. Dit wordt verder toegepast op enkele gassen en GEM-configuraties.

Verschillende simulatieprogramma's werden gebruikt waaronder ANSYS Inc. voor het definiëren van de GEM-geometrie en het berekenen van het elektrisch veld. Vervolgens werd Garfield++ gebruikt voor de simulatie van de primaire ionisatie, transport van ladingen en de simulatie van het geïnduceerde signaal. Garfield++ bestaat uit verschillende programma's zoals HEED en Magboltz voor het berekenen van de individuele processen. Verder werd ROOT gebruikt voor de analyse van de data. Een lokale simulatieomgeving werd opgezet voor het efficiënt simuleren van verschillende GEM-configuraties.

II. DE GAS ELECTRON MULTIPLIER

De GEM-detector is uitgevonden door F. Sauli in 1997 in CERN [2]. Een schematische doorsnede van een single GEM is weergegeven in Fig. 1. Tussen twee parallelle platen is een GEM-folie gespannen en het geheel wordt opgevuld met een gasmengsel. Het bovenste gedeelte is



Figuur 2. Schematische doorsnede van een GEM-folie met gaten en $5 \mu\text{m}$ gecoate elektroden. Typische afmetingen zijn $P = 140 \mu\text{m}$, $K = 50 \mu\text{m}$, $\text{RIM} = 70 \mu\text{m}$, $D = 70 \mu\text{m}$ en $d = 50 \mu\text{m}$.

het driftgebied en heeft een typische dikte h_D van enkele millimeter terwijl het inductiegebied onderaan een typische dikte h_I heeft van één of twee millimeter. De GEM-folie bestaat uit een dunne isolerende laag van polymeer (kapton) die gecoat is met koper langs beide kanten. In de folie zijn dubbelconische gaten geperforeerd met een dichtheid van 50 tot 100 gaten mm^{-2} . Een schematische doorsnede van de folie is weergegeven in Fig. 2 en de typische afmetingen zijn gegeven in het bijschrift. Een hoge spanning (V_C en V_D) wordt aangelegd over beide platen alsook over de elektroden van de GEM-folie (V_{GEM}). Omdat de folie zeer dun is ontstaan er sterke elektrische velden in de gaten tot 100 kV/cm. Het elektrische veld in het drift- en inductiegebied is typisch rond 3–8 kV/cm.

Wanneer een geladen deeltje door de detector passeert zal het gas worden geïoniseerd in de omgeving van zijn traject. De gegenereerde primaire en secundaire elektronen driften naar de GEM-gaten en een lawine zal zich ontwikkelen wegens de sterke elektrische velden in de gaten. De vrijgemaakte elektronen driften naar de anode en zullen een signaal induceren gedurende hun drifttijd. De gaten worden beschouwd als versterkingskanalen met een versterkingsfactor afhankelijk van de aangelegde spanning en het gebruikte gas. Omdat sommige veldlijnen in de gaten eindigen op de GEM-folie is het mogelijk dat elektronen vanuit de lawine gevangen geraken in de kapton laag of op de GEM-folie elektroden. De totale versterking zal dan lager zijn en de effectieve versterking wordt dan gedefinieerd als een fractie van de totale versterking G , i.e. $G_{\text{eff}} = \xi G$.

De versterking kan verhoogd worden door het toevoegen van meerdere GEM-folies in het gas volume. Voor n folies aanwezig moeten n spanningen alsook $n - 1$ tussenliggende spanningen opgelegd worden. De gebieden tussen de folies noemt men de transfergebieden. Bij gelijke spanningen over elke laag en over de GEM-elektroden kan de versterking bij benadering berekend worden met een machtswet: $G_{\text{tot}} = G^n$, met G de (effectieve) versterking van één GEM-laag.

III. SINGLE GEM SIMULATIES

Elementaire simulatie resultaten worden besproken met de simulatie van een single GEM met dimensies gegeven in Tabel I. Een standaard gasmengsel van Ar- CO_2 (75–25) werd gebruikt bij standaard temperatuur en druk (STP, i.e. $p = 1 \text{ atm}$ and $T = 293.15 \text{ K}$). Muonen met een energie van 100 GeV werden gesimuleerd loodrecht invallend op de GEM detector. Om voldoende nauwkeurige resultaten te bekomen werd de simulatie 100 keer herhaald.

Tabel I
SINGLE GEM DIMENSIES EN SPANNINGEN.

h_T	2 mm	d	$55 \mu\text{m}$
h_I	1 mm	D	$85 \mu\text{m}$
P	$140 \mu\text{m}$	RIM	$85 \mu\text{m}$
K	$50 \mu\text{m}$	Metal	$5 \mu\text{m}$
V_{drift}	270 V	E_{drift}	1.35 kV/cm
V_{induct}	400 V	E_{induct}	4 kV/cm
V_{GEM}	460 V	E_{GEM}	92 kV/cm

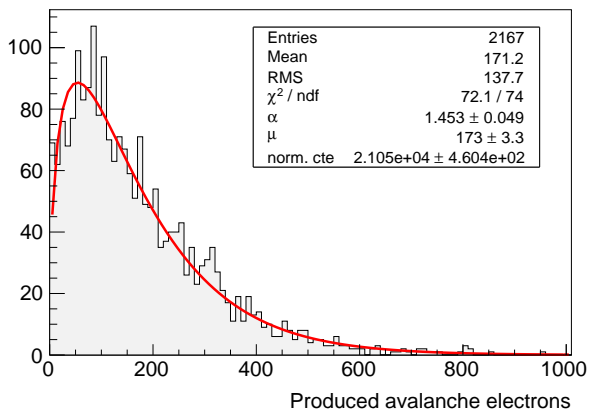
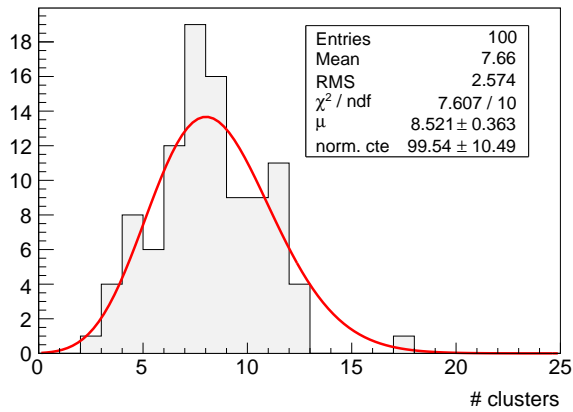
A. Primaire ionisatie

Het aantal primaire ionizaties (clusters) over een lengte L is beschreven met de Poisson-statistiek met een gemiddelde waarde L/λ . De parameter λ^{-1} is de clusterdichtheid, i.e. het aantal clusters per eenheidslengte, afhankelijk van het gas, het geladen deeltje en zijn energie. Voor Ar- CO_2 (75–25) is de clusterdichtheid gelijk aan 37.78 cm^{-1} zodat een gemiddeld aantal clusters van 7.556 behaald wordt. In Fig. 3 (boven) is het aantal clusters getoond in een histogram. Een gemiddelde waarde van 7.66 werd bekomen wat in goede overeenstemming is met de berekende waarde. Om de efficiëntie en de tijdsresolutie te optimaliseren moet de clusterdichtheid zo hoog mogelijk zijn (zie IV).

B. Townsend lawine en versterkingsfactor

De lawinegrootte voor per primair elektron is weergegeven in Fig. 3 (onder), waar de curve gefit is aan een Polya-distributie dat deze lawinefluctuaties beschrijft. Een gemiddelde versterking van $G = 171.2$ werd behaald die afhangt van de GEM-spanning V_{GEM} en het gasmengsel via de Townsend-coëfficiënt α . De effectieve versterking kan berekend worden uit de fractie ξ van elektronen die driften naar de anode en is gelijk aan 0.40484. Zo wordt een effectieve versterking van $G_{\text{eff}} = \xi G = 69.31$ behaald.

De spreiding van de elektronen op de anode is een maat voor de spatiale resolutie en een RMS van $120 \mu\text{m}$ werd behaald in beide transversale richtingen.



Figuur 3. Garfield++ simulatie resultaten: totale clustergrootte gefit aan een Poisson-distributie (boven) en de lawinegrootte per primair elektron, gefit aan een Polya-distributie die de versterkingsfluctuaties beschrijft (onder).

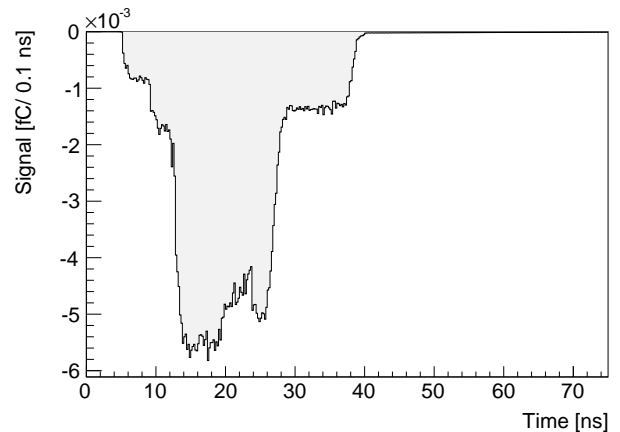
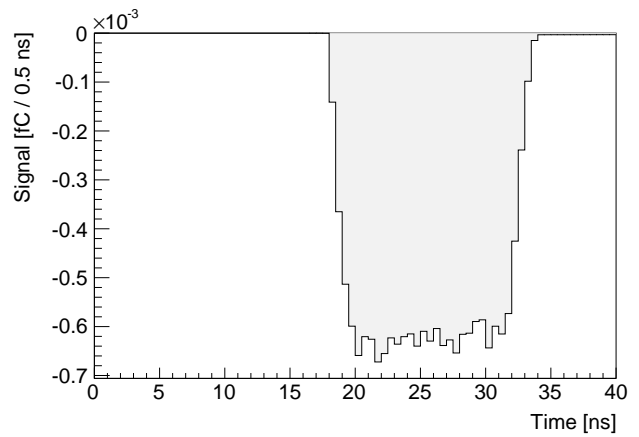
C. Geïnduceerd signaal

Als gevolg van het Shockley-Ramo-theorema wordt een signaal geïnduceerd op de anode vanaf dat de lawine-elektronen gecreëerd zijn en drijven naar de anode. Het signaal is evenredig met de totale lading Q , de elektrische veldsterkte en de driftsnelheid in het inductiegebied. Om snelle pulsen te bekomen moet de driftsnelheid $v_d(|\vec{E}|)$ zo hoog mogelijk gekozen worden.

Fig. 4 (boven) toont de geïnduceerde lading op de anode afkomstig van één primair elektron, die gesimuleerd werd in de helft van het driftgebied. Tijdens de drift naar het GEM-gat werd geen signaal geïnduceerd omdat de lading afgeschermd werd door de top GEM-folie elektrode. De tijdsoffset kan dan berekend worden als:

$$\Delta t_1 = \frac{d_{\text{drift}}/2}{v_{d,\text{drift}}} = \frac{0.1 \text{ cm}}{45 \mu\text{m} \cdot \text{ns}^{-1}} = 22.22 \text{ ns}, \quad (1)$$

waar $45 \mu\text{m} \cdot \text{ns}^{-1}$ de driftsnelheid is in het driftgebied ($E = 1.35 \text{ kV/cm}$). Binnen een foutenmarge van 3 ns door het niet-uniforme elektrische veld en driftsnelheid,



Figuur 4. Garfield++ simulatie resultaten: geïnduceerd signaal van een primair elektron (boven) en geïnduceerd signaal van een loodrecht invallend muon (onder).

is deze berekende waarde in overeenstemming met de tijdsoffset van 18–19 ns zoals te zien op Fig. 4 (boven). De tijdsduur van de puls is gelijk aan de drifttijd van de lawine-elektronen in het inductiegebied:

$$\Delta t_2 = \frac{d_{\text{induct}}}{v_{d,\text{induct}}} = \frac{0.1 \text{ cm}}{70 \mu\text{m} \cdot \text{ns}^{-1}} = 14.29 \text{ ns}, \quad (2)$$

met $70 \mu\text{m} \cdot \text{ns}^{-1}$ de driftsnelheid in het inductiegebied ($E = 4 \text{ kV/cm}$). Deze waarde komt overeen met de tijdsduur van 15 ns zoals kan afgeleid worden uit Fig. 4 (boven). Uit deze analyse concludeert men dat het ruwe geïnduceerde signaal op de anode, afkomstig van een primair elektron, blokvormig is. Het kan beschreven worden door de kinematica van de ladingen in de drift- en inductiegebieden bij constante velden.

Wanneer een geladen deeltje doorheen het driftgebied passeert zullen er verschillende primaire en secundaire elektronen vrijgemaakt worden in het driftgebied, elk leidend tot een lawine en een geïnduceerd signaal op de anode. De totale geïnduceerde lading is dan een superpositie van de individuele geïnduceerde ladingen. Als voorbeeld wordt in Fig. 4 (onder) een geïnduceerd signaal getoond afkomstig van een 100 GeV muon.

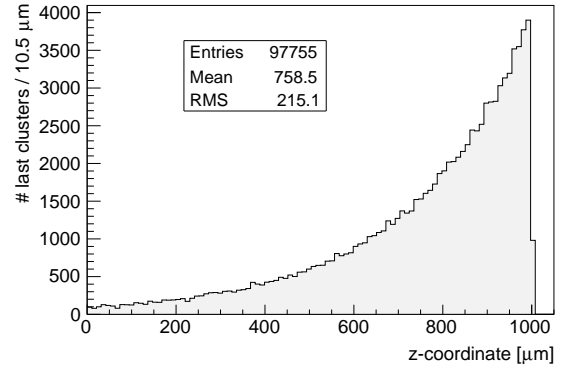
IV. TIJDSRESOLUTIE

De elektronica zal het ruwe signaal versterken en vormen tot een gewenste vorm (e.g. Gauss). Vervolgens wordt een discriminator gebruikt die een drempel op het signaal legt. De tijd wanneer het signaal de drempelwaarde overschrijdt wordt geregistreerd. Deze wordt gebruikt als referentie om de tijd te bepalen wanneer een geladen deeltje doorheen de detector gepasseerd is. De drempelwaarde hangt af van de elektronica en moet zo laag mogelijk zijn om nauwkeurige tijdsmetingen te behalen. Door de stochastische processen in de gasdetector zullen de signalen en dus de tijdsmetingen onderworpen worden aan onzekerheden. Fluctuaties bij de primaire ionisatie, versterkingsvariïaties, diffusie en elektronische ruis leiden allemaal tot een onzekerheid op de tijdsmeting. Het gecombineerde effect leidt dan tot een spreiding in de tijdsmetingen van verschillende events wat gedefiniëerd wordt als de tijdsresolutie.

Het dominante effect op de tijdsresolutie is de tijdsjitter veroorzaakt door primaire ionisatie. Het is duidelijk dat de laatste cluster gecreëerd, voor de GEM-folie, het eerste signaal zal induceren op de anode. Zoals beschreven in de vorige paragraaf zal dit signaal starten wanneer de primaire elektronen naar het GEM-gat gedrift zijn. Omdat de primaire ionisatie een stochastisch proces is, beschreven door de Poisson-statistiek, zal de positie van de laatste cluster verschillend zijn van event tot event, alsook de drittijd en dus de tijd wanneer het signaal geïnduceerd wordt. De spreiding van de laatste cluster volgens de z -richting (loodrecht op de GEM-folie) is genoteerd als σ_z^I en heeft een onderliggende distributie genoteerd als $P(z, \theta, L, \lambda)$. Deze distributie hangt af van het geladen deeltje, de invalshoek θ en de dikte L van het driftgebied. Verder is ook het gasmengsel afhankelijk via λ^{-1} omdat een hogere clusterdensiteit zal leiden tot een kleinere spreiding en dus zal σ_z^I afnemen als λ^{-1} toeneemt. In eerste instantie kan men veronderstellen dat de primaire elektronen naar de GEM-gaten driften met constante driftsnelheid v_d . De spreiding σ_t^I in de tijd van het geïnduceerde signaal zal dan gelijk zijn aan de spreiding in de tijd van de laatste cluster. Deze laatste kan beschreven worden in functie van σ_z^I en v_d :

$$\sigma_t^I = \frac{\sigma_z^I}{v_d}. \quad (3)$$

σ_t^I wordt gedefiniëerd als de intrinsieke tijdsresolutie van een GEM-detector en geeft een goede eerste orde benadering van de tijdsresolutie, zonder diffusie, versterkingsvariïaties, attachment en elektronica. In de volgende paragraaf zal deze gebruikt worden om verschillende gassen met elkaar te vergelijken.



Figuur 5. Gesimuleerde $P(z, \theta, L, \lambda)$ distributie voor het Ar-CO₂ (75–25) gasmengsel, bekomen door 10^5 loodrecht invallende muonen te simuleren op een single GEM met 1 mm driftgebied.

De $P(z, \theta, L, \lambda)$ distributie is weergegeven in Fig. 5 voor Ar-CO₂ (75–25), bekomen door simulatie van 100 GeV muonen met $L = h_I = 1$ mm. Als het elektrische veld in het driftgebied gelijk is aan 1.35 kV/cm, dan is de corresponderende driftsnelheid gelijk aan $v_d = 45$ $\mu\text{m}/\text{ns}$ en de intrinsieke tijdsresolutie wordt dan gegeven door $\sigma_t^I = 214.8 \mu\text{m} / 45 \mu\text{m} \cdot \text{s}^{-1} = 4.77$ ns.

V. OPTIMALISATIE TIJDSRESOLUTIE

Uit de voorgaande discussie en algemene beschouwingen werd het volgende algoritme voorgesteld om te tijdsresolutie te optimaliseren. Het bevat de selectie van een geschikt gasmengsel en het aanpassen van de GEM-spanningen en/of afmetingen.

- 1) Selecteer een gasmengsel, bij voorkeur met hoge clusterdensiteit λ^{-1} , hoge driftsnelheid v_d , hoge Townsend-coëfficiënt α en lage attachment coëfficiënt η .
- 2) Bereken de gaseigenschappen zoals v_d , α en η in functie van het elektrische veld met Magboltz.
- 3) Zoek het elektrische veld dat de driftsnelheid maximaliseert in gebied van 1–10 kV/cm.
- 4) Bereken σ_z^I met HEED en bereken de intrinsieke tijdsresolutie σ_t^I .
- 5) Selecteer een GEM-geometrie en bepaal de drift- en inductiespanningen nodig om het elektrische veld in de vorige stap te bekomen.
- 6) Selecteer een GEM-spanning gebaseerd op α om een geschikte versterking te bekomen.
- 7) Bereken het elektrostatisch veld met ANSYS en simuleer de GEM met Garfield++.
- 8) Bepaal de effectieve versterking en verander de GEM spanning V_{GEM} indien de versterking te laag is en herhaal de vorige stap.
- 9) Bepaal de tijdscharacteristieken van de geïnduceerde puls en vergelijk met σ_t^I .

Tabel II

RESULTATEN VAN DE GASPARAMETERS EN σ_z^I VOOR VERSCHILLENDE GASMENGSELS. (*) PENNING TRANSFER IS TOEGEPAST.

Gasmengsel	$v_{d,\max}$ [$\mu\text{m}/\text{ns}$]	$E(v_{d,\max})$ [kV/cm]	σ_z^I [μm]	σ_t^I μm [ns]	G_{eff}	V_{GEM} [V]
Ar-CO ₂ 75-25	75	7.0	214.8	2.90	72.73*	450
C ₅ H ₁₂	55	4.0	74.29	1.35	19.82	800
C ₄ H ₁₀	54	6.0	89.17	1.65	9.82	600
CO ₂ *	90	8.0	193.6	2.15	n.a.	n.a.
C ₄ H ₁₀ -C ₅ H ₁₂ 60-40	55	4.2	82.0	1.49	20.92	700
CO ₂ -C ₅ H ₁₂ 40-60	58	8.0	100.5	1.73	34.06	650
Ar-C ₅ H ₁₂ 40-60	55	2.1	105.9	1.93	10.77	600
Xe-C ₅ H ₁₂ 40-60	51	4.1	94.88	1.86	25.39	650
Ar-C ₄ H ₁₀ 20-80	54	4.5	101.7	1.88	n.a.	n.a.
Xe-C ₄ H ₁₀ 20-80	52	4.5	99.43	1.91	n.a.	n.a.
CF ₄	145	5.0	145.3	1.00	52.91	600
C ₅ H ₁₂ -CF ₄ 40-60	100	5.5	103.5	1.04	8.32	550
Xe-C ₅ H ₁₂ -CF ₄ 40-20-40	90	4.1	127.8	1.42	18.92	500

Het voorgaande algoritme werd toegepast op verschillende gasmengsels waarvan enkel de optimale gasmengsels hier worden besproken (zie Tabel II). De simulaties werden uitgevoerd met een single GEM met standaard GEM-folie afmetingen (zie Fig. 2) en met $h_D = h_I = 1$ mm. De drift- en inductiespanningen werden aangepast zoals besproken in het algoritme. Verder werd de GEM-spanning V_{GEM} gebaseerd op de Townsend-coëfficiënt. De simulatie werd uitgevoerd met loodrecht invallende 100 GeV muonen (i.e. ideale omstandigheden).

In de onderstaande discussie is een onderscheid gemaakt tussen niet-broeikas- en broeikasgassen omdat deze laatste niet aanbevolen zijn voor toekomstig gebruik. Niet-ideale omstandigheden zoals de invalshoek, de initiële muonenergie en de dikte van het driftgebied worden kort besproken in de laatste paragraaf.

A. Niet-broeikasgasmengsels

Baserend op de clusterdensiteit zijn C₅H₁₂ (pentaan) en C₄H₁₀ (butaan) de beste gassen met waarden van respectievelijk 137 cm⁻¹ and 111 cm⁻¹. De intrinsieke tijdsresolutie is 1.35 ns en 1.65 ns respectievelijk (zie tabel). Omdat de Townsend-coëfficiënt van beide gassen laag is, zijn hoge waarden voor V_{GEM} nodig in de orde van 700–900 V. Om deze spanningen te reduceren worden er andere constituenten zoals Ar, Xe of CO₂ toegevoegd om de waard van α te doen toenemen. Met de CO₂-C₅H₁₂ (40–60) en Xe-C₅H₁₂ (40–60) mengsels werden tijdsresoluties in de orde van 1.8 ns behaald, met GEM spanningen in de orde van 650–750 V. Xe-C₅H₁₂ is echter meer geschikt omdat de drift- en inductievelden moeten gelijk zijn aan 4.1 kV/cm in vergelijking met 8 kV/cm voor CO₂-C₅H₁₂. Een ander veelbelovend gasmengsel is C₄H₁₀-C₅H₁₂ 60–40 met een tijdsresolutie

van 1.5 ns, hoewel ook hier hoge GEM-spanningen nodig zijn om een geschikte versterking te bekomen. Gebaseerd op α zijn de Ar/Xe-C₄H₁₀ 20–80 gunstig met een tijdsresolutie van ongeveer 1.9 ns. Verwacht is dat deze kunnen opereren onder V_{GEM} spanningen maar deze simulaties moeten nog uitgevoerd worden.

B. Broeikasgasmengsels

Met een clusterdensiteit van 143 cm⁻¹ is C₃F₈ een veelbelovend gas met een intrinsieke tijdsresolutie van 620 ps. Door zijn acht fluoride atomen is de attachment-coëfficiënt zeer hoog over een groot bereik van het elektrische veld, met een maximum van $\eta = 840$ cm⁻¹. Er wordt dus verwacht dat veel elektronen verloren gaan, resulterend in een lage versterking. Na de simulaties van een single GEM met zuiver C₃F₈ werden inderdaad alle electronen attached en een versterking van nul werd bekomen. Dezelfde resultaten werden bekomen met C₂F₆ ($\lambda^{-1} = 143$ cm⁻¹ en $\eta_{\text{max}} = 110$ cm⁻¹). Toegevoegde constituenten zoals Ar, Xe of CO₂ werden voorgesteld en gesimuleerd, maar de attachment-coëfficiënt bleef hoog en lage versterkingen werden behaald.

Anderzijds blijkt CF₄ een uitstekend gas te zijn met een hoge driftsnelheid van 145 $\mu\text{m}/\text{ns}$ bij 5 kV/cm. Verder heeft deze een hoge Townsend-coëfficiënt en een relatief lage attachment-coëfficiënt in vergelijking met C₃F₈ en C₂F₆. Het kan gebruikt worden als zuiver gas resulterend in een tijdsresolutie van 1 ns. Verder werden verschillende composities berekend met o.a. C₅H₁₂ of Xe, leidend tot een tijdsresolutie in de orde van 1–1.4 ns (zie tabel). Verder onderzoek is nodig om de hoeveelheid CF₄ te reduceren omdat het een sterk broeikasgas is.

C. Niet-idealiteiten

De afhankelijkheid van σ_z^I op verschillende niet-idealiteiten werd onderzocht via simulaties. Een kleine afhankelijkheid van σ_z^I op de dikte van het driftgebied werd geobserveerd met gassen die een lage clusterdensiteit hebben, maar convergeert vrijwel onmiddellijk naar een constante waarde bij toenemende dikte van het driftgebied. De afhankelijkheid van de energie van het muon is verwaarloosbaar omdat de clusterdensiteit λ^{-1} vrijwel constant is voor muonen met een energie groter dan 1 GeV. De invalshoek heeft duidelijk een invloed op de spreiding σ_z^I omdat niet-loodrecht invallende muonen een langere ionisatie track achterlaten in het driftgebied, resulterend in een afname van σ_z^I . Grotere invalshoeken zullen echter zorgen voor een grotere transversale spreiding van de primaire elektronen, resulterend in een degradatie van de spatiale resolutie en de lading geïncollateerd op de readout strips.

VI. CONCLUSIES EN VOORUITZICHTEN

In deze paper werd een algoritme beschreven om verschillende gasmengsels te vergelijken die de tijdsresolutie van de Gas Electron Multiplier (GEM) kan optimaliseren, gebruikmakende van simulaties. Na een korte introductie van de GEM-detector en resultaten van elementaire simulaties, werd een methode uitgelegd om de tijdsinformatie af te leiden uit de geïnduceerde

signaalpulsen. Een korte beschrijving van de stochastische processen in een gasdetector leidde automatisch tot de definitie van de tijdsresolutie. De stochastische effecten van de primaire ionisatie werd besproken en een intrinsieke tijdsresolutie werd gedefinieerd. Uit deze discussie werd een algoritme afgeleid om de intrinsieke tijdsresolutie te optimaliseren. Dat werd toegepast op verschillende gasmengsels, onderverdeeld in broeikas- en niet-broeikasgassen. C_5H_{12} , C_4H_{10} en CF_4 werden naar voor geschoven als kandidaat-gassen met een intrinsieke tijdsresolutie onder 2 ns. Verschillende composities werden berekend in ideale omstandigheden en de GEM-spanningen werden aangepast. Nadien werden enkele niet-idealiteiten kort besproken.

De intrinsieke tijdsresolutie is onafhankelijk van de gebruikte elektronica, diffusie-effecten en versterkingsvariëaties. Het is dus nodig om de intrinsieke tijdsresolutie te toetsen aan experimentele waarden en het gebruikte algoritme te verifiëren.

REFERENTIES

- [1] D. Abbaneo, S. Bally, H. Postema, A. Conde Garcia, J. Chatelain *et al.*, "Characterization of GEM Detectors for Application in the CMS Muon Detection System," *IEEE Nucl.Sci.Symp.Conf.Rec.*, vol. 2010, pp. 1416–1422, 2010.
- [2] F.Sauli, "Gem: A new concept for electron amplification in gas detectors," *Nucl. Instrum. Methods Phys. Res., A*, vol. 386, no. CERN-EP-2000-031. CERN-SL-2000-008-EA. 1-2, pp. 531–534, 1997.

Contents

1	Introduction	3
1.1	Motivation of particle physics	3
1.2	Tools used in particle physics	4
1.3	The Large Hadron Collider	5
1.4	The CMS experiment	7
1.5	Thesis overview	9
2	General principles of gaseous detectors	11
2.1	General processes in gaseous detectors	11
2.2	Interaction of a charged particle with the gas atoms	11
2.3	Charge transport	16
2.4	Charge amplification	20
2.5	Signal creation	23
2.6	Readout electronics	24
3	Gas Electron Multipliers	25
3.1	The Gas Electron Multiplier	25
3.2	GEM performance	28
3.3	Production process	30
3.4	The CMS triple GEM	31
3.5	Applications	33
4	Simulation software	35
4.1	ANSYS	35
4.2	Garfield ++	39
4.3	Local simulation environment	41
4.4	Source code	43
5	GEM simulations and measurements	45
5.1	Single GEM simulations	45
5.2	Gain measurements and energy calibration	53
5.3	Comparison gain measurements with simulation	57
6	Time resolution	59
6.1	Time resolution	59
6.2	Time resolution optimization method	63
6.3	Time resolution optimization	65
6.4	Non-ideal circumstances	72
6.5	Summary	74

7 Summary and outlook	75
7.1 Summary	75
7.2 Outlook	77
Appendix A Single GEM ANSYS input file	79
Appendix B Source code	83
Appendix C Drift velocities of used gases	85

Glossary

ALICE	A Large Ion Collider Experiment
ATLAS	A Toroidal LHC Apparatus
BSM	Beyond Standard Model
BX	Bunch crossing
CSC	Cathode Strip Chamber
CERN	Centre Européenne pour la Recherche Nucléaire
CMS	Compact Muon Solenoid
DAQ	Data Acquisition
DESY	Deutsches Elektronen-SYNchrotron
DT	Drift Tube
ECAL	Electromagnetic Calorimeter
FEM	Finite Element Method
FWHM	Full Width Half Maximum
GEM	Gas Electron Multiplier
HCAL	Hadronic calorimeter
HEP	High energy physics
HL-LHC	High Luminosity LHC
HV	High Voltage
IP	Interaction point
LEP	Large Electron Positron
LHC	Large Hadron Collider
LS1/2	Long Shutdown 1/2
MPGD	Multi-Pattern gaseous detector
MWPC	Multi-Wire Proportional Chamber
PAI	Photo-Absorption Ionization
PMT	Photomultiplier
pp	proton-proton
PS	Proton Synchrotron
QFT	Quantum Field Theory
QCD	Quantum Chromodynamics
RPC	Resistive Plate Chamber
SM	Standard Model
SPS	Super Proton Synchrotron
SUSY	Supersymmetry
TOE	Theory Of Everything

Chapter 1

Introduction

1.1 Motivation of particle physics

*There is nothing new to be discovered in physics now,
all that remains is more and more precise measurement.*

In the second half of the nineteenth century, young students – including M. Planck – were advised to leave the field of physics because it was generally accepted that physics was complete, comprising Newton’s law of motion and gravity as well as Maxwell’s equations for electromagnetism. The quote above by L. Kelvin in 1882 precisely summarizes the thoughts of great physicists at that time. It soon became clear that it was not possible to fit some phenomena in this classical picture such as the position of the earth relative to the vacuum, the black body spectrum and the atomistic view on matter with the recently discovered electron. Great minds such as A. Einstein, M. Planck and N. Bohr were needed to think beyond the classical thoughts to solve these problems. Special and general relativity was developed by Einstein in 1900–1915 leading to a successful theory for dynamics and gravity. Bohr successfully implemented the forced idea of energy quantization, proposed by Planck in his theory to explain the black body spectrum, by assuming that the energy levels inside an atom are discrete. This was the starting point of the development of Quantum Mechanics where the wave-particle duality, known from light phenomena, was generalized to matter by L. de Broglie in 1924. This gave independently rise to wave and matrix mechanics developed by E. Schrödinger and W. Heisenberg respectively, which were found to be equivalent by P.A.M. Dirac in 1930. The peculiar discovery that an electron has an additional angular momentum, later called the spin, was perfectly described with quantum mechanics which provided a first experimental validation. The consequences of quantum mechanics deeply shocked the world of physics as it turned out Nature behaves non-deterministic. As time moved on, Dirac tried to unify both quantum mechanics and special relativity within the framework of Quantum Field Theory (QFT), leading to the existence of the positron. In 1931, E. Fermi developed a successful theory on β -decay wherein the neutrino was involved, which was postulated by W. Pauli one year before. After the war, physicists explored the world of atomic nuclei and the constituents of the proton and the neutron. This search was triggered because of a tremendous increase of discovered particles in the fifties and early sixties. Theoreticians developed the quark model as fundamental building blocks of these particles (hadrons) to explain this ”particle zoo”, and the first experimental evidence was observed in deep inelastic scattering experiments at the Stanford Linear Accelerator in 1968. Together with the quark model, the strong force was introduced to explain quark-quark interactions leading to confinement and the explanation of the strong nuclear force between the protons and neutrons in atomic nuclei. The strong force was theoretically developed within QFT and is nowadays referred as Quantum Chromodynamics (QCD). A new particle,

the gluon, was proposed as the force carrier of the strong force and was discovered in the eighties at DESY. Later on, in the seventies, S. Weinberg, A. Salam and S. Glashow proposed a theory to unify the weak force describing β -decay and the electromagnetic force. This resulted in the electroweak force, with as force carriers the heavy W^\pm and Z^0 vector bosons. Both particles were experimentally observed by the UA1 collaboration at CERN in 1983.

The above paragraph describes a very brief history of particle physics and is nowadays summarized as the Standard Model (SM) of particle physics. In this model, (visible) matter is described with six types of quarks (u, d, c, b, t and b), six leptons ($e, \mu, \tau, \nu_e, \nu_\mu$ and ν_τ) and their antiparticles. Furthermore, the electroweak and strong force is operating between (some of) these particles with the vector bosons (γ, g, W^\pm and Z^0) as the force carriers. Recently, the Brout-Englert-Higgs boson was added to the SM, discovered in 2012 by the CMS and ATLAS collaborations at CERN. This boson is responsible for the existence of the Higgs field, giving mass to the fundamental particles (except the neutrinos). However, history is repeating itself because a beautiful theory such as the Standard Model is not able to describe phenomena such as dark matter, matter-antimatter asymmetry, the gravitational force and the neutrino masses. Different other theories such as supersymmetry (SUSY) were developed in the nineties but are not yet experimentally verified. Other theories such as string theory provides a Theory of Everything (TOE), combining general relativity with the Standard Model. It is clear that experimental evidence needs to be obtained to discover new or exclude existing physics. Hence, a lot of research experiments such as the LHC, astrophysical experiments (IceCube at the South Pole, the Planck Observatory in space) and many others are exploring this physics beyond the standard model.

1.2 Tools used in particle physics

The main modern tools used in particle physics are particle accelerators and detectors. Since the advent of radioactivity in 1896, experimental physicists invented several detectors to measure and identify radiation such as α particles and electrons. In the early days, great discoveries such as the proton were achieved by using natural radioactive sources but it soon became clear that the energy of such sources was not sufficient. Particle accelerators were developed in the 1930s wherein elementary particles are accelerated and collided head on (or impinging on a fixed target), producing other particles through materialization by $E = mc^2$ or yielding scattering information. As the accelerator technology evolved in time, higher energies became available producing a higher amount of particles in the collisions. Hence, more sophisticated particle detectors were needed. This evolution is still going on today and major efforts are done to obtain high performance detectors. In the following text, a brief history of detectors is given, mainly based on [1], [2] and [3].

In the early days, it was already possible to detect X-rays by using photographic plates. Charged particles could be detected with a cloud chamber, invented by C.T.R. Wilson in 1911 or by using ionization chambers developed by E. Rutherford and H. Geiger in 1908 and improved in collaboration with W. Mueller in 1928. The cloud chamber played a very important role in experimental physics and was used with the discovery of the Compton effect, cosmic muons and the positron. The scintillating principle was already known in the 1930s but only became popular with the invention of the photomultipliers (PMTs) in the beginning of the 1940s. It was mainly used as a counting detector and is nowadays still frequently used in particle physics. After the war, the bubble chamber was invented based on the cloud chamber where liquid H_2 at its boiling temperature generates bubbles in the vicinity of an ionization track. It was used for the detection of neutral currents in 1973 at CERN. The spark chamber was developed already before the war, but was improved in the 1950s and intensively used until the 1980s. This was the first detector which could be used and produced

on a larger scale. The next important invention was the Multi Wire Proportional Chamber (MWPC) in 1968, which consists of many parallel wires placed between two parallel plates. Such detectors yield excellent spatial resolutions in the order of $300 \mu\text{m}$ and were mainly used as tracking detectors. The position resolution was even further improved in 1971 with the invention of drift chambers which uses a fast scintillator to determine the time of incident from where the drift time of the primary electrons to the wire can be calculated. The initial distance could then be extracted when the drift velocity was known.

Semiconductor detectors were developed in the 1980s but only widely used in the 1990s due to optimized photolithography techniques which reduced the manufacturing costs. Silicon detectors have good spatial and time resolutions but are still rather expensive when used on large-scale detectors and therefore gas detectors are still used on large-scale detectors. From the early 1990s, the Micro Pattern Gas Detectors (MPGD) have been developed to replace the wires in the MWPC detectors by electrical micro-structures on the anode. However, it turned out such detectors are barely radiation resistant and have a high dead time. A new type of MPGD, the Gas Electron Multiplier (GEM), was proposed in 1997 by F. Sauli. He proposed to add an intermediate grid between the two parallel plates acting as amplification holes. Another common detector used is the Resistive Plate Chamber (RPC), developed in the beginning of the 1980s. This detector originated from the spark chamber developed early in the fifties, but a resistive layer of $\approx 10^{10} \Omega\text{cm}$ is located before the anode and cathode to reduce the spark probability. A comparison of both time and spatial resolution of the different types of gas chambers is given in Table 1.1.

Table 1.1: Comparison of the spatial and time resolution of different types of gaseous detectors. The position resolution depends on the granularity of the wires/strips and nominal values of respectively 1 mm and 3 cm were used.

Detector type	Invention	Spatial resolution	Time resolution
Spark chamber	1950s	$\sim 1 \text{ mm}$	$0.5\text{--}1 \mu\text{s}$
RPC	1982	$2\text{--}5 \text{ mm}$	$< 3 \text{ ns}$
MWPC	1990	$300 \mu\text{m}$	$0.1 \mu\text{s}$
GEM	1997	$100 \mu\text{m}$	5 ns

1.3 The Large Hadron Collider

The Large Hadron Collider (LHC) is a circular accelerator with 27 km in circumference, situated 100 m below ground level near Geneva. It is the largest accelerator ever built which accelerates two proton beams in opposite directions with a designed center-of-mass energy of $\sqrt{s} = 14 \text{ TeV}$. A scheme of the total accelerator complex and its experiments is shown in Fig. 1.1. The aim of the LHC is to discover new physics at the TeV energy range, with a main search for the Higgs boson. The latter was indeed discovered in 2012 during the 2010–2013 run. Besides the search for the Higgs boson which is part of the SM, the LHC also investigates BSM theories such as dark-matter models (SUSY), string theory and the search for extra dimensions.

The first LHC studies dated from 1982, but large progress was made after the discovery of the W and Z bosons in 1983. At the end of the eighties, the Large Electron Positron (LEP) collider became operational at CERN to perform detailed studies on the W^\pm and Z^0 bosons. At the beginning of the nineties, it was agreed to use this 27 km LEP tunnel to house the LHC accelerator. The LEP equipment was removed in 2002 and one year later the LHC installation was started. The accelerator is not perfectly circular but rather consists of straight and bending sections containing respectively 1232 dipole magnets and 392

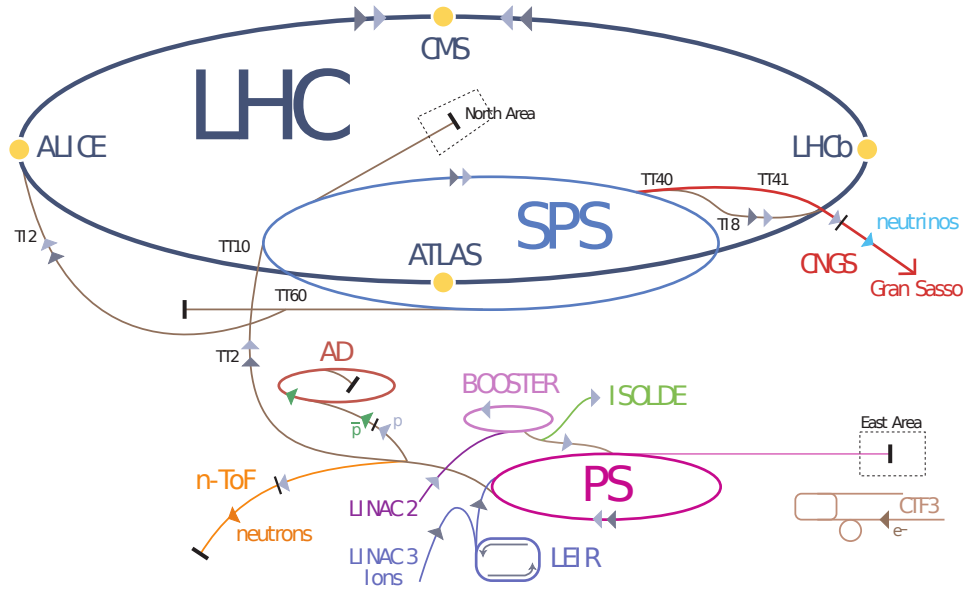


Figure 1.1: LHC accelerator complex with its four main experiments (CMS, ATLAS, ALICE and LHCb) and its predecessor accelerators (SPS, PS, BOOSTER, LINAC2) [4].

quadrupole magnets for bending and focusing the beams. Before injecting the proton beams in the LHC, several pre-accelerators are used to gradually increase the proton energy (see Fig. 1.1), respectively the LINAC2 (50 MeV), Booster (1.4 GeV), Proton Synchrotron (26 GeV), Super Proton Synchrotron (450 GeV) and finally the injection in the LHC accelerator. The beams are not continuous but divided into bunches in order to accelerate the beam using radiofrequency cavities, installed near the quadrupole magnets. In total there are 3564 bunch spaces in which 2808 are filled with protons due to the limitations in the beam injection process through kicker magnets. Each filled bunch contains about 10^{11} protons and are squeezed together by the focusing magnets to a beam diameter of about $20 \mu\text{m}$, yielding a luminosity¹ in the order $\mathcal{L} = 10^{34} \text{ cm}^{-2}\text{s}^{-1}$. At the interaction point (IP), every 25 ns the proton beams collide head on which is equivalent to a bunch crossing (BX) frequency of 40 MHz (values valid for the 2011–2013 run).

The first beams at 14 TeV were expected in 2008 but due to an accident with the interconnection between the magnets, around 100 magnets were broken and needed to be repaired. In November 2009, the LHC was restarted and the protons were accelerated up to 7 TeV at the beginning of 2010. One year later the beam energy was upgraded to 8 TeV. Due to precautions after the magnet accident, it was decided not to go to the designed value of 14 TeV right away. After the 2010–2013 run, the first long shutdown (LS1) began in order to repair and install new detector and accelerator equipment. The next run is foreseen to start in 2015 with an energy of 13 TeV and eventually reaching the designed value of 14 TeV. The second long shutdown (LS2) is planned in 2018–2019 in order to further upgrade the equipment and prepare the system for the High Luminosity LHC (HL-LHC) in 2020. The luminosity will then be increased by a factor 10, reaching a value of $10^{35} \text{ cm}^{-2}\text{s}^{-1}$.

Four large experiments are installed in the accelerator tunnel: ATLAS, CMS, ALICE and LHCb. ATLAS and CMS are twins because both searches for the same physics, though different detector technologies are used. ALICE is used for investigations in heavy-ion physics

¹The luminosity \mathcal{L} is an accelerator parameter as a function bunch crossing (BX) frequency and the amount and density of the particles in each bunch. It is related to the pp -cross section σ_{tot} and the interaction rate R through $R = \mathcal{L} \cdot \sigma_{\text{tot}}$

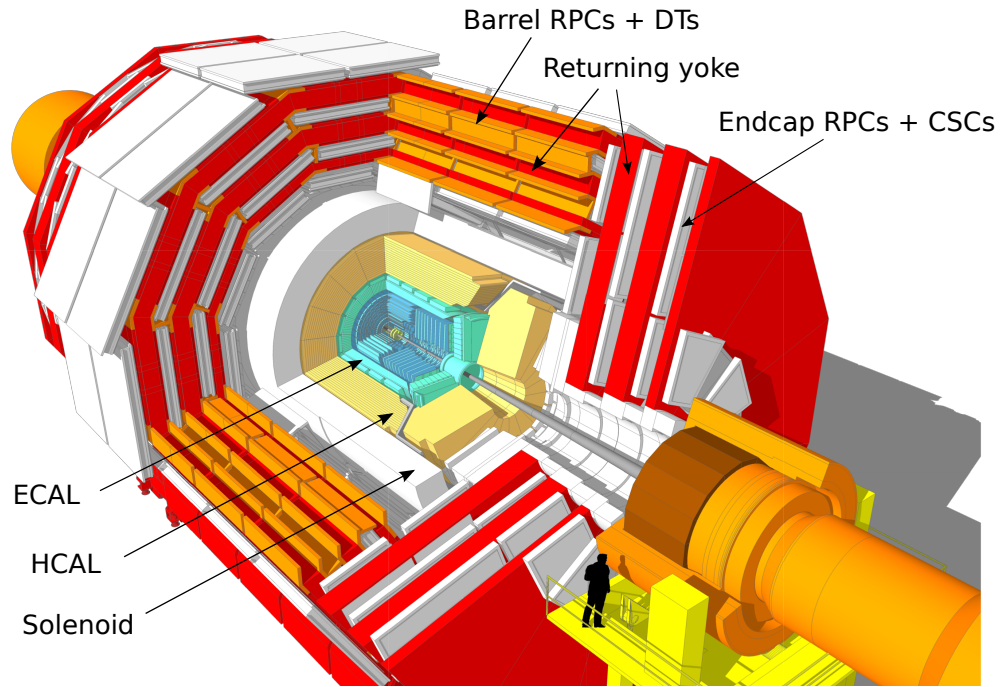


Figure 1.2: Sketch of the CMS detector with its main components [5].

using heavy ion collisions (lead nuclei) which were injected after global run in 2010 and 2012. The LHCb detector is especially designed for research in b-quark physics. Furthermore, several other experiments are housed in the LHC accelerator complex providing detailed studies of specific processes.

1.4 The CMS experiment

The Compact Muon Solenoid (CMS) detector is one of the four large detectors installed in the LHC tunnel. It measures 25 m long, 15 m in diameter and weighs about 12500 tons. The weight is mainly due to the superconducting solenoid that generates a magnetic field of 3.8 Tesla along the beam axis. It has a traditionally cylindrical structure divided in rings or shells (see Figure 1.2). The innermost shell is the silicon tracker, followed by the electromagnetic (ECAL) and hadronic (HCAL) calorimeters and ending with the muon chambers at the outer shells. The silicon tracker is used as a tracking detector for all charged particles. Electrons and photons are completely absorbed in the ECAL crystals and the hadrons are absorbed in the HCAL. The magnet is placed between the calorimeters and the muon chambers. It is a so called 4π -detector which almost completely covers the total solid angle. To achieve this, the CMS detector is composed of a cylindrical part called the barrel, and closed by two endcaps at each side of the barrel. A cross section in the (R, z) -plane is shown in Fig. 1.3.

As already mentioned before, at the interaction point every 25 ns two proton bunches collide head on with the production of many particles such as photons, leptons, fermions, etc. The Level-1 trigger system, operating at the BX frequency of 40 Mhz, selects online according to complex algorithms the interesting events up to a rate of 100 kHz. Trigger decisions are made only with raw data from both calorimeters and the muon detectors. With a luminosity $\mathcal{L} = 10^{34} \text{ cm}^{-2}\text{s}^{-1}$ and a proton-proton cross section $\sigma_{pp} = 115 \text{ mb}$ at the designed center-of-mass energy, the interaction rate is equal to $r = \mathcal{L} \cdot \sigma_{pp} \approx 1.15 \cdot 10^9 \text{ Hz}$, or about 36 interactions per bunch crossing. This phenomenon, called in-time pile-up, makes it very hard to select interesting events. Algorithms were written and implemented in the Level-1 trigger hardware which are based on particle identification and imposing thresholds on energy or

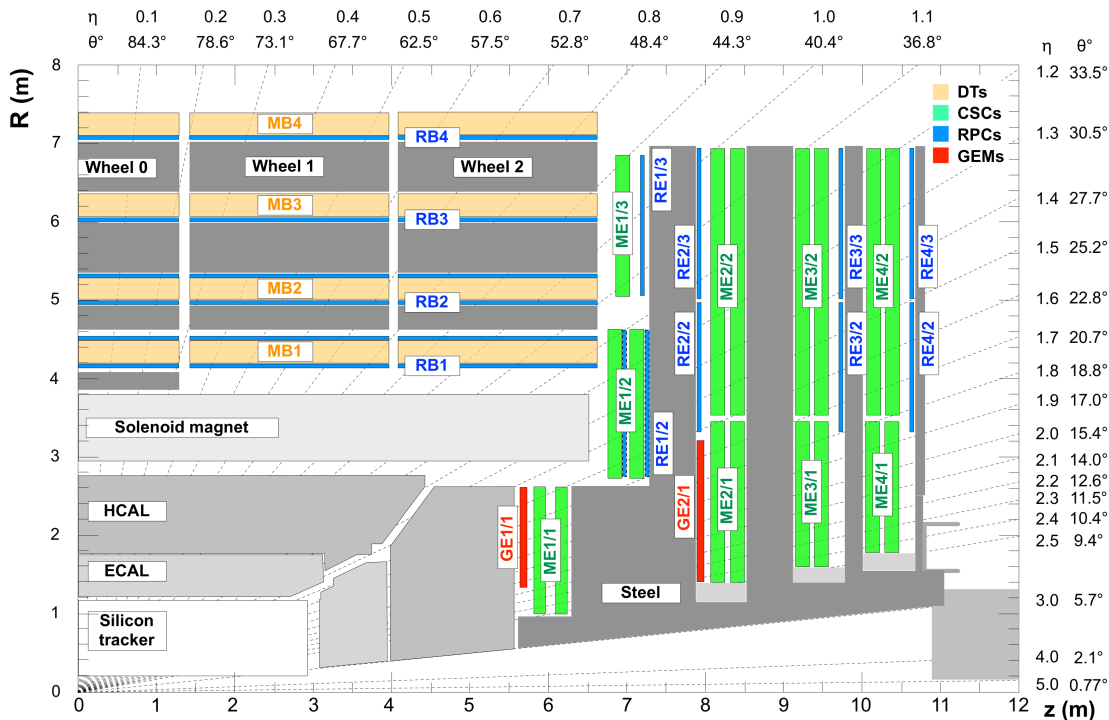


Figure 1.3: CMS cross section in the (R, z) -plane, indicating the different subdetectors of the muon system. The proposed GE1/1 and GE2/1 layers are indicated in red [6].

momentum. For example, the CMS Level-1 trigger imposes typically the following thresholds for electrons and muons:

$$\begin{aligned} \text{single electron: } & p > 4 \text{ GeV}/c, \\ \text{single muon: } & p_T > 20 \text{ GeV}/c. \end{aligned}$$

Below these thresholds, different phenomena such as multiple scattering becomes dominant which drastically decreases the precision of the measurement and reconstruction. After the Level-1 trigger, the (offline) High-Level trigger further reduces the event rate down to 100 Hz. Precise particle reconstruction algorithms are applied which uses the different detector signals to obtain the particle flow and energy or momentum. Because the beam energy is such high, the transverse momentum of the partons or quarks inside the protons can be neglected. Hence, the total transverse momentum measured from one collision must add to zero. Within this framework it is possible to calculate the missing energy carried by undetectable neutrinos or BSM exotic particles.

A right handed coordinate system is defined having its origin at the IP, the x-axis pointed towards the center of the LHC ring and the y-axis perpendicular to the LHC plane. Hence, the z-axis is tangent to the beam line at the IP. It is convenient to use spherical coordinates (θ, ϕ) to describe the geometry of the detector, with θ the angle measured from the z-axis. However, the pseudorapidity defined as,

$$\eta = -\ln \tan \left(\frac{\theta}{2} \right) \quad (0 \leq \eta \leq \infty),$$

is more often used in high energy physics to describe the polar angle. Because the CMS detector is cylindrically symmetric, local material variations are only along η and are (almost) constant in the ϕ direction.

The muon system

The muon detectors are used for muon identification, triggering and measuring the transverse momentum. They are situated in the outermost shells of the CMS detector and consist of drift tubes (DT) in the barrel region and cathode strip chambers (CSC) in the endcap region (see Figure 1.3 for a cross sectional view). An additional trigger signal is provided by the RPCs, both present in the barrel and endcap region, having a different sensitivity to background events. The CSCs and DTs are used as tracking detectors whereas the RPCs are used for time measurements, resulting in an excellent muon detector with high precision and efficiency. In order to measure the transverse momentum of the muons, a returning yoke is placed between the muon detectors which bends the muons in the magnetic field. The transverse momentum is then extracted by measuring the bending curvature of the particles trajectory through this field. The global active detector material coverage is limited by $|\eta| \leq 2.5$, distributed over $0 \leq |\eta| \leq 1.2$ for the barrel and $0.9 \leq |\eta| \leq 2.4$ for both endcaps. The endcap RPC system consists of four disks on both sides of the IP (RE-4 up to RE4), each disk containing three rings equipped with RPC detectors (REi/1, REi/2 and REi/3, where i represents the disk number). However, due to funding problems, the fourth endcap (RE4 and RE-4) disc with RPCs was not ready for installation before the first run in 2010, as well as the first ring in all disks remained unoccupied with RPCs. The coverage of the RPCs was only up to $\eta \leq 1.6$ during the first run. The installation of ring 2 and 3 was successfully done during LS1. The forward region $1.6 \leq \eta \leq 2.5$ corresponding with ring 1 will remain empty during the second run. High particle fluxes in the order of 10 kHz/cm^2 are expected in this forward region when the luminosity will be increased during the third run from 2020. The current RPCs are not expected to be suitable to handle such high particle rates and new detectors must be developed. After initial studies, the GEM detector was proposed as a candidate for installation during the LS2. Indeed, excellent properties such as handling the high particle rates, a good spatial and time resolution, radiation resistant, operational in a high magnetic field, etc. proved the GEM as a suitable detector in the forward region. In Fig. 1.3, both proposed GEM stations GE1/1 and GE2/2 are indicated in red. The detectors are still in development for further optimization and for improving the construction techniques on a large scale. More details about the properties, performances and construction techniques are given in chapter 3.

1.5 Thesis overview

The present text is the description of the simulations performed on GEM detectors. Although already proved to be excellent detectors, there is still some freedom to improve its properties and performances. The purpose of this master thesis is the investigation of the time resolution with the use of simulations. Indeed, simulations are appropriate for such studies as there is a large degree of freedom in the parameter space (e.g. dimensions, environmental parameters, etc.) which are not always directly accessible in the laboratory. Furthermore, the development of algorithms and simulation software started already in the eighties and has now become a full branch in experimental physics for the development of small and large scale detectors. A lot of work have been done through the years to implement and optimize physical processes aiming more accurate simulations. On the contrary, detailed simulations require heavy computation time and it is the task of the experimental physicist to neglect unwanted physics to reduce the computation time.

The investigation on the GEM time resolution is done gradually and requires in the first place a thorough discussion of the processes in gaseous detectors. The necessary concepts are introduced and supported by elementary results obtained with the simulations. The GEM detector is introduced and the working principle is explained with the previous intro-

duced concepts. The properties, performances, production processes and applications will be discussed, mainly with a view on the CMS GEM prototypes. Afterwards, the simulation software is discussed because it is necessary to understand at some level the algorithms and physical processes implemented in the simulations. After having introduced the necessary concepts and the simulation tools, a single GEM detector is simulated and the results are discussed in detail. Furthermore, some experimental measurements are explained and the results of the simulations are compared to experimental results. In the next and final step, the concepts of time resolution are defined and a method is deduced to improve the time resolution of GEM detectors. This method is applied to different configurations and also on realistic scenarios such as the CMS GEM detectors.

Chapter 2

General principles of gaseous detectors

Prior to the discussion on the GEM simulations in the following chapters, the concepts and principles of gaseous detectors are described in detail. Indeed, the origin of the time resolution of gaseous detectors traces back to the physics on atomic and molecular level. Furthermore, it is essential to understand the algorithms and models used in the simulation tools in order to validate the results of the simulation. In this chapter, we systematically discuss in detail the different processes occurring in gaseous detectors from the interaction of the to be detected particle with the detector up to the creation of the signal on the readout electrodes. As a good starting point, a quick and general overview of the different processes in such detectors is given, followed by a detailed discussion in the next paragraphs. This text is mainly based on [7] and [8], individual references are given in the text.

2.1 General processes in gaseous detectors

In general, a gaseous detector in its simplest form consists of a gas volume which is typically a few mm wide, enclosed between two metal electrodes. An electric field is applied between both electrodes which automatically defines the anode and cathode electrodes. When a charged particle traverses the gas, it locally ionizes the gas atoms liberating electrons and ions along its path. Both electrons and ions drift towards the anode and cathode respectively under influence of the electric field. However, when the electric field is sufficiently high, the electrons can gain enough energy to further ionize the gas atoms. This triggers an avalanche process and the amount of free electrons and ions grows exponentially. The liberated electrons and ions further drift towards the anode and cathode respectively, inducing a current on both electrodes. This current is picked up by the readout electronics to create the final signal. The pulse shape of this signal can be analyzed and the time resolution can be defined.

2.2 Interaction of a charged particle with the gas atoms

When a charged particle passes through a gas medium, it locally ionizes the gas in the vicinity of its trajectory due to inelastic collisions with the gas atoms. One refers to an ionizing collision when the inelastic collision liberates at least one electron. Depending on the particle, the deposited energy can be only a fraction of its energy (e.g. muons) or the particle can be completely absorbed in the gas (e.g. photons). It is possible, however, that a single ionizing collision with a gas atom liberates more than one electron. Therefore one refers to an ionization cluster rather than a single ionization electron. The ionization is a result from inelastic collisions with the gas atoms or molecules as a whole, or individual elastic collisions with the atomic electrons. In general many other processes occur depending on energy of the charged particle, but only the inelastic collisions are important because these processes only generate directly ionization. The liberated electrons in a cluster can be regarded as free

within a certain time range and drift under influence of the electric field towards the anode where an avalanche might be triggered along its path.

If the particle is relativistic, which is usually the case in high energy physics (HEP), the energy loss from a single ionization collision is negligible. As a result, each collision or ionization process is independent and one can define a mean-free-path λ between two gas ionization encounters:

$$\lambda = \frac{1}{N\sigma_i}, \quad (2.1)$$

with N the number density of the gas mixture. σ_i is the total ionization cross section which depends on the energy of the charged particle and the gas mixture. The total ionization cross section for a gas mixture can be calculated by weighting the individual ionization cross sections σ_j of the gas constituents with their corresponding number densities N_j :

$$\sigma_{i,\text{tot}} = \sum_j \sigma_j N_j. \quad (2.2)$$

In fact, λ depends on the pressure p and temperature T because $N = N(p, T)$, which can be expressed in first order by the ideal gas law $p = NkT$, with k the Boltzmann constant. As a result, λ is proportional to the temperature and inverse proportional to the pressure.

The amount of ionization encounters k over a track length L can be described with a Poisson distribution with mean L/λ :

$$P(L/\lambda, k) = \frac{(L/\lambda)^k}{k!} \exp(-L/\lambda). \quad (2.3)$$

The inverse of λ is called the cluster density or the specific primary ionization, i.e. the number of clusters per unit length. In Fig. 2.1 (top), the cluster density is plotted for incident muons as a function of the kinetic energy. This plot is obtained with the simulation software HEED which will be discussed in the next chapters. The cluster density is one of the important parameters which dominates the time resolution and therefore the primary ionization process deserves a more detailed discussion. However, a theoretical description of the primary ionization process is rather difficult because many processes occur on the atomic level and must be described with quantum mechanics. A complete theory to describe globally the primary ionization does not (yet) exist. In a first attempt, we can estimate the amount of ionization electrons with the use of energy conservation. The W -value for a gas mixture is defined as the mean energy needed to create one electron-ion pair and must be measured for every gas mixture and type of charged particle. The W -value is at least equal to the lowest ionization potential I_{min} of the gas mixture. In general, however, the W -value is higher than I_{min} because also non-ionizing processes (e.g. excitations) occur whose energy transfer is not available for ionization. For example, the lowest ionization potential for Ar is 15.76 eV whereas the W -value is equal to 26.3 eV. It should be noted that the W -value for a given gas mixture is almost independent of the type and energy of the charged particle. Typical values are in the range of 25–35 eV. Now, when a charged particle traverses the gas medium depositing an energy Q in the gas medium, the average liberated electrons $\langle n \rangle$ is equal to:

$$\langle n \rangle = \frac{Q}{W}. \quad (2.4)$$

This equation is only useful if the value of Q is known. For photons, which are completely absorbed in the gas medium provided this medium is a few mm thick, the full photon energy E_γ is used to create electron-ion pairs and thus $Q = E_\gamma$. For charged particles which deposits only a small fraction of its initial energy, the deposited energy can be calculated if the stopping power S is known, defined as:

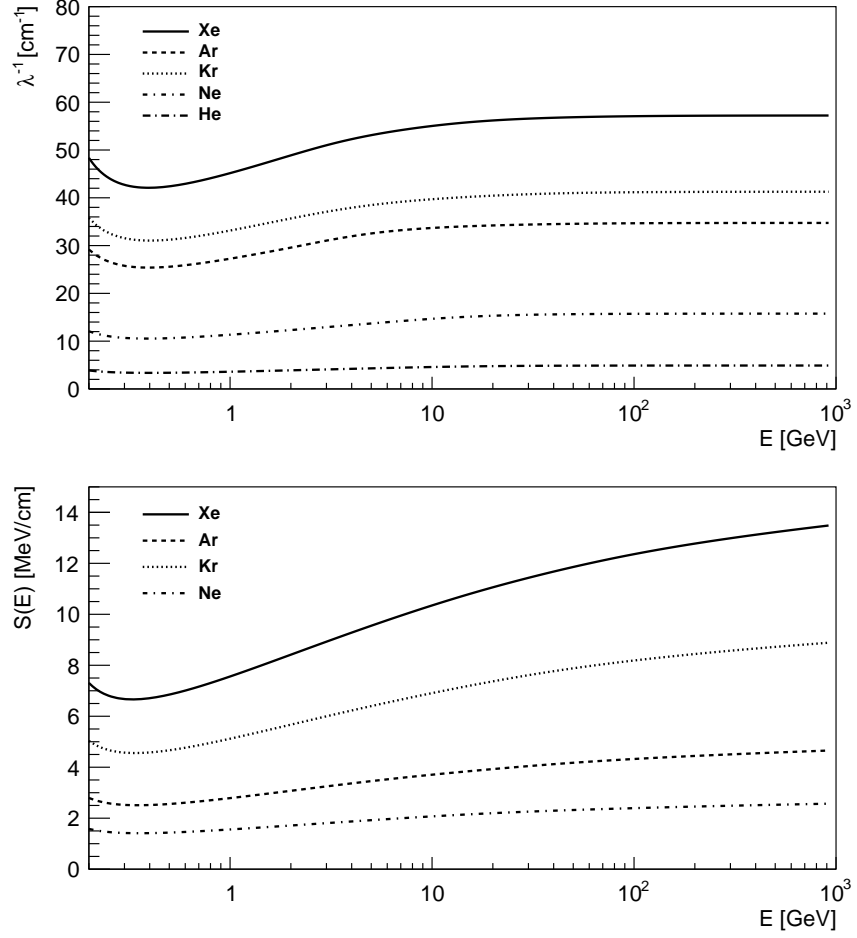


Figure 2.1: Simulated cluster density (top) and stopping power (bottom) for different noble gases at standard conditions ($p = 1$ atm, $T = 293.15$ K) as a function of the muon energy E . Plots obtained with HEED simulations and may slightly differ from experimental results (see 4.2.1).

$$S(E) = -\frac{dE}{dx}. \quad (2.5)$$

The stopping power curves are tabulated for various charged particles impinging on different targets. Once known, the total deposited energy can then be calculated as:

$$Q = \int dE = - \int_l S(E) dx. \quad (2.6)$$

Many models have been proposed in order to describe theoretically the stopping power, depending on the type of processes and the energy of the charged particle. Indeed, the stopping power can be divided in various contributions from different processes such as electronic processes, radiative processes and nuclear processes [9]. For heavy relativistic particles such as muons, one can write $S(E) = S_e(E) + b(E)E$, where $S_e(E)$ is the electronic part due to inelastic collisions and $b(E)E$ captures the radiative and nuclear contributions. For particle detectors, only the electronic processes are important because they lead directly to ionization.

Historically, H. Bethe was the first to calculate the electronic stopping power for non-relativistic particles in 1930 and extended his calculation for relativistic particles in 1932. His formula reads:

$$S_e(E) = -\frac{dE}{dx} = \frac{4\pi}{m_e c^2} \frac{n Z'^2}{\beta^2} \frac{e^4}{(4\pi\epsilon_0)^2} \cdot \left(\ln \left[\frac{2m_e c^2 \beta^2}{I(1-\beta^2)} \right] - \beta^2 \right), \quad (2.7)$$

with:

m_e the electron rest mass,

c the speed of light,

e the electronic charge,

n the electron density in the gas medium ($n \propto Z$, with Z the atomic number of the gas),

ϵ_0 the vacuum permittivity,

Z' the charge of the incident particle,

I the mean excitation potential of the gas medium and

β the velocity of the incoming particle over the speed of light.

This equation was obtained by making use of first-order quantum perturbation theory and is only valid for heavy charged particles. Higher order corrections are calculated which yields terms up to Z^3 (Barkas-Andersen) and Z^4 (Bloch). In the model proposed by Bethe, the gas medium is described by a single parameter, being the mean excitation potential I . Bloch showed in 1933 that for atoms the mean excitation potential can be written as $I = (10 \text{ eV})Z$. In Fig. 2.1 (bottom), the (simulated) electronic stopping power is plotted for incident muons for different noble gases. These curves tend to have a similar shape as the cluster density curves. Indeed, both quantities are related to each other which can be understood from a simple energy balance. When a charged particle generates λ^{-1} clusters per unit length, each cluster having on average n electrons, the energy balance reads:

$$W \cdot n \cdot \frac{1}{\lambda} = \left\langle \frac{dE}{dx} \right\rangle. \quad (2.8)$$

Assuming n and W as constant over the total energy range, λ^{-1} is indeed proportional to the Bethe energy-loss formula. Small deviations can be ascribed due to a slight dependence of W on the energy. The dependence of λ^{-1} on Z , with Z the (mean) atomic number of the gas, is clearly shown in Fig. 2.1. Indeed, the heaviest noble element Xe shows the highest cluster density and vice versa.

Up to now we only concentrated on the energy aspects of energy loss, but not on specific interactions and processes occurring in the primary ionization process. For simulation purposes, more detailed information is needed such as the position of the clusters and the exact energy transfer. The previous quantities only describe these phenomena on an average level. As a result, a more fundamental theory is needed to describe the primary ionization process. One such theory is the Photo Absorption Ionization model which is discussed in the next section.

2.2.1 The Photo-Absorption Ionization model

In the Photo-Absorption Ionization (PAI) model, introduced by Allison and Cobb in 1980 [10], the differential cross section $d\sigma/dE$ is calculated, from which other quantities can be derived such as the energy spectrum $F(E) dE$ of the primary electrons or the cluster density. In the model, it is assumed that the total ionization cross section σ_i depends in a certain way on the photo-absorption cross section σ_γ , i.e. the absorption cross section of real photons. Indeed, the interaction of a charged particle with a gas atom is pure electromagnetic with the exchange of virtual photons (γ^*) between the charged particle and atom.

The gaseous medium can be described with a complex dielectric constant $\epsilon = \epsilon_1 + i\epsilon_2$. Recalling that the imaginary part of the dielectric constant of a plane wave traveling in a medium describes the damping coefficient (and thus the energy loss), the photo-ionization

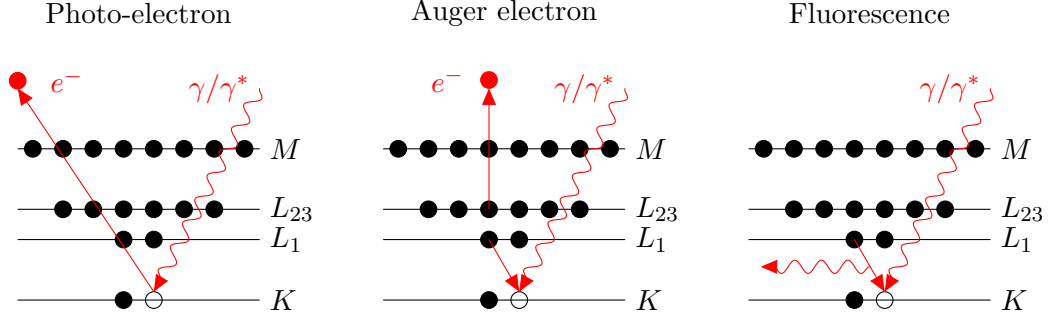


Figure 2.2: Example of direct core shell ionization leaving a photoelectron and a vacancy (left) and relaxation of the atom through emission of an Auger electron (center) or a fluorescent photon (right).

cross section σ_γ is directly related to the imaginary part ϵ_2 . The absorption of a (virtual) photon results in the emission of an electron and a vacancy in the ionized atom (see Fig. 2.2 (left) as an example). The emitted electron is called the photo-electron and originates most of the time from the K-shell as the energy transfer between the atom and the charged particle is usually very high (relative to the atom binding energies). After a short time, the atom relaxes by filling this vacancy with an electron from a higher shell. The energy released with this process can be transferred to a second atomic electron (an Auger electron), or more likely, the emission of a fluorescent photon (see Fig. 2.2 center and right respectively). This photon can escape the gas medium or can again be absorbed inducing further ionizations. Indeed, the energy of the fluorescent photon is equal to the binding energy of the relaxed electron which is in the order of keV. The result of the total ionization process are photo- and Auger electrons and are called primary electrons. The energy of such electrons is typically in the order of 1–10 eV, lower than the lowest ionization potential of the gas. This ionization mechanism is only valid for one cluster is repeated several times along the path of the particle, depending on σ_i (see Eq. 2.10). However, the fluorescent photons can travel a certain distance through the medium inducing new clusters on different locations. Furthermore, when a primary electron is very energetic (due to a large and efficient energy transfer), this electron can also travel through the medium inducing other ionizations along its path. These energetic electrons are called δ -electrons.

When applying this theory on virtual photons, the dispersion relation $E = pc/\sqrt{\epsilon}$ does not hold anymore and such relationship has to be premised. Allison and Cobb assumed the absorption as point like in the energy-domain, i.e. described with a Dirac function. Combining these principles, they were able to calculate the differential cross section in a semi-classical approach. For one primary electron, the differential cross-section reads:

$$\frac{d\sigma}{dE} = \frac{\alpha}{\beta^2\pi} \left[\frac{\sigma_\gamma(E)}{EZ} \ln \frac{2m_e c^2 \beta^2}{E[(1 - \beta^2 \epsilon_1)^2 + \beta^4 \epsilon_2^2]^{1/2}} + \frac{Z}{N\hbar c} \left(\beta^2 - \frac{\epsilon_1}{|\epsilon|^2} \right) \theta + \frac{1}{ZE^2} \int_0^E \sigma_\gamma(E') dE' \right], \quad (2.9)$$

with the following constants:

α the fine-structure constant,

β the velocity of the incoming particle over the speed of light,

$\theta = \arg(1 - \epsilon_1 \beta^2 + i\epsilon_2 \beta^2)$,

E the energy transfer to the primary electron,

Z the (weighed) atomic number of the medium and

m_e the electron mass.

The photo-ionization cross section σ_γ remains as a free parameter in this equation, and must be known either from a theoretical model or from experimental results. For high energies above the K-shell ionization potential, it can be shown that the differential cross section reduces to the Rutherford cross-section. Indeed, at very high energies, the electrons can be regarded as free and the charged particle interacts elastically with the atomic electrons.

Once the differential cross-section is calculated, the cluster-size distribution can be obtained according to:

$$\frac{1}{\lambda} = \int N \frac{d\sigma}{dE} dE, \quad (2.10)$$

and the energy spectrum of the primary electrons can be calculated as:

$$F(E) = \frac{N}{1/\lambda} \frac{d\sigma}{dE}. \quad (2.11)$$

2.2.2 The Penning effect

The previous discussion only deals with direct ionization, e.g. $\mu A \rightarrow \mu A^+ e^-$. Depending on the gas mixture, other ionization processes could also occur via excited states of gas atoms. One such process is where the charged particle excites an atom A which transfers its excitation energy to a atom B . The latter atom can be ionized if the excitation energy of A^* is higher than the lowest ionization potential of B . This process, summarized by $A^* B \rightarrow AB^+ e^-$ is called the Penning effect.

The penning effect reduces the W -value as more primary electrons are generated. It has to be implemented in the simulations algorithms because it can also affect the gain of the detector. The Penning transfer probability f_p is defined as a measure for the Penning effect, depending on the gas mixture and the relative densities of the atoms. It turns out the determination of f_p is a rather difficult task because it has to be matched with experimental results and no direct formula or theory is available. As an example we consider the Ar-CO₂ gas mixture which is typically used in gaseous detectors. The lowest ionization potential of CO₂ is equal to 13 eV and is lower than the excitation levels of Argon. The Penning transfer probability is equal to $f_p = 0.57$ when the gas composition is 75–25%.

2.3 Charge transport

Electrons and ions created in primary ionization processes can be regarded as free in a short time interval and are subjected to different processes such as diffusion, recombination, etc. Furthermore, the trajectories of electrons and ions are governed by the electromagnetic field and collisions with the gas atoms. For detailed simulations purposes, their trajectories must be calculated accurately and all these effects must be taken into account. This requires in the first place the knowledge of the electric and magnetic field (\mathbf{E} and \mathbf{B}) inside the gas medium, either being an analytic expression or obtained by Finite Element Methods (FEM).

In a macroscopic picture, the general equation of motion of a charged particle with mass m (electrons or ions) in an electromagnetic field can be written as:

$$m \frac{d\mathbf{u}}{dt} = q(\mathbf{E} + \mathbf{u} \times \mathbf{B}) - K\mathbf{u}. \quad (2.12)$$

The scalar K represents the isotropic frictional force due to collisions with the gas atoms, which can be regarded as the average friction due to microscopic collision processes. After introduction of a time constant $\tau = m/K$, the steady-state solution ($t \gg \tau$) in absence of a magnetic field ($\mathbf{B} = \mathbf{0}$) reads:

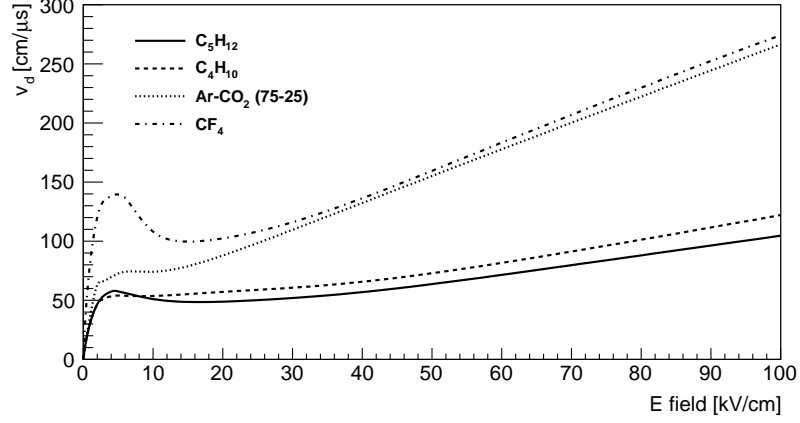


Figure 2.3: Simulated electron drift velocity for common gases used in this paper, as a function of the electric field. Plots obtained with Magboltz simulations and may slightly differ from experimental results (see 4.2.2).

$$\mathbf{u} = \frac{q}{m} \tau \mathbf{E} = \mu \mathbf{E} = \mathbf{v}_d. \quad (2.13)$$

The steady-state value of \mathbf{u} is called the drift velocity \mathbf{v}_d and is proportional to the electric field. However, the proportionality constant μ , called the scalar mobility, depends in general on the magnitude of the electric field and no linear relationship is obtained. In the next section, the electron drift velocity will be treated on a microscopic level where τ will have a physical interpretation.

2.3.1 Drift of electrons

The energy distribution of free electrons can be described by the classical Maxwell-Boltzmann distribution:

$$f(\epsilon) = \sqrt{\frac{\epsilon}{\pi kT}} \exp\left(-\frac{\epsilon}{kT}\right). \quad (2.14)$$

In this formula, ϵ is the energy of the free electrons, T is the absolute temperature and k is the Boltzmann constant. The average energy of free electrons is called the thermal energy and is equal to $\epsilon_0 = \frac{3}{2}kT$. This can be understood from the equipartition theorem where each degree of freedom has a contribution of $\frac{1}{2}kT$. Electrons liberated from ionization processes cannot completely be regarded as free (only after a very short time interval) but are governed by collisions with the gas atoms and the electric field present in the detector. The electrons are isotropically scattered from the gas atoms because of its small mass. The average time interval between two collisions is denoted as τ and the average electron energy can be written as the sum of the thermal energy ϵ_0 and a contribution ϵ_E gained from the acceleration in the electric field:

$$\epsilon = \frac{1}{2}mv^2 = \epsilon_E + \epsilon_0 = \epsilon_E + \frac{3}{2}kT. \quad (2.15)$$

The electric field in particle detectors is sufficient high such that $\epsilon_E \gg \epsilon_0$ and thermal motion can be neglected. The mean-free-path λ between two collisions can be expressed as a function of the collision cross section $\sigma(\epsilon)$:

$$\lambda = \frac{1}{N\sigma(\epsilon)}, \quad (2.16)$$

where N is the number density of the gas atoms. The total cross section consists of elastic (recoil) and inelastic collisions (excitations: shells, rotational, vibrational). Combining the average velocity v with the mean-free-path λ , the average time between two collisions can be expressed as $\tau = \lambda/v$, or:

$$\tau = \tau(\epsilon) = \frac{1}{N\sigma(\epsilon)v(\epsilon)}. \quad (2.17)$$

The inverse of τ is sometimes called the collision rate. We are now able to reinterpret the scalar mobility. An electron is accelerated in the electric field with a component

$$\mathbf{a} = -\frac{e\mathbf{E}}{m_e}. \quad (2.18)$$

The drift velocity is defined as the average additional velocity gained through the electric field, or the average of the acceleration multiplied by the time between two collisions:

$$\mathbf{v}_d = \langle \mathbf{a}t \rangle = -\frac{e\tau}{m_e}\mathbf{E} = -\frac{e}{m_e} \frac{1}{N\sigma(\epsilon)v(\epsilon)}\mathbf{E}. \quad (2.19)$$

This equation shows the dependence of \mathbf{v}_d on the average energy ϵ of the electrons (and thus on \mathbf{E}) as well as the dependence on the cross section of the processes and the environmental parameters such as the temperature and pressure. In Fig. 2.3, the electron drift velocity is plotted for common used gases in this paper. This plot is obtained with Magboltz, a simulation tool which will be discussed in chapter 4.

2.3.2 Drift of ions

The treatment of the drift velocity for ions is much more complicated than for electrons. Due to a large ion mass, the energy transfer between the ion colliding with a gas molecule is much higher than for electrons. Therefore, the collision is not isotropic and must be treated with the conservation laws of energy and momentum. The energy gained through the electric field is much smaller than for electrons because of the large ion mass and thus the average ion energy is mostly thermal energy. Hence, an analytic treatment of the ion drift velocity as a function of the electric field is very complicated. The global result after such theoretical calculations can be summarized in the definition of the ion mobility μ , which has formally the same definition as the electron mobility:

$$\mathbf{v}_d = \mu(|\mathbf{E}|)\mathbf{E}. \quad (2.20)$$

The ion mobilities are tabulated for different gases as a function of the electric field. For gas mixtures, the drift velocity can be calculated with Blanc's law:

$$\frac{1}{v_d} = \sum_k \frac{N_k}{N} \frac{1}{v_{d,k}}, \quad (2.21)$$

where the sum runs over all the gas mixture constituents with densities N_k and $N = \sum_k N_k$.

2.3.3 Diffusion

Diffusion is the natural process where, for example, a dense cloud of electrons will spread out in space. This effect is important in particle detectors as it could influence the transport of electrons. When a cloud of particles is squeezed at $t = 0$ in a single point $\mathbf{r} = 0$, it will diffuse following a Gaussian profile in space:

$$n(r, t) = \frac{1}{(4\pi Dt)^{3/2}} \exp\left(-\frac{r^2}{4Dt}\right), \quad (2.22)$$

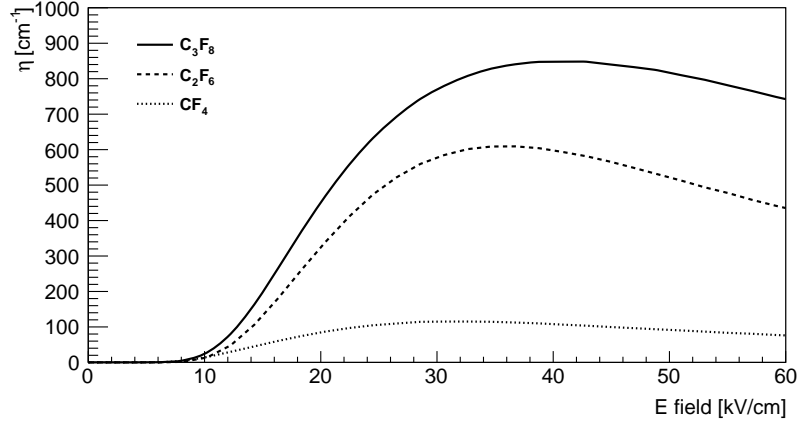


Figure 2.4: Simulated attachment for fluoride gases used in this paper, as a function of the electric field. Plots obtained with Magboltz simulations and may slightly differ from experimental results (see 4.2.2).

with a standard deviation of $\sigma = \sqrt{2Dt}$. D is called the diffusion constant and depends on the energy of the electrons or ions. For charges at thermal energies (e.g. ions or electrons in very low electric fields), there exists a relationship between D and the mobility μ :

$$D = \frac{kT}{e} \mu. \quad (2.23)$$

This relationship is called the Nernst-Townsend or Einstein formula. Because the mobility for electrons is much higher than for ions, the diffusion process is more important for electrons.

When electric or magnetic fields are present, the diffusion process seems to be not isotropic and a diffusion tensor must be introduced rather than a single diffusion constant. When only an electric field is present, the diffusion coefficient can be split up in a longitudinal (D_l) and transverse (D_t) part, relative to the direction of the field.

2.3.4 Recombination

When a positive ion and a negative electron collide, they might be recombine to form a neutral atom releasing a low energy photon. The recombination rate equation can be written as:

$$R_c = \frac{dn^+}{dt} = \frac{dn^-}{dt} = \alpha n^+ n^-, \quad (2.24)$$

with n^+ , n^- the ion and electron concentration respectively and α the recombination coefficient. Recombination can be important because it could loss the primary electrons and reducing the detector efficiency. However, it seems recombination is not an important effect when high electric fields are present because the charges are strongly separated by the field.

2.3.5 Attachment

A more important effect for electron loss is attachment. Electronegative atoms with high electron affinities could attach electrons in a collision to form a stable negative ion and a low energetic photon. Typical atoms are the halogenides (F, Cl) or oxygen, the latter which could be present as an impurity. It is important to reduce the amount of attachment by choosing a good gas mixture in order to collect all the primary electrons without losses. On the other hand, if attachment is a dominant process, the slow negative ions drifting towards the anode will cause noise on top of the signal.

The decrease of electrons dN due to attachment per unit length can be written as:

$$dN = -N\eta ds, \quad (2.25)$$

where η is the attachment coefficient expressed in cm^{-1} , and is equal to the amount of electrons attached per unit distance in the gas medium. It depends on the gas composition (attachment cross sections) and electric field, and must be measured for each gas mixture. At low electric fields, $\eta = 0$ because the mean energy ϵ of the electrons is too low to induce attachment as the cross sections are very low at low electron energies. Furthermore, qualitatively, the attachment coefficient is in first order proportional to the electronegativity of the gas atoms. Indeed, electronegative atoms tend to form stable negative ions by attracting an electron. This is the highest for the halogenides (F, Cl, O). For noble gases, the attachment coefficient is zero. For the common fluoride gases used in this paper, the attachment coefficient is plotted in Fig. 2.4.

2.3.6 The Boltzmann equation

Gases are excellently described by statistical mechanics, developed at the beginning of the twentieth century. For non-equilibrium systems (e.g. under influence of an electric field), the gas can be described by the Boltzmann transport equations [11]. In this theory, each component of the gas is described by a probability density function $f_i(\mathbf{r}, \mathbf{p}, t)$, defined such that the amount of gas molecules or atoms of type i is given by:

$$dN_i = f_i(\mathbf{r}, \mathbf{p}, t) d^3\mathbf{r} d^3\mathbf{p}. \quad (2.26)$$

The change of f in time has contributions from collisions, diffusion and eventually an external applied force. The external forces are referred in this discussion to electromagnetic fields. The collision contribution consists of elastic and inelastic terms described by their cross sections. At relative high electric fields, the inelastic terms contain processes such as ionizations and attachment whereas for lower electric fields electronic and vibrational excitations are dominant. When the external force is expressed by a field $\mathbf{F}(\mathbf{r}, t)$, the Boltzmann equation becomes:

$$\frac{\partial f_i}{\partial t} + \frac{\mathbf{p}_i}{m_i} \cdot \nabla f_i + \mathbf{F} \cdot \frac{\partial f_i}{\partial \mathbf{p}_i} = \left(\frac{\partial f_i}{\partial t} \right)_{\text{coll}}. \quad (2.27)$$

In this equation, m_i is the mass of the gas component i . The term in right-hand side of the equation represents the collision term and must be calculated for the individual processes (elastic and inelastic).

Once the probability density function is known, one can calculate the gas parameters such as drift velocity, diffusion, attachment and Townsend coefficient. However, it is in general not possible to calculate f_i analytically and one must apply numerical calculations such as Monte Carlo integrators. An example is the Magboltz simulation tool which is briefly discussed in section 4.2.2.

2.4 Charge amplification

The amount of primary electrons is too low to create a detectable signal in the readout electronics. Indeed, such amount of electrons will induce a signal which is comparable to the electronic noise level and it will be impossible to distinguish between noise and signal. It is necessary to increase the amount of signal electrons with a factor of $10^2 - 10^8$, depending on the type of the detector and the electronics.

The amplification process in gaseous detectors is achieved by applying a strong (local) electric field inside the detector. The primary electrons drifting in this strong field gain enough energy to ionize the gas atoms, liberating additional electrons which in turn ionize the gas and a cascade of ionizations will develop. This cascade, or avalanche, stops when the electrons are captured on the anode or when the electric field is too low to induce further ionization. The latter is the case in GEM detectors, which have strong non-uniform fields. One refers to the proportional mode if the signal is proportional to the total amount of electrons generated. However, when the electric field is very high, the large amount of slow drifting ions generated in the avalanche can distort the electric field and nonlinear effects will occur. This region is called the limited proportionality. If the electric field is further increased, the amount of ions will decrease the electric field such that the avalanche cannot continue and we speak of the Geiger-Mueller region.

The lateral extend of the avalanche is typically in the order of 10–100 μm and is mainly ascribed to the diffusion of the electrons and electrostatic repulsion. Another important effect is the generation of UV photons. As already described in section 2.2, photons are emitted during the ionization process whose energy depends on the excitation of the atoms and thus on the energy transfer. Photons emitted in the amplification process are mainly UV photons and could propagate through the medium causing a lateral extension of the avalanche. It is even possible that an UV photon can cause a breakdown of the avalanche by triggering a second avalanche further away. The photon propagation can be reduced by using quench gases, typically organic gases, which have relative high absorption cross sections for UV photons. Frequently used gases are carbon dioxide (CO_2), alkanes ($\text{C}_i\text{H}_{2i+2}$), ethylene, etc.

2.4.1 Townsend coefficient and gain factor

Charge amplification is a very complex process involving many contributions from different processes such as ionizations, excitations, scattering, repulsion, etc. A theory on molecular level to describe the avalanche does not exist. However, from a macroscopic point of view the increase of electrons dN per path length ds can be described by:

$$dN = N\alpha ds. \quad (2.28)$$

α is called the (first) Townsend coefficient (expressed in cm^{-1}). It depends on the electric field because the field indicates the mean energy between two collisions and hence the amount of ionization. Below a certain threshold E_{min} , the field is too weak to trigger an avalanche and the Townsend coefficient is zero. As a function of the electric field, the Townsend coefficient is plotted in Fig. 2.5 for common used gases. This plot is obtained from Monte Carlo simulations with Magboltz. The dependence of α on the electric field makes it difficult to integrate Eq. 2.28 analytically in nonuniform fields. In general, without the knowledge of the relationship $\alpha(E)$ (with $E = |\mathbf{E}|$), the solution of this equation is given by:

$$\frac{N}{N_0} = \exp \left[\int \alpha(s) ds \right] = \exp \left[\int \alpha(E) \frac{ds}{dE} dE \right]. \quad (2.29)$$

The ratio N/N_0 , with N_0 the amount of initial electrons is called the avalanche gain or gas gain. This gain does not necessarily corresponds to the effective gain of the detector as the electrons are not all captured by the readout electrodes. The first Townsend coefficient α depends on the gas mixture (i.e. on the ionization cross sections) and environmental properties (density, pressure, temperature). With ρ the density of the gas mixture, it is experimentally found that the following relationship is valid:

$$\alpha(E, \rho) = f(E/\rho)\rho. \quad (2.30)$$

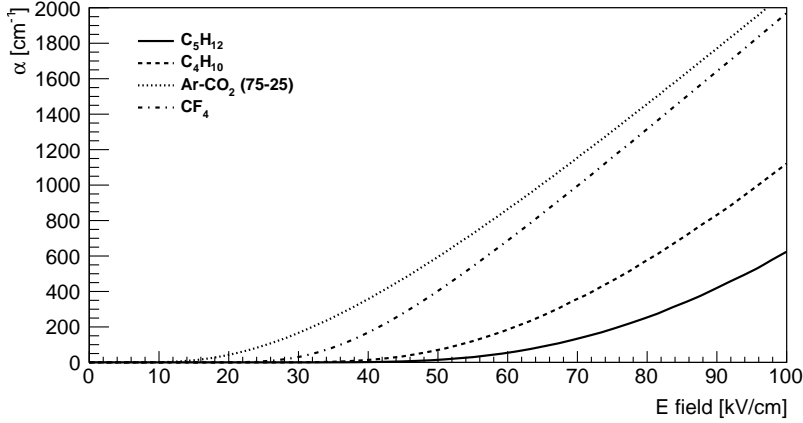


Figure 2.5: Simulated Townsend coefficients for common gases used in this paper, as a function of the electric field. Plots obtained with Magboltz simulations and may slightly differ from experimental results (see 4.2.2).

2.4.2 Gain fluctuations

Many processes cause fluctuations of the gas gain factor G . They can be categorized in statistical and local variations. The latter is a combination of effects such as pressure variations, mechanical imperfections, space-charge variations due to ions, etc. The statistical fluctuation is a result of the random nature of the multiplication process. We only concentrate here on the statistical fluctuations, because these are especially suited to study with Monte Carlo simulations. In strong non-homogeneous fields, the calculations were performed by Alkhazov[12] and he showed that the statistical gain distribution is given by a Polya distribution:

$$P(n) = \left(\frac{\alpha}{\mu}\right)^\alpha \frac{1}{\Gamma(\alpha)} n^{\alpha-1} \exp\left[-\frac{\alpha n}{\mu}\right]. \quad (2.31)$$

In this equation, μ is the average gain and α is related to the root-mean-square value through:

$$\sigma^2 = \frac{\mu^2}{\alpha}. \quad (2.32)$$

In Fig 2.6, the Polya distribution is plotted for different values of μ and α . For $\alpha = 1$ the exponential distribution is obtained from where the normalization can easily be checked.

Originally, the work of Alkhazov was based on gain fluctuations in wire chambers having an $1/r$ dependence of the electric field. It turns out the Polya distribution can also be used for other gaseous detectors, even detectors with uniform fields.

2.4.3 Effective Townsend coefficient

In gas mixtures where the attachment coefficient is high, the attachment of electrons can limit the avalanche growth. By combining the attachment and avalanche process, the total change of electrons dN per unit distance ds is equal to:

$$dN = N\alpha ds - N\eta ds = N(\alpha - \eta) ds. \quad (2.33)$$

The factor $\bar{\alpha} = \alpha - \eta$ is called the effective Townsend coefficient. The gain G is then subsequently lower and can be calculated by:

$$G = \exp\left[\int (\alpha(E) - \eta(E)) \frac{ds}{dE} dE\right]. \quad (2.34)$$

Again, $E = |\mathbf{E}|$, the magnitude of the electric field.

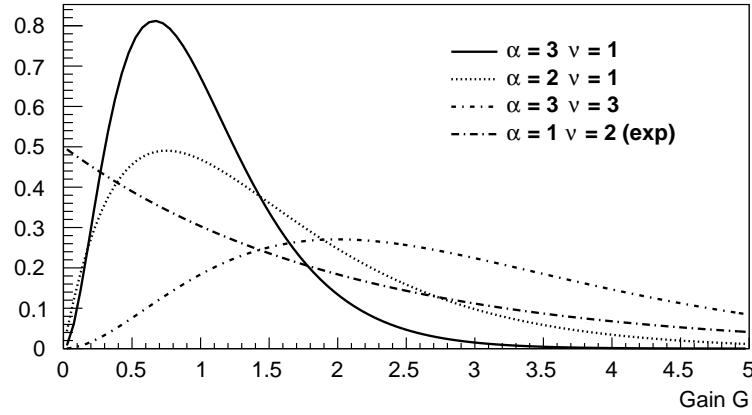


Figure 2.6: Polya distribution.

2.5 Signal creation

After the amplification process, the electrons drifts towards the anode, inducing a current signal which can be processed by the readout electronics. It is a common misunderstanding that the signal is created when the charge is collected on the electrode. In fact, every *moving* charge will *induce* a current signal on the surrounding electrodes, before the actual collection of the charge. The theory describing this charge induction is called the Shockley-Ramo theorem which will be introduced in this section.

A particle detector consists of dielectric materials and electrodes which can be regarded as equipotential surfaces. The total system can be described with a capacitance matrix C_{nm} , defined as:

$$Q_n = \sum_{m=1}^N C_{nm} V_m, \quad (2.35)$$

if the detector consists of N electrodes with charge Q_n and potential V_n . The reciprocity theorem relates two different configurations of \mathbf{V} and \mathbf{Q} having the same capacitance matrix through:

$$\sum_{n=1}^N Q_n V'_n = \sum_{n=1}^N Q'_n V_n. \quad (2.36)$$

Furthermore, due to Gauss's law, the sum of the charges on the electrodes is equal to the sum of the charges between the electrodes.

Consider now a gaseous detector with N electrodes (readout strips, cathode, etc.), and one wants to calculate the charge induced on electrode 1 from a charge Q_0 at position \mathbf{x} inside the gas volume. The charge can be seen as an infinite small electrode at potential V_0 . To continue, we consider two electrostatic configurations. In the first configuration all the electrodes are grounded ($V_i = 0, i > 0$) and have charges Q_i . The second (virtual) configuration is defined when electrode 1 has a potential equal to 1 (i.e. $V_1 = 1$) whereas the others are kept at ground potential ($V_i = 0, i > 0$) and the charge Q_0 is set to zero. For this configuration, the potential must be calculated inside the medium and this potential is called the weighting potential of electrode 1, denoted as $\psi_1(\mathbf{x})$. After applying the reciprocity theorem, one immediately obtains:

$$qV_0' + Q_1V_w = 0 \quad \text{or} \quad Q_1 = -\frac{q}{V_w}\psi_1(\mathbf{x}), \quad (2.37)$$

where V_w is the weighting potential which has been set to one ($V_w = 1$ V). The induced current can be calculated as:

$$I_1(t) = -\frac{dQ(t)}{dt} = \frac{q}{V_w} \nabla \psi_1(\mathbf{x})(t) \cdot \frac{d\mathbf{x}}{dt} = -\frac{q}{V_w} \mathbf{E}_n(\mathbf{x}(t)) \cdot \mathbf{v}(t). \quad (2.38)$$

This result is called the theorem of Shockley-Ramo. For the electrode of interest, the weighting field \mathbf{E}_n must be calculated from which the induced current can be calculated.

When a charge q at initial position $\mathbf{x}_0(0)$ starts to move according to a path $\mathbf{x}(t)$, the total induced charge at $t = t_1$ can be calculated as:

$$Q_n^{\text{tot}} = \int_{t_0}^{t_1} I_1(t) dt = -\frac{q}{V_w} \int_{t_0}^{t_1} \mathbf{E}_n(\mathbf{x}(t)) \dot{\mathbf{x}}(t) dt = \frac{q}{V_w} (\psi_1(\mathbf{x}_1) - \psi_1(\mathbf{x}_0)), \quad (2.39)$$

and is independent of the path of the trajectory. Electrons are created together with ions and both charges will contribute to the signal on an electrode. For example, if at t_0 the electron-ion pair is created, at time t_1 they will be at positions \mathbf{x}_1 and \mathbf{x}_2 respectively. From the result above, the total induced charge from both electron and ion on the anode electrode n is given by:

$$Q_n^{\text{tot}} = Q_n^e + Q_n^i = \frac{q}{V_w} (\psi_n(\mathbf{x}_1) - \psi_n(\mathbf{x}_2)). \quad (2.40)$$

If both charges are collected on the anode and cathode electrodes respectively, the total induced charge is Q_n^{tot} because $\psi_n(\mathbf{x}_2) = 0$ due to the definition of the weighting field. Hence, the *total* induced charge on an electrode is equal to the total collected charge on that electrode, when all the other charges are also collected on other electrodes.

2.6 Readout electronics

The raw signal induced on the electrodes must be processed in order to extract information from it. The choice and design of the electronics is a rather difficult task which, in general, depends on the application such as timing or charge measurement. Furthermore, different side effects has to be taken into account that limits the flexibility. One such side effect is the noise produced by the electronics. This random noise is superimposed on the signal pulse and the electronics have to be designed to keep the noise as low as possible such that, above all, the signal can be distinguished from noise. Especially for timing purposes the noise must be as low as possible because any additional fluctuation on the signal will result in an additional uncertainty on the time of the pulse (see later chapters).

Notwithstanding the flexibility in design, some elementary operations must be fulfilled. As the raw signal is very weak, it must be amplified with a very sensitive and low noise amplifier. This amplifier, called the preamplifier, is placed as close as possible to the readout electrode. After the preamplifier the signal is shaped according to an appropriate function, such as a Gaussian. The shaped signal is again amplified with a large factor. The purpose of the signal processing is to obtain an well-known signal shape for a given incident particle in the detector. A discriminator and/or analog-to-digital converter (ADC) can then be used to digitize and store the signal with its properties (time, pulse-height, etc.).

We will not go into detail regarding the electronics but rather treat it as a black box with a known transfer function $H(s)$ in the Laplace domain with $s = j\omega$, the Laplace variable. However, some specific electronic circuits will be briefly discussed in the next chapters.

Chapter 3

Gas Electron Multipliers

In this chapter the Gas Electron Multiplier (GEM) is introduced. We discuss the typical geometry, electrostatics and performance with the use of the concepts in the previous chapter. The fabrication of the GEM foils and the manufacturing limitations are briefly discussed. Afterwards, the CMS triple GEM detector will be introduced together with a brief review of other applications.

3.1 The Gas Electron Multiplier

The GEM detector is a new type of gas detector developed by F. Sauli in 1997 at CERN [13]. In Fig. 3.1, a cross sectional diagram of a single GEM is shown with its basic elements. A GEM foil is located between two parallel plates, the cathode and the anode respectively. The volume in between is filled with gas. The upper volume is called the drift region and the thickness h_D is typically a few mm. The lower volume, the induction region has a thickness h_I which is typically one or two mm. The GEM foil, the characteristic element of this type of detector, is made of a thin insulating polymer (kapton) sandwiched between two metal-coated electrodes. Circular holes are perforated in the foil with a density of 50 to 100 holes mm^{-2} . The cross section of such a foil is shown in Fig. 3.2 and the common dimensions are listed in Table 3.1. The holes are conically shaped due to the manufacturing process but other shapes are also possible if other production processes are used (see section 3.3).

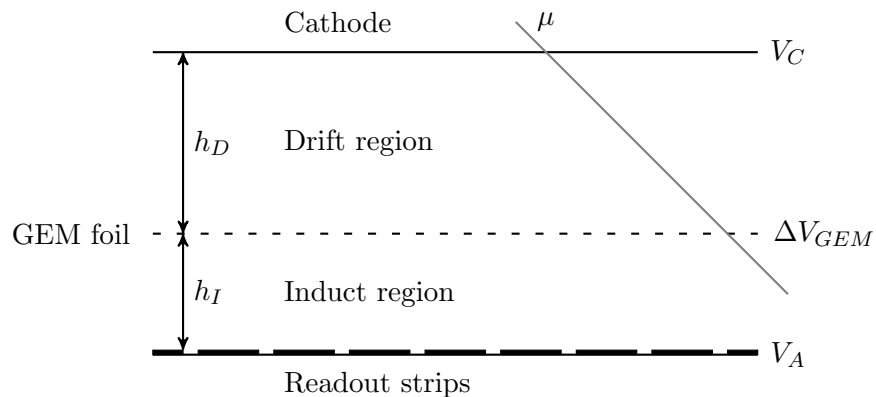


Figure 3.1: Cross section of a single GEM detector with readout strips. An incident muon ionizes the gas in the drift region producing primary electrons which drift to the GEM holes.

The electrostatic field in a single GEM detector is governed by three voltages, the drift voltage V_C , induction voltage V_A and a voltage V_{GEM} across the GEM foil. In practice, a voltage divider is used to correctly assign the voltage over each element. The electric fields inside the detector can either be modified by changing the voltages or the resistors in the

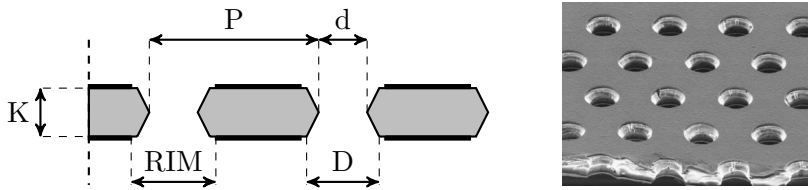


Figure 3.2: Left: cross section of a GEM foil with the kapton layer colored in gray and the metal coating in black. Right: scanning electron microscope (SEM) image [14].

voltage divider, or by changing the dimensions of the drift (h_D) and induction (h_I) region thickness (the thickness of the GEM foil is assumed to be fixed at $50 \mu\text{m}$). Typically, the voltage over each element or region is in the order of $300 - 600 \text{ V}$, but the electric field is very different because of the different dimensions. Especially the field in the GEM holes can reach 100 kV/cm when a voltage of 500 V is applied, provided the kapton thickness is $50 \mu\text{m}$. The GEM voltage is limited due to the breakdown of the kapton polymer or gas discharge, depending on the gas mixture.

Table 3.1: Typical GEM foil dimensions (units: μm). Other dimensions are possible depending on the fabrication process (see section 3.3).

Kapton thickness (K)	50	Inner hole diameter (d)	50
Metal thickness	5	Outer hole diameter (D)	70
Pitch (P)	140	Rim	70

The behavior of the electric field lines in a GEM detector is interesting because it governs the drift motion of the electrons and ions in the gas volume. If the electrodes are assumed to be perfect conductors, the electric field (and field lines) must be perpendicular to the surface. Without a GEM foil, the electric field lines are parallel to each other and perpendicular to the anode and cathode electrodes (cfr. capacitor). The presence of the GEM foil will distort the field only in the vicinity of the holes, as shown in Fig. 3.4(b) where the field lines are plotted in a GEM foil hole. At a certain distance from the hole, the external field lines from the anode-cathode are indeed parallel to each other and perpendicular to the GEM structure whereas the external field lines are squeezed together when approaching the hole. Together with the additional field lines from the GEM electrodes, a high field line density in the holes is obtained resulting in high electric field. Some of the field lines inside the hole terminate on the coated metal electrodes or on the kapton layer rather than passing through the hole and terminating on the anode or cathode.

The central hole potential $\psi(0, 0, z)$ along the z -axis (i.e. perpendicular to the electrodes) is shown in Fig. 3.3(b). This plot is obtained with the ANSYS simulation tool which will be discussed in the next chapter. The electric field along the z -axis can be calculated through $E_z = \partial_z \psi(x, y, z)$, i.e. the first derivative of the curve in Fig. 3.3(b). From this plot it is clear that the electric field changes only at the edges of the GEM holes, i.e. at $z = 2 \text{ mm}$ and $z = 2.06 \text{ mm}$. Inside both drift and induction regions and the holes, the field can be assumed to be constant.

3.1.1 Working principle and operation

A charged particle passing through the detector can ionize the gas in both drift and induction region. Only the primary and secondary electrons generated in the drift region will drift through the GEM holes, where an avalanche process will start due to the high electric field. The avalanche electrons drift towards the anode and a signal will be induced during their drift time. The hole can be regarded as a single amplification channel with a gain depending

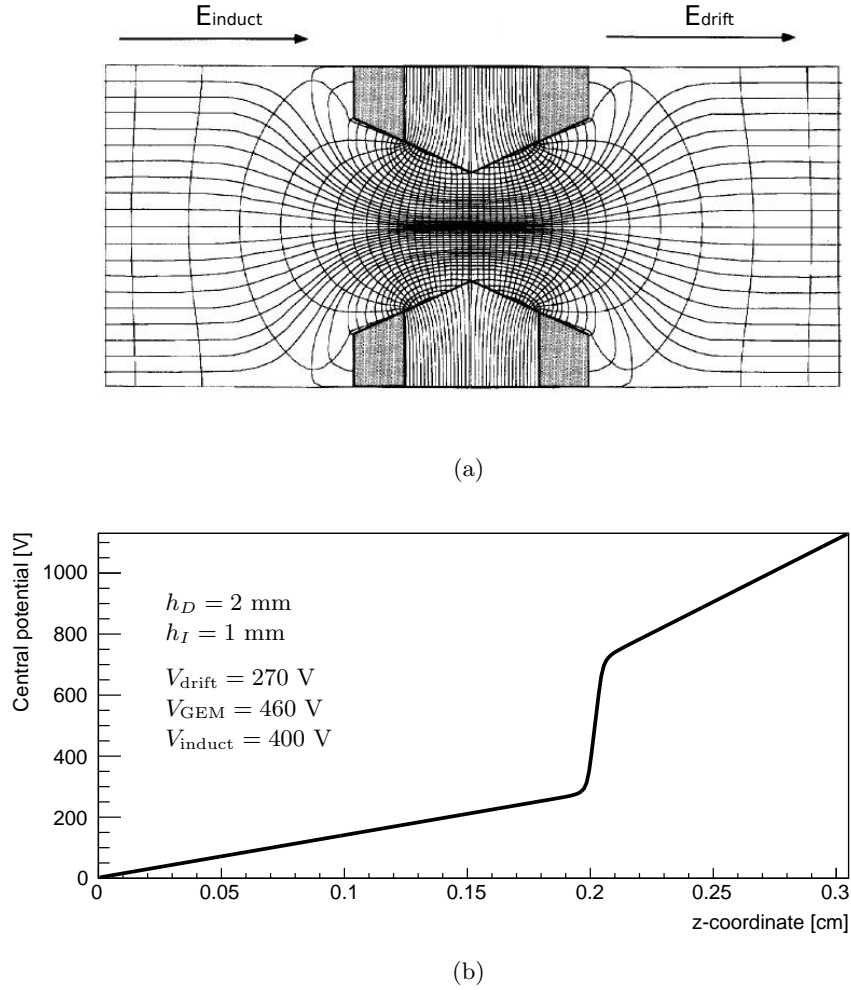


Figure 3.3: GEM electrostatics: electric field lines in a GEM hole [15] (a) and central potential of a single GEM detector (b). The GEM foil dimensions are given in Table 5.1.

on the GEM voltage and the gas mixture. The electrons liberated from primary ionizations in the induction region will not be amplified and their induced signal can be neglected. The ions slowly drift towards the cathode, inducing a small signal on the cathode which is spread out over the ion drift time, typically a few μs .

The voltages on the GEM electrodes, the gas mixture and the readout electronics must be adjusted depending on the desired quantity to measure and to achieve a high detection efficiency. For example, high incident particle fluxes requires fast detectors which restore fast to the equilibrium state such that the overlap in signal pulses reduced. The optimization of the time resolution by choosing an appropriate gas mixture and a set of voltages is the aim of the paper and is explained in Chapter 6.

3.1.2 Multiple GEM layers

The gain of a single GEM can be too low in order to induce a detectable signal, even after adjusting the GEM voltage. By inserting multiple GEM foils in the gas volume, the gain can be increased because the primary and secondary electrons must pass through multiple amplification stages resulting in a higher gain. For n GEM foils installed, n GEM potentials must be defined as well as $n - 1$ intermediate potentials between the GEM foils. These regions between the foils are called the transfer regions. If equal voltages are applied over the GEM

foils and the drift, transfer and induction voltages are approximately equal, the gain can be calculated in first order with a power law:

$$G_{\text{tot}} = G^n, \quad (3.1)$$

with G the (effective) gain of one GEM layer and n the amount of layers installed. From a simulation point of view, this approximation can reduce the computation time drastically because only a single GEM must be calculated. In this way it is only necessary to investigate single GEMs and extrapolate the results to multi-GEM configurations. Afterwards a final check must be performed by calculating the total multi-GEM configuration.

3.2 GEM performance

3.2.1 Detection efficiency

The detection efficiency is defined as the probability an incident particle will induce a detectable signal on the GEM readout plane. It depends on the applied voltages, the gas mixture and the readout electronics as we will discuss in this section. After the detector is built, the efficiency is plotted as a function of the applied voltage to obtain an efficiency curve which has typically a sigmoid shape (see section 3.4). From these curves it is possible to extract the voltage working point of the detector which corresponds to the desired detection efficiency.

From chapter 2 we know that the amount of primary ionization encounters is described by a Poisson distribution with mean L/λ , where L is the thickness of the active region and λ the mean-free-path between two ionization encounters (depending on the gas mixture and the charged particle). The ionization efficiency η is defined as the probability that a charged particle will cause at least one ionization encounter in the drift region. To obtain a relationship between η and the parameters L and λ , we first calculate the probability for zero encounters:

$$P(L/\lambda, 0) = \exp(-L/\lambda). \quad (3.2)$$

A minimum ionization efficiency η_0 is obtained when:

$$P(L/\lambda, 0) = \exp(-L/\lambda) < 1 - \eta_0. \quad (3.3)$$

The minimum drift region thickness L_{min} for a given λ can then be calculated as:

$$L_{\text{min}} = -\lambda \ln(1 - \eta_0). \quad (3.4)$$

For example, the cluster density for 100 GeV muons in Argon is $\lambda^{-1} = 35$ /cm (see Fig. 2.1). Hence, the minimum drift region thickness must be equal to 0.8 mm for a 95% ionization efficiency.

Due to attachment and recombination there is a probability the primary electrons will disappear before they reach the GEM hole and trigger the avalanche. These effects, of course, affects the total efficiency of the detector and must be suppressed by choosing an appropriate gas mixture such that the attachment and recombination coefficients are as low as possible. Furthermore, some external field lines terminate on the top GEM metal electrode and a primary electron can be captured on this electrode yielding a decrease in the total detection efficiency. The amount of external field lines terminating on the top metal electrode mainly depends on the hole density, which must be high enough. A quantity related to this is the electrical transparency. It is defined as the ratio of the field lines passing through the GEM holes divided by the total external field lines produced by the cathode-anode. It can be calculated using FEM software packages or with Monte Carlo simulations. In first order, the

electrical transparency can be approximated with the optical transparency τ , defined as the area of the GEM holes divided by the total area:

$$\tau = \frac{\pi D^2}{4P^2} = 0.196. \quad (3.5)$$

In this calculation the dimensions in Table 3.1 were used. As a general rule, to increase the GEM hole collection efficiency, the attachment coefficient must be as low as possible and the amount of primary electrons must be as high as possible. This can be achieved by choosing an appropriate gas mixture with a high cluster-size distribution, i.e. the amount of electrons per cluster. The amount of clusters can be increased by changing the dimensions of the drift region.

3.2.2 Effective gain

After the avalanche process, a dense cloud of electrons is located at the bottom of the GEM hole(s). Because some field lines terminate on the kapton and bottom GEM electrode, it is possible that the avalanche electrons will be collected on these layers, resulting in a decrease of the gain. This amount can be very high, up to 60% of the created avalanche electrons, depending on the electric field and GEM hole geometry. Furthermore, when electrons are not collected but drift towards the anode, a small fraction will be attached to the gas atoms due to attachment. This effect is only important when the attachment coefficient is very high in the induction electric field. These processes lead to a decrease in the detector gain, and an effective gain G_{eff} is defined as the total collected charge at the anode, divided by the amount of primaries. Besides statistical fluctuations, the effective gain is related to the avalanche gain by a constant factor:

$$G_{\text{eff}} = \xi G, \quad (3.6)$$

where ξ can only be obtained with simulations. Typical values for ξ are 0.4–0.6.

3.2.3 Charging up

Because kapton is an insulator, electrons collected by the kapton are trapped on the bottom side of the kapton. Ions on the other hand will drift slowly upwards and some will be trapped on the top half of the kapton. When accumulating more electrons and ions, the space charge will distort the electric field until an equilibrium state is reached. This equilibrium state is comparable to a charged capacitor, resulting in a higher electric field in the holes and subsequently higher gains. It is important that this effect only appears after a certain time, depending on the incident particle rate.

3.2.4 Energy resolution

The energy resolution is defined as the uncertainty on the pulse height at the anode due to statistical fluctuations during the avalanche process. Measurements of the energy of the incident particle is only possible when the particle (e.g. photons) is absorbed in the drift region, where all its energy is deposited and converted to primary and secondary electrons. The pulse height spectrum can be fitted to a Gaussian and the energy resolution is defined as the FWHM at the mean peak position. Initial studies on single GEMs shows an energy resolution of 18% at 5.9 GeV photons [13]. The experimental setup on how the energy resolution can be measured will be discussed in chapter 5

3.2.5 Spatial resolution

In order to achieve information on the position of the incident particle, the anode readout plane must be fragmented in independent transverse readout planes. Both dimensions of the fragments and the GEM hole density determine the spatial resolution, i.e. the uncertainty to resolve the initial track position. Different methods are possible such as strips for 1-dimensional tracking, a two-dimensional grid of tiles for two-dimensional tracking, or wires. Excellent spatial resolutions in the order of $100\ \mu\text{m}$ have been obtained with single and triple GEMs, even in the presence of high magnetic fields (see section 3.4).

3.2.6 Time resolution

All the processes in a gaseous detector such as primary ionization, avalanche and drift, are stochastic processes and uncertainties are introduced. Hence, it is not possible to exactly retrieve the space and time coordinates of an incident particle, but it is only possible to extract information within a given uncertainty range. The time resolution is a measure for the uncertainty of the time coordinate measured by the electronics when an incident particle is registered. Current GEM detectors have time resolutions in the order of 5–10 ns but it is possible to achieve better time resolutions as will be discussed in the next chapters. For such optimization it is necessary to track the electrons on atomic level and investigate the individual uncertainties of the different processes.

3.2.7 Other advantages

As already discussed in the introduction and in the previous paragraphs, the GEM detector combines both excellent spatial and time resolutions into one single detector which is a great advantage because in the past the tracking and timing information was obtained by using two detectors separately (e.g. a MWPC with a scintillator). Furthermore, high rates up to $500\ \text{kHz}/\text{cm}^2$ could be obtained because the ions are collected very fast. Aging tests shows no degradation of the GEM performance and could reach up to tens C/cm^2 over a period of 10 years. Because the electric field is focused in the GEM holes, GEMs could operate at lower voltages in the order of 1–5 kV (cfr. RPCs which operate at 10 kV), reducing the power and the noise levels. The noise is even further reduced as the readout electronics could be separated from the High Voltage (HV) structure if the anode is grounded.

3.3 Production process

The production of GEM foils comprises different steps and is similar to the fabrication of printed circuit boards where a photolithographic process is employed. We only explain the single and double mask process here, which are schematically shown in Fig. 3.4. This text is a summary of the production process as explained in [16].

The original and most common process is the double mask process. The starting point is a $50\ \mu\text{m}$ kapton foil with $5\ \mu\text{m}$ copper electrodes coated on both sides. Next, a photoresist is coated on both metal electrodes. With a computer and laser techniques, two masks are created with perforated holes according to the GEM hole pattern. The mask hole diameter is equal to the outer GEM hole diameter. Both masks are placed on the photoresist and optically aligned to each other with an accuracy of $5\ \mu\text{m}$. After exposing both sides with UV light, the photoresist is removed at the holes and the metal in the holes can be removed by etching with appropriate acids. In the last step, the kapton is etched on both sides yielding a bi-conical hole shape.

The major problem with the double masked technique is the alignment of the both masks on the metal layers. A precision of $5\ \mu\text{m}$ allows to make small-scale foils with dimensions up

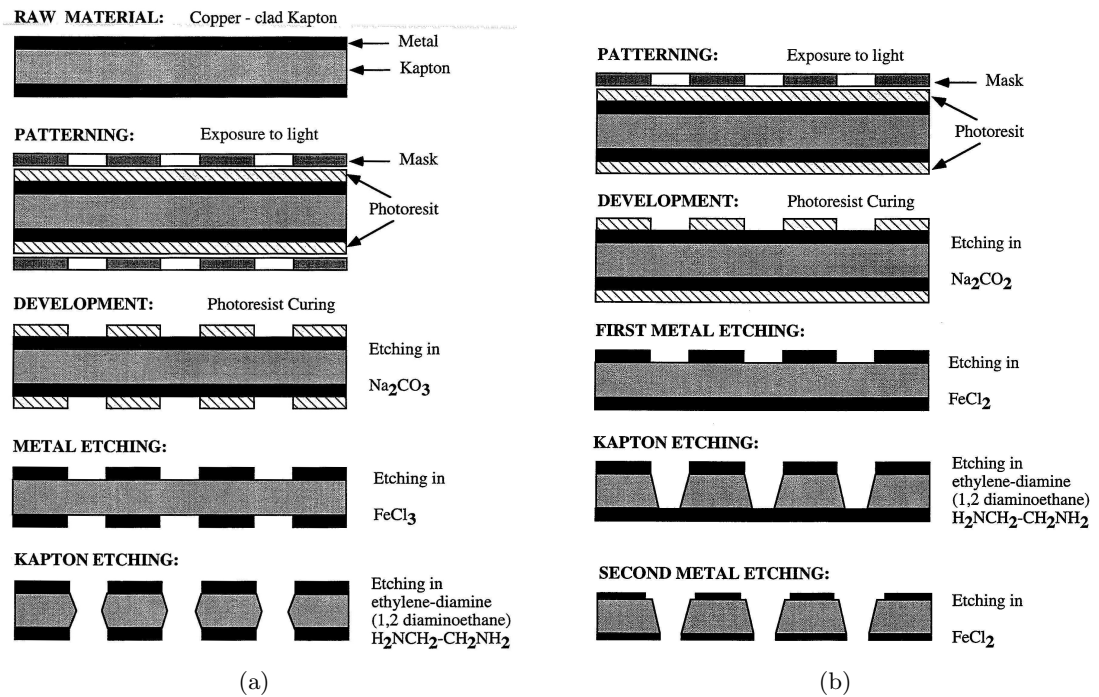


Figure 3.4: Schematic process of two common GEM foil manufacturing methods: double masked (left) and single masked (right). Figure adapted from [16].

to 50 cm. When larger foils are needed to be produced, such as the foils for the CMS triple GEM, another manufacturing method such as the single mask process must be used. This process is the same as the double masked process except that only one side of the GEM foil is masked, exposed to UV light and etched. The kapton etching yields a single conical shape hole and a second etching of the lower metal is needed. As the metal is not covered with protective materials, the metal must have twice the desired thickness before the final etching because the etching is uniform as performed in a bath of acid.

A lot of research on the production of large-scale GEM foils has been performed through the years. With specialized etching techniques it is possible to obtain approximately a bi-conical hole shape or cylindrical shapes [17]. Nowadays the GEM foils are industrially manufactured and the dimensions cannot be changed.

After the production process, the GEM foil is cleaned with floating water, deionized water, demineralized water and alcohol. The foil is dried in air at 80 degrees and the electrical connectors are added. An Omhic test is performed where the foil must exceed around $2\text{ G}\Omega$. The foil is now ready to be installed in the detector housing where it is clamped at the edges of the detector.

3.4 The CMS triple GEM

As already explained in the introduction, new triple GEMs are proposed for installation in the forward high η -region in CMS (GE1/1) during LS2. The present technology with RPCs is not able to cope with the expected high radiation environment and new detectors needed to be developed. The choice for GEM detectors was based on its properties such as high rate capabilities, excellent spatial and time resolutions, radiation resistant and operational in high magnetic fields. In this section, the developments of the CMS triple GEM is briefly described. This text is based on [6], [18] and [19].

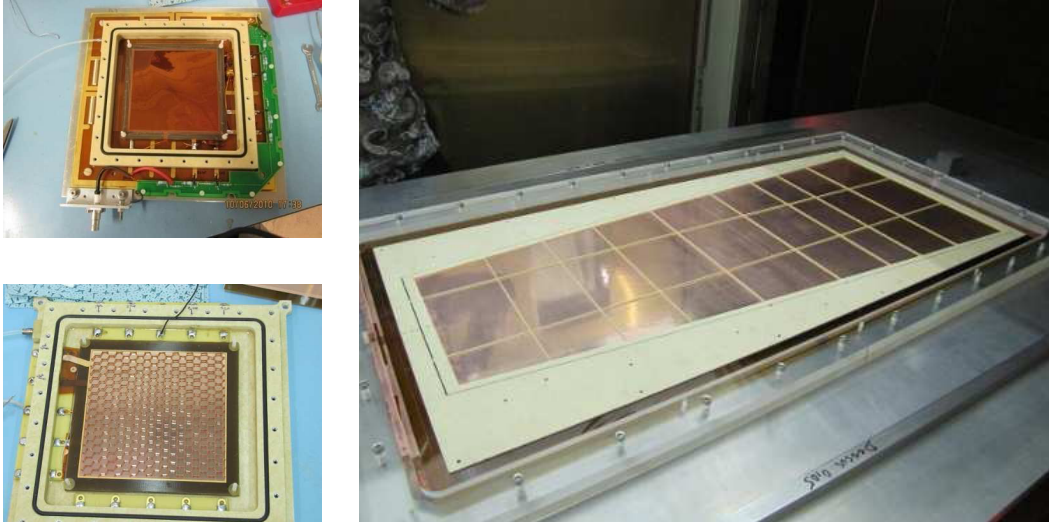


Figure 3.5: GEM prototypes: double mask (top left), double mask with honeycomb spacers (bottom left) and full single mask GE1/1 prototype with the 3/1/2/1 configuration during gluing of the spacer frames (right). Figure adapted from [16].

3.4.1 Initial studies

In 2009, a research program is started to perform R&D studies on the new CMS triple GEMs. Initially, small triple GEM prototypes were developed, measuring $10 \times 10 \text{ cm}^2$ in two configurations: 3/2/2/2 and 3/1/2/1 mm (respectively drift, transfer1, transfer2 and induction thickness). The readout consists of 128 strips with a pitch of 0.8 mm. The GEM foils used were manufactured with the double mask technique and, therefore, an additional prototype with the single mask technique is tested with an eye to the development of large scale foils. The dimensions were 3/2/2/2 mm with 256 strips having a pitch of 0.4 mm in two perpendicular directions. A last prototype was built with honeycomb spacers to avoid the stretching of the GEM foils during the detector assembly. In Fig. 3.5 (left), the standard double mask and the honeycomb prototypes are shown. However, the latter is not further discussed here. The electronic VFAT chip developed for the TOTEM GEMs was used as readout electronics for processing the signals. However, the readout electronics which will be installed on the triple GEMs in 2019 are still under development (VFAT3).

The prototype GEMs were tested with a 150 GeV muon and pion beam at the CERN SPS H4 beam line and the results are shown in Fig. 3.6. Two gas mixtures were investigated: the standard Ar-CO₂ (70-30) and the Ar-CO₂-CF₄ (45-15-40) mixture. A spatial resolution of 270 μm for the first prototype (3/2/2/2) is achieved (see Fig. 3.6(a)). The histogram was fitted to a shifted Gaussian with an additional first order polynomial to describe the noise. Furthermore, no strong influence of the spatial resolution on the gas mixture and the dimensions was observed. However, the best cluster size distribution was obtained with the 3/1/2/1 configuration. The time resolution was measured with two scintillators serving a trigger signal, and the spread (RMS) of the arrival time of the signals is plotted in the Fig. 3.6(b) as a function of the drift voltage. A strong dependence on the drift field is observed and a time resolution of 4 ns is obtained with the Ar-CO₂-CF₄ mixture. This behavior will become clear in chapter 6. The efficiency curves of both double and single mask as a function of the gain are plotted in Fig. 3.6(c) and 3.6(d) respectively. An efficiency of 98% is reached with gains above 8 kV for the double mask whereas this high efficiency for the single mask GEM is shifted towards higher gains. We conclude that the best performances are obtained with the 3/1/2/1 gap configuration with the Ar-CO₂-CF₄ mixture and almost no difference in performance for both double and single mask foils was observed.

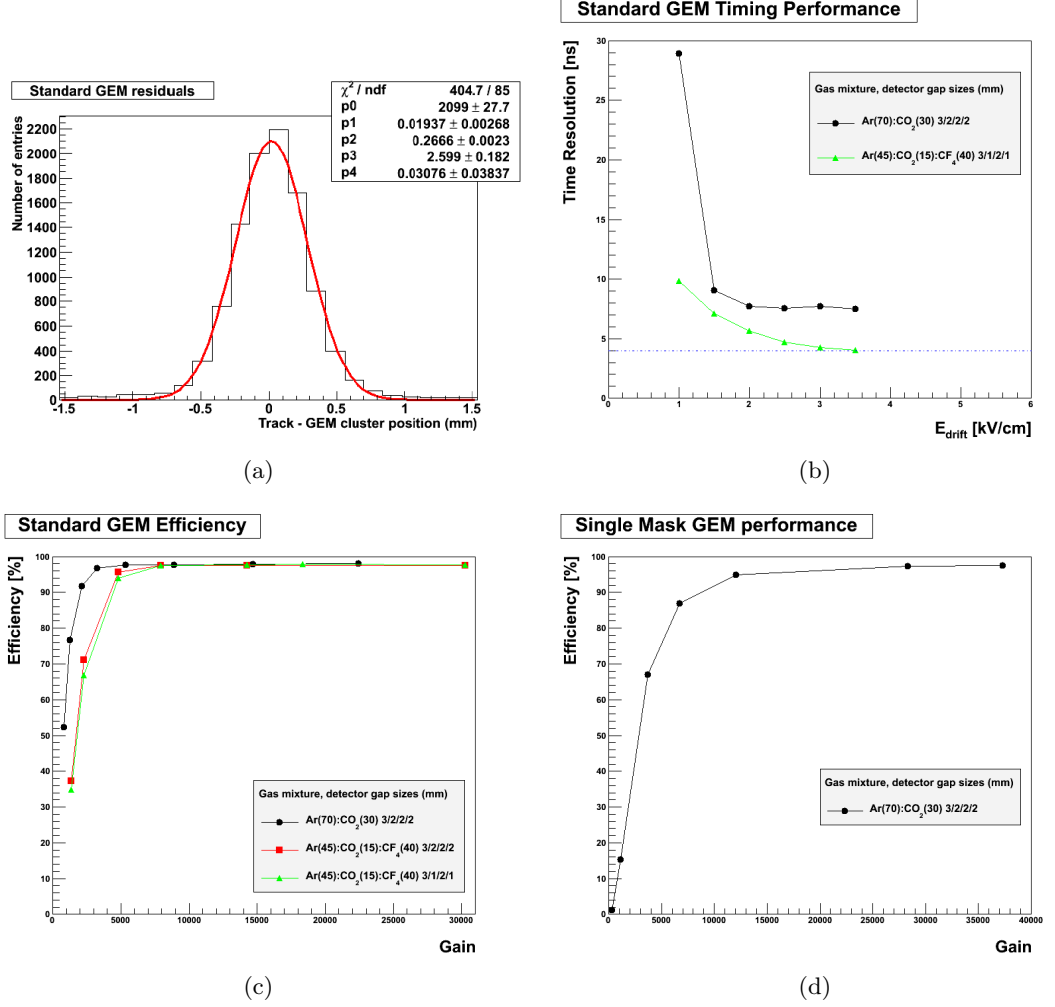


Figure 3.6: Beam test results for both small CMS triple GEM prototypes: spatial resolution (a), time resolution (b), efficiency (c) and efficiency for the single mask prototype (d).

3.4.2 GE1/1 prototype

After the successful initial results on the single mask GEMs, a large-scale triple GEM prototype was constructed. A trapezoidal single mask GEM with the 3/1/2/1 configuration was built (see Fig. 3.5, right) which covers 10° in azimuth and equipped with readout strips pointing towards the LHC beam pipe, having on average a pitch of 0.9 mm. To improve tracking capabilities, two GEMs are housed face-to-face in a super chamber. Beam line test results with a Ar-CO₂-CF₄ (45-15-40) are shown in Fig. 3.7. An efficiency of 98% is obtained at ≈ 4200 V which corresponded to a gain of 7000 and a spatial resolution of $268 \mu\text{m}$ is obtained. These results proved the successful R&D studies and a full prototype of this type will be installed during the short technical winter stop in 2016–2017.

3.5 Applications

GEM detectors are also used a broad range of other applications. In the following we will briefly discuss three main applications. For a more complete list, see [14]. Although the principles are the same, the applications differ from the HEP particle detectors on the type and energy range of the incident particles. Indeed, as this paper deals only with high relativistic muons, the results are not in general applicable to other particles with a lower energy.

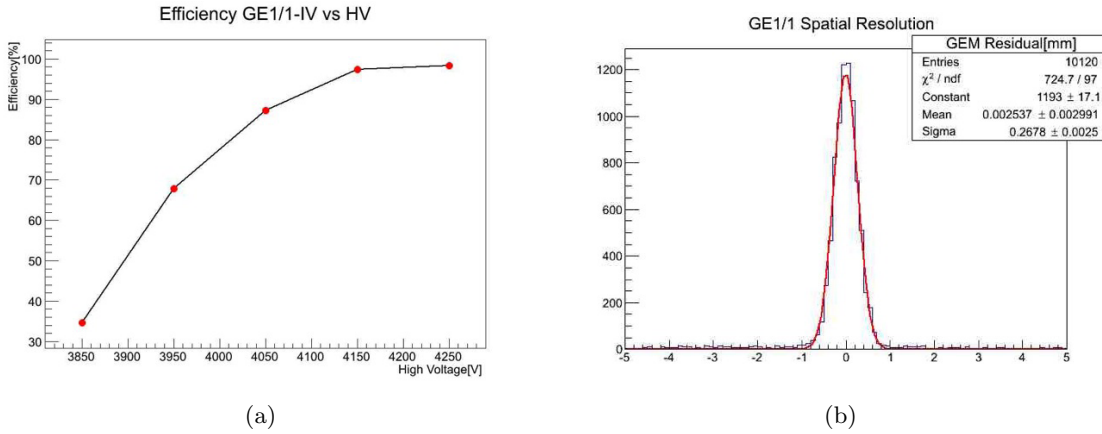


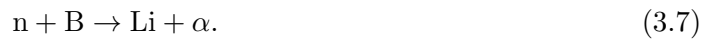
Figure 3.7: Beam test results for CMS GE1/1 triple GEM prototype: efficiency (a) and spatial resolution (b).

3.5.1 Photon detection

Photons can directly be detected when the photon interacts with the gas atoms in the drift region, liberating primary electrons. However, the interaction rate with the gas atoms is very low, and not all the incoming photons are detected, resulting in a very low detection efficiency. This can be improved by adding a semitransparent photocathode layer (e.g. CsI) at the cathode, optionally combined with a reflective photocathode at the top metal GEM electrode. The photon interacts with the photocathode and releases electrons via the photoelectric effect. These electrons act as primary electrons and can be detected in the traditional way. Because of the excellent GEM properties such as position and time resolution, such GEMs are competitors of photomultipliers (PMTs) [20].

3.5.2 Neutron detection

Neutrons cannot directly be detected in a gas medium because it is not possible to ionize the gas atoms. It is possible, however, to use Boron (B) to absorb the neutron and trigger a nuclear reaction:



Other conversion reactions are also possible. The α -particle has an energy in the MeV range and can ionize the gas in the drift region, creating a detectable signal. The boron can be present in the detector as a solid layer at the cathode or by using a gas mixture containing boron (e.g. BF_3).

3.5.3 Medical applications

GEMs are more often used in medical applications due to their good position and time resolution. A good position resolution is required by medical imaging with soft X-rays. The detection efficiency for X-rays can be enhanced by using photocathodes as described above, sensitive in the soft X-ray region. The combination of the time resolution (order of 10 ns) and the position resolution is used for example in PET scanners in order to retrieve the initial coordinates of the positron. Decreasing both the uncertainty on the position and timing result in an even better determination of the decay position, and hence the position of a tumor.

Chapter 4

Simulation software

Monte Carlo simulations of particle detectors require software packages that model the detector as well as the primary ionization and the charge transport inside the detector. Depending on the needs and computation time, one can use different models, each operating within a specific domain in the parameter space (e.g. energy) where the result is accurate and valid. For example, the primary ionization can be modeled by using the Bethe equation or the photo-absorption ionization model. As a GEM detector has a rather complex geometry and electric field, detailed simulations must be performed in order to have accurate results. The purpose of this chapter is to give an overview of the simulation software tools used in order to assess accuracy of the simulation. Different programs and algorithms are used for each specific process which will be discussed further on.

The software package ANSYS Inc. [21] is used to calculate the potential for a fixed set of boundary conditions, i.e. for a fixed set of voltages applied on the electrodes. Garfield++ [22] is then used for the calculations of the primary ionization, charge transport and signal creation. This software package combines different standalone programs each taking care of a specific process. Finally, ROOT [23] is used to analyze the results. To work efficiently with these programs, a local simulation environment is set up which acts as an interface between the different software packages. This will be discussed at the end of this chapter.

4.1 ANSYS

ANSYS is a broad used engineering simulation software package that is able to calculate electronics, fluid dynamics, structural mechanics, etc. The keystone of this simulation package is the Finite Element Method (FEM), a technique for solving differential equations in 2D or 3D structures. Within this technique, the volume is divided in cells, the number of cells depending on the accuracy, and the differential equations are solved inside each cell by taking the boundary conditions into account. The boundary conditions depend on the quantity of interest (e.g. electric or magnetic field) and follow from the underlying theory. The solution is then obtained by minimizing a functional by using variational methods. In the case of GEM detectors, the potential $\psi(\mathbf{r})$ is calculated in ANSYS from where the electric field can be derived: $\mathbf{E} = -\nabla\psi(\mathbf{r})$. The FEM elements are 10-node-tetrahedrons with curved sides and the potential is solved by expanding $\psi(\mathbf{r})$ in polynomials of order n . This results in a less accurate field calculation as the field will be described with a polynomial of order $n - 1$.

4.1.1 GEM unit cell

Solving the potential in the complex GEM geometry requires in the first place a detailed formulation of the geometry and the materials used. For the electrostatic calculations, it is assumed the GEM detector is infinitely spread out in the plane of the GEM foil. From the

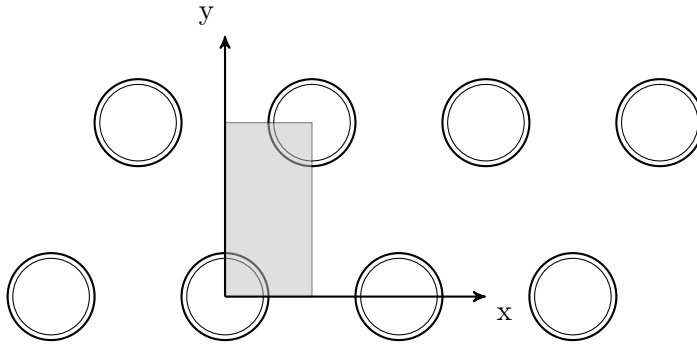


Figure 4.1: Top view of the GEM foil. The unit cell is indicated with a gray box containing half a GEM hole, with a thickness equal to the total GEM thickness.

staggered hole positions in the GEM foil, a periodic rectangular unit cell structure can be defined. In Fig. 4.1, the top view GEM foil is plotted and an (x, y) -coordinate system is defined. The origin of the cell is defined as the midpoint of one hole, the opposite side has coordinates $(P/2, \sqrt{3}P/2)$, because the diagonal of the projected cell is equal to the pitch P . In the z direction, the unit cell is limited between the drift plane at $z = 0$ and the readout plane at $z = d_{\text{tot}}$. For a single GEM, the total thickness $z = d_{\text{tot}}$ is equal to:

$$d_{\text{tot}} = h_D + h_I + K + 2d_m, \quad (4.1)$$

with h_D the drift region thickness, h_I the induction region thickness, K the kapton thickness and d_m the metal thickness. For multi-GEMs with n layers, the total thickness consists n times the metal-kapton-metal layer, the drift and induction region thickness and the $n - 1$ transfer region thicknesses.

4.1.2 Input file

There are two ways to define the unit cell geometry in ANSYS. The first one is the Graphical User Interface (GUI) where the unit cell must be constructed by drawing the cell in 3D. It is also possible to import geometries from AutoCAD drawings, a method which is more common for civil engineering purposes. The other method is by writing a script with predefined ANSYS instructions. These instructions allow to make elementary volumes such as blocks, cylinders, cones, etc. The instructions must be written chronologically in a text file and must be imported in ANSYS, which reads the instructions and compiles the geometry. For geometries such as the GEM detector this method is the most suitable. The advantage of this script method is that the whole detector can be described within one text file, including the voltage boundary conditions and materials properties. The rather complex structure of the predefined instructions may be a disadvantage of this method because no visual aid is available. However, the script can be tested line by line to debug or adjust. We will now discuss the principle on how to define the geometry with text and figures in order to understand ANSYS. A complete input file describing a single GEM with explanation can be found in Appendix A.

The ANSYS instructions allow to create elementary volumes. To define the GEM unit cell from such elementary volumes, we first define the gas volume as a rectangular box enclosing the total unit cell. At the center of this block, three small blocks are added defining respectively the top GEM metal layer, the kapton and bottom metal layer (see Fig. 4.2(a)). Two quarter GEM holes at opposite side must be subtracted from the metal-kapton-metal layer. Referring to Fig. 3.2, only the kapton layer is conical shaped whereas the metal layers are straight. Hence, to subtract such a double conical shape from the kapton, two cones with

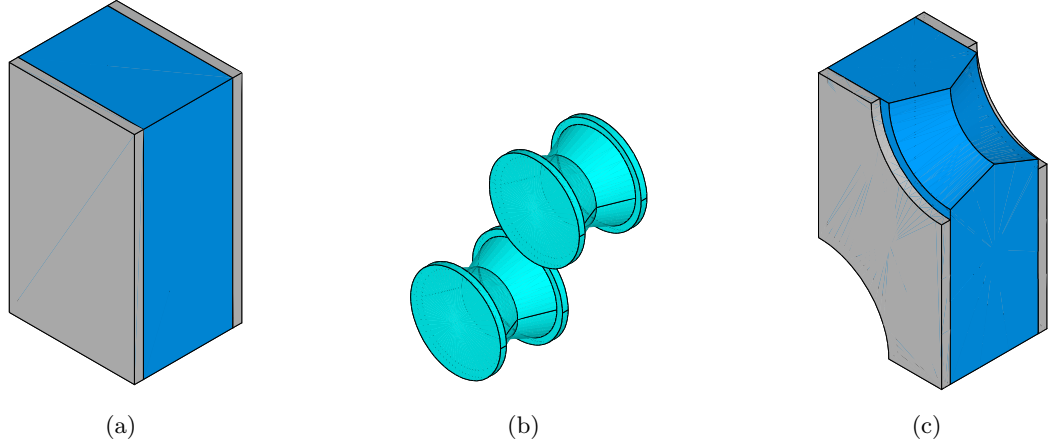


Figure 4.2: Elementary composed ANSYS volumes: metal-kapton-metal layer embedded in the gas volume (a), to be subtracted GEM holes (b) and total metal-kapton-metal layer with subtracted holes (c).

inner (d) and outer (D) radius must be created at the common GEM hole axes. Furthermore, two discs or flat cylinders with radius equal to the rim-value must be subtracted on both metal layers. These volumes, both cones and both cylinders are shown in Fig. 4.2(b) (left). After subtracting these volumes from the metal-kapton-metal layer, one obtains the result as shown in Fig. 4.2(c) (right). The anode and cathode metal electrodes does not have to be defined geometrically as they can be handled with the boundary conditions (see next section). After the subtraction, the conical and cylindrical volumes are removed, resulting in a complete described unit cell consisting of four volumes: the gas volume, two metal volumes and one kapton volume. The gas volume is shown in Fig. 4.3, where a rectangular coordinate system is introduced for further use.

4.1.3 Boundary conditions and electrostatic solution

To compute the potential $\psi(\mathbf{r})$, the volumes must be assigned to materials with a relative permittivity ϵ_r . The gas volume can be considered as vacuum ($\epsilon_r = 1$) whereas kapton has a relative permittivity of $\epsilon_r = 4$. The metal layers on the GEM foils are assumed to be perfect conductors with very high permittivity. A value of $\epsilon_r = 10^{10}$ is used in the simulations. Also the electrodes at the drift and induction planes are treated as perfect conductors. The voltages on the metal electrodes must be given as boundary conditions in order to solve the field. An additional boundary condition is that the electric field must be perpendicular to the metal surfaces, a consequence of the infinite conductance of the electrodes. The material properties and the voltages must also be defined in the input file as well as the periodic boundary conditions in the (x, y) -plane.

The solution of the potential is shown in Fig. 4.4. The drift and induction region shows only a small linear variation of $\psi(\mathbf{r})$ in the z -direction and electric field is then nearly constant in these regions. Large variations are present in the GEM hole region, together with an increased cell density for more accurate results, resulting in a strong non-uniform electric field. The field lines have a shape according to Fig. 3.4(b).

The weighting field or potential can also be computed when all the electrodes are set to zero potential, except the electrode of interest. This electrode is set to potential one and the potential is solved.

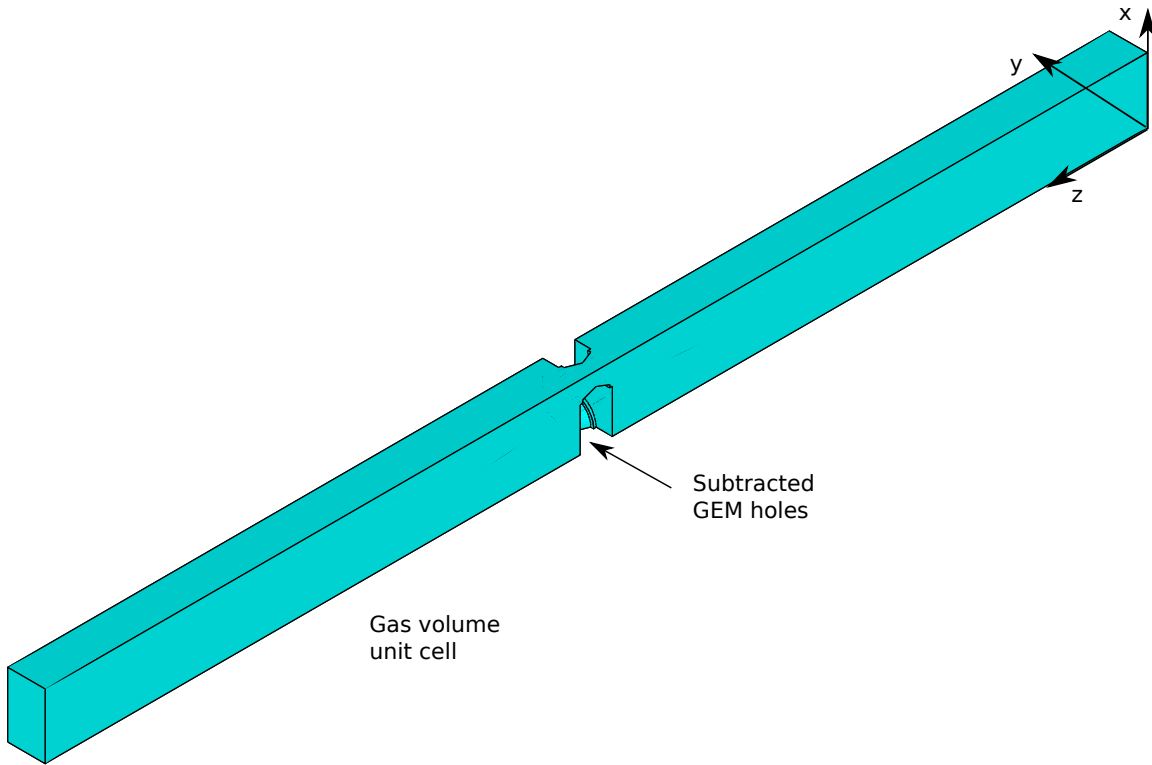


Figure 4.3: The gas volume unit cell with subtracted GEM holes in the middle. A rectangular coordinate system is introduced as shown.

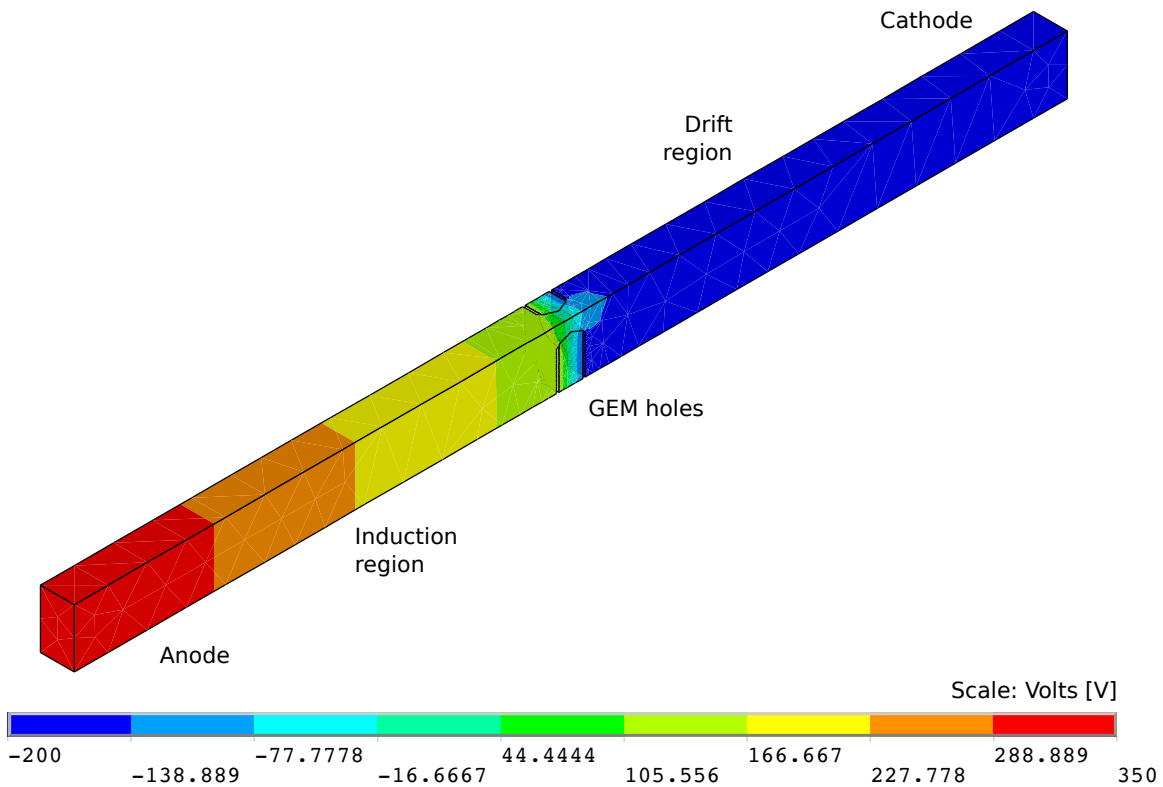


Figure 4.4: Computed potential $\psi(\mathbf{r})$. The scale accuracy does not correspond with the actual accuracy of the potential. The white lines in the volume defines the boundaries of the FEM elements.

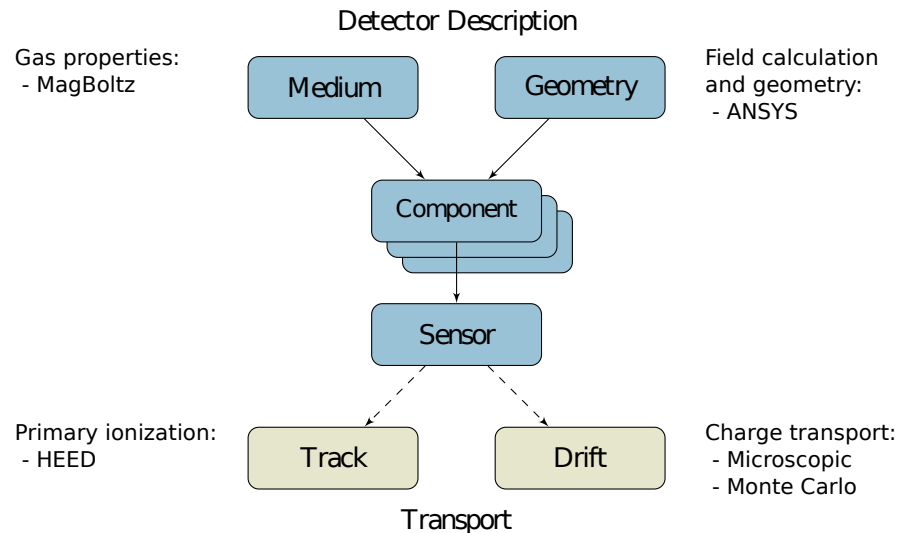


Figure 4.5: Garfield structure [25].

4.1.4 Output files

When the electrostatic field is solved, a field map can be saved containing the information about the FEM cells and the potential. In general, four output files are generated:

- ELIST.lis: contains the mapping of the FEM elements;
- NLIST.lis: the coordinates of the nodes are stored;
- MPLIST.lis: the materials are defined with their properties;
- PRNSOL.lis: the potential in each node is stored.

Typically for a single GEM, around 10000 elements are created together with 15000 common nodes. The FEM elements are more concentrated in places where large structural variations are present. The weighting field produces additionally an additional .lis file containing the nodal solutions of the potential. The field map and FEM elements are the same.

4.2 Garfield ++

Garfield++ is a software package used for detailed simulations of gaseous and silicon particle detectors. The first version was released in 1984 under the name Garfield [24]. It was originally written in FORTRAN and was only capable to simulate gaseous detectors. Garfield was updated and ported to C++ at the end of the nineties and the possibility to simulate semiconductor detectors was added. This gave rise to the birth of Garfield++, a complete simulation tool for modeling of primary ionizations up to signal processing. Different algorithms are incorporated and a large flexibility is built-in to adjust the algorithms and the simulation environment. It is necessary to understand the basic principles behind the simulations, which we will describe in this section. A complete review can be found on the website, the user manual [25] and the source code.

An overview of the Garfield++ class structure is given in Fig. 4.5. The program and classes rely heavily on the ROOT software package, a simulation and analysis tool developed at CERN. In a first step to simulate a gas detector, the geometry must be defined. For simple geometries such as parallel plate detectors, it is possible to draw or define the detector with the use of ROOT classes. More complex geometries such as GEM detectors must be, together with the electrostatics, loaded from the ANSYS output files. The FEM elements are parsed such that the GEM unit cell is loaded in Garfield++. Afterwards, an active medium or gas

volume must be assigned which can be characterized by its permittivity ($\epsilon_r = 1$ for the gas volume). Only the active medium is used for the simulation and the other volumes (the metal and kapton layers) are neglected because no transport models are available in solids (except for semiconductors). A gas mixture can then be assigned to the gas volume via the Magboltz class, which is a link between Garfield++ and the standalone Magboltz simulation tool (see 4.2.2). The component class combines both the geometry and gas medium classes into a single description of the detector including the electric field. For simple geometries the field can be calculated analytically whereas for GEM detectors the potential is loaded from the ANSYS output files and the field is calculated by $\mathbf{E} = -\nabla\psi(\mathbf{r})$. If necessary, multiple field solutions (e.g. \mathbf{E} and \mathbf{B}) can be added in separated Component objects, as the field equations are linear and the superposition principle is valid. Once the geometry and the fields are combined in a Component object, the Track (4.2.1) and charge transport (4.2.3) classes can be used to simulate the primary ionization and the transport of the primary electrons respectively. The connection between these classes and the Component class is achieved by the Sensor class. The Sensor class is the global class connecting all the different sub-classes and allows to calculate the induced signals and perform convolutions with transfer functions.

4.2.1 HEED

HEED is an abbreviation for High Energy Electrodynamics, a standalone simulation tool written by I. Smirnov (originally in Fortran, later in C++) [26]. This program simulates the primary ionization process in detail according to the Photo-Absorption Ionization model described in section 2.2.1. More specific, it is able to calculate the following interesting quantities:

- gas parameters such as the cluster density, W -value and the stopping power;
- location of ionization clusters and energy transfer per cluster;
- position of the primary and secondary electrons from δ -electrons.

A wide selection of incident particles is available such as muon, pions, electrons positrons, α -particles, etc. For photons, no clusters are calculated but rather the position of the primary electrons. It is not possible, however, to calculate the energy of the primary and secondary electrons because the detailed transport of δ -electrons is not yet implemented in HEED. Hence, energy of the primary and secondary electrons is set to zero.

HEED relies intensively on photo-absorption cross sectional data for the different particles and gas mixtures ranging over a wide energy interval. In the discussion and formulas of the PAI model, the cross section is assumed to be the total photo-absorption cross section for a given atom, averaged over the electrons present in the atom. To make the simulations more accurate, HEED uses individual electron cross sections depending on the electron shell, conducted from different experiments. As a consequence, it is assumed that the energy from the charged particle is completely absorbed by a single electron rather than the atom. The photo-electron is emitted with an energy equal to the energy transfer minus the binding energy of the electron. The excited atom will release a photon or an Auger electron.

The accuracy of HEED is discussed in the main paper [26] where the simulations are carefully compared to experimental results. For example, the cluster density is simulated and compared with experimental data for pions, protons and electrons over an energy equivalent to $\beta\gamma = 10^5$. The simulations are in agreement with experimental curves with high accuracy.

4.2.2 Magboltz

Magboltz is a standalone program written in Fortran by S. Biagi [27]. It allows to calculate the transport parameters such as the drift velocity, Townsend coefficient, diffusion coefficients

and the attachment coefficient in the presence of electric and magnetic fields. A Monte Carlo integrator is used to solve the Boltzmann transport equation in detail, by assuming a third order Legendre expansion of the probability density function $f(\mathbf{r}, \mathbf{p}, t)$. This allows to calculate the drift velocity within an accuracy of 1%. The Monte Carlo integrator consists of a test electron which is released in a hypothetical gas medium where the electric field is aligned with the z -axis. After each collision with the gas atoms, the state (position, energy and direction) of the electron is updated. The solution of the Boltzmann equation converges to an equilibrium value after typically 10^7 collisions. The transport parameters are then extracted from the behavior of the electron during the simulation.

When the Magboltz program is called, the gas composition, the electromagnetic field and the environmental parameters such as pressure and temperature must be defined. The Magboltz simulation tool calculates the different transport parameters within the given configuration. The calculations can be repeated over a range of electric fields, and the results are stored in a gas table. The gas table can later be used to use in Garfield simulations or to plot the transport parameters as a function of the electric field.

Also Magboltz relies on atomic data cross sections to handle the collision energy transfer. All the cross sections of the processes which could occur must be taken into account: ionization, excitation, rotational and vibrational cross sections. A large database of cross sections is available online and is updated regularly (see for example [28]). The Magboltz simulation results are shown to be very accurate for electric fields up to 10 kV/cm, according to the discussion in the main paper. For higher fields, the accuracy depends on the energy range of the available cross-sections. In general, it is accepted that Magboltz produces reasonable results because it is able to successfully simulate GEM detectors where high fields are present (see section 5.3).

4.2.3 Charge transport

For electrons, two mechanisms are available to calculate the transport. The first one, named Avalanche Microscopic, uses the Magboltz interface to track the electron on atomic level. This method is by far the most precise but is time consuming when a large amount of electrons must be tracked. The second method is a macroscopic Monte Carlo integration by stepping in time, using the equation $\Delta s = \mathbf{v}_d \Delta t$ for the drift and $\sigma = D\sqrt{\Delta s}$ for the standard deviation for the diffusion. The attachment and avalanche processes are also treated on macroscopic level. For ions, only the Monte Carlo technique is available. For more information, see the Garfield++ user manual.

4.3 Local simulation environment

From the previous discussion about the simulation tools it became clear that when large-scale simulations have to be performed, an local environment has to be set up in order to efficiently perform the simulations. It is necessary to have a flexible connection between the different simulation tools (ANSYS and Garfield++) and between different computers available to perform the calculations. At the beginning of this thesis, such a simulation environment is conceived and elaborated.

4.3.1 Computer power

The simulation of the processes with Garfield can be a very computer intensive task. Especially the calculation of the electron avalanche processes, electron drift and transport parameters are very time consuming and cannot be executed on a classical computer. Care

has been taken, where possible, to reduce the computation time based on physical valid assumptions. For example, in this paper we report only single GEM calculations from where results for double or triple GEMs can be deduced, if needed, by extrapolating methods. The computation time scales with a power law because the amount of electrons on average rises according to a power law and it is not practical to calculate double and triple GEMs for timing optimization purposes. However, the extrapolation has to be verified with a final simulation.

The calculations in this paper were performed on two supercomputers. The first one, the CERN computing grid, was mostly used for the general calculations. The Garfield C++ were submitted into a queue with the use of bash job scripts. Furthermore, the CERN grid has a command-line based ANSYS 15.0 program which was used to calculate the electrostatics. For visualizing the ANSYS geometries, ANSYS 14.5 available at Ghent University was used. The electron transport parameters for different gases were computed on the STEVIN Supercomputer Infrastructure at Ghent University, funded by Ghent University, the Flemish Supercomputer Center (VSC), the Hercules Foundation and the Flemish Government – department EWI. A set of 7 programs were calculating simultaneously the gas files for different types of gas mixtures. The transport parameters were extracted afterwards on a local computer.

4.3.2 ANSYS input file generator

The flexibility to simulate different GEM geometries and electrostatics is limited by the relative complex structure of the ANSYS input files. Indeed, by changing a single parameter (e.g. thickness), the whole ANSYS file has to be modified. Especially when adding more GEM layers, the input file becomes enormous complex (per GEM layer, about 150 lines must be added). Another difficulty is the internal ANSYS volume numbering system which becomes very complicated when adding more GEM layers. Therefore, a program was written in HTML/PHP which automatically generates an ANSYS input file, including code for the calculations weighting fields on the anode and the cathode. Because we are not interested in the position of the arrival electrons, the anode readout strips are converted into one readout plane.

A screenshot of this script, captured in a web browser, is shown in Fig. 6.1. The reason why this script is written in HTML/PHP is because it is easy to implement a graphical user interface from where the GEM settings can be inserted. The first setting allows to define the total GEM layers. The input fields for the transfer voltages, transfer thickness and GEM voltages automatically increases when more GEM layers are selected. In the next fields, the GEM foil characteristics can be defined where the default foil configuration is already loaded. The remaining fields are the drift, induction and transfer dimensions and electrostatics. Once the GEM configuration is inserted, the script generates the ANSYS input code and displays it on the screen. Moreover, three files are created:

- GEM.inp: ANSYS input file for the electric field calculations;
- geometry.txt: text file containing the geometrical information;
- volumes.txt: a list with all the volumes created by ANSYS.

The GEM.inp file can be directly imported in ANSYS and the electrostatics can be calculated. The second file, geometry.txt contains all the geometric properties and voltages in a human readable format. It is necessary to have the GEM dimensions in Garfield++ and therefore a function is written which loads the contents geometry.txt into C++ variables. The file volumes.txt consists of information about the ANSYS volume numbering system which can be useful for debugging purposes.

MultiGEM ANSYS configuration file generation

MultiGEM configuration:

Gem layers	<input type="text" value="2"/>	
Kapton thickness (K)	<input type="text" value="0.05"/>	mm
Metal thickness	<input type="text" value="0.005"/>	mm
Pitch (P)	<input type="text" value="0.14"/>	mm
Outer diameter cone (D)	<input type="text" value="0.07"/>	mm
Inner diameter cone (d)	<input type="text" value="0.05"/>	mm
Rim	<input type="text" value="0.08"/>	mm
Drift region voltage	<input type="text" value="450"/>	V
Drift region thickness	<input type="text" value="2"/>	mm
VGEM 1	<input type="text" value="350"/>	V
Transfer voltage 1	<input type="text" value="300"/>	V
Transfer thickness 1	<input type="text" value="1"/>	mm
VGEM 2	<input type="text" value="350"/>	V
Induction region voltage	<input type="text" value="400"/>	V
Induction region thickness	<input type="text" value="1"/>	mm
	<input type="button" value="Generate file"/>	

Output code

Figure 4.6: The ANSYS file generator, written in HTML/PHP.

4.4 Source code

The complete source code used in the entire project is published on GitHub, available at <https://github.com/jeyserma/GEMSimulations>. The structure of the code and the source code files are summarized in Appendix B.

Chapter 5

GEM simulations and measurements

Both theoretical definitions and formulas introduced in chapter 2 and the technical GEM details in chapter 3 are now discussed with the use of simulations and measurements. It is the aim to analyze the simulation results for the individual processes such as primary ionization, charge transport, charge amplification and signal creation. These results are necessary to understand the shape of the signal pulse, from which the time information can be extracted. We continue this discussion by reporting experimental results on energy calibration and gain performed on a CMS triple GEM prototype. This is useful in the last section where the simulation results are compared to experimental gain results.

5.1 Single GEM simulations

A single GEM detector is used to discuss the general simulation results rather than a triple GEM in order to reduce the computation time. The dimensions are listed in Table 5.1. A gas mixture of Ar-CO₂ is used with a composition of 75-25% at standard temperature and pressure (STP, i.e. $p = 1$ atm and $T = 293.15$ K). Muons with an energy of 100 GeV are perpendicularly incident on the detector at $\mathbf{r}_0 = (0, 0, 0)$, according to the coordinate system defined in section 4.1. The Penning transfer coefficient $f_p = 0.57$ is applied for the correction of the avalanche growth. In order to increase the statistics, the simulation has been repeated over 100 iterations. Although the transport of the ions is incorporated with the Monte Carlo stepping algorithm, we will not incorporate them in this discussion. As will be shown in section 5.1.4, the ion contribution of the induced signal is spread out over a long time interval and can be neglected.

Table 5.1: Single GEM dimensions and electrostatics used in this section.

Drift region thickness	2 mm	Inner hole diameter	55 μm
Induct region thickness	1 mm	Outer hole diameter	85 μm
Pitch	140 μm	Rim	85 μm
Kapton thickness	50 μm	Metal thickness	5 μm
V_{drift}	270 V	E_{drift}	1.35 kV/cm
V_{induct}	400 V	E_{induct}	4 kV/cm
V_{GEM}	460 V	E_{GEM}	92 kV/cm

5.1.1 Gas properties

In the following discussion the gas properties are frequently used to explain the results of the simulation. For ease, the simulated gas properties are listed in Table 5.2. The ionization parameters were calculated with HEED for 100 GeV muons whereas the transport parameters

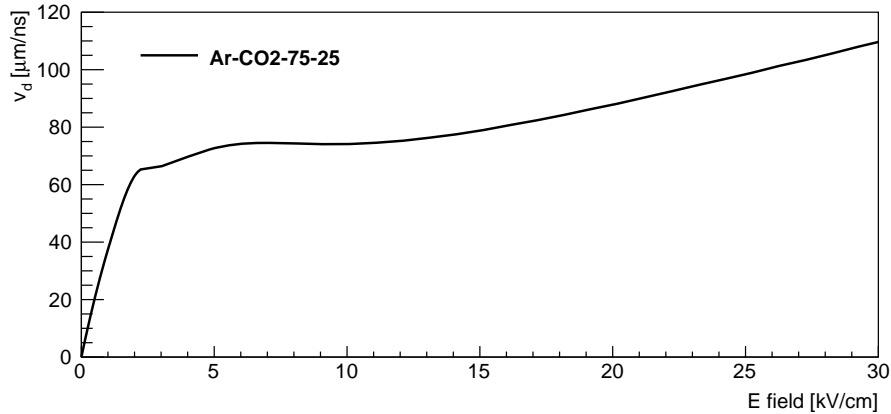


Figure 5.1: Simulated electron drift velocity composed with Magboltz for Ar-CO₂ (75-25) as a function of the electric field.

were calculated with Magboltz for electric fields up to 100 kV/cm. A plot of the drift velocity is shown in Fig. 5.1 for the electric fields of interest, from which the drift velocity in the drift and induction region can be extracted. Furthermore, the Townsend coefficient α at the GEM hole electric field was calculated and given in the table. The maximum attachment coefficient was calculated to be around 6.5 cm^{-1} at $E = 18 \text{ kV/cm}$ and can be neglected w.r.t. α in the high electric field region (i.e. GEM holes).

Table 5.2: Calculated ionization and transport parameters for Ar-CO₂ (75-25).

Ionization parameters		Transport parameters	
λ^{-1}	37.78 cm^{-1}	$v_d(E = E_{\text{drift}})$	$45 \text{ } \mu\text{m/ns}$
dE/dx	3.05 keV/cm	$v_d(E = E_{\text{induct}})$	$70 \text{ } \mu\text{m/ns}$
W -value	27.76 eV	$\alpha(E = E_{\text{GEM}})$	1850 cm^{-1}
I_{min}	13.79 eV	η_{max}	6.5 cm^{-1}

5.1.2 Primary ionization

HEED was used to calculate the primary ionization encounters, cluster positions, cluster size distributions, etc. Because delta electron transport is not fully integrated in the algorithm (see section 4.2.1), the primary electrons have zero energy. It is possible to assign a value for the primary electron energy according to a certain distribution, provided the energy is lower than the lowest ionization potential I_{min} of the gas (otherwise new secondary ionizations could occur). However, such approach was not incorporated in the simulations because the initial electron energy (typically a few eV) is negligible as the mean electron energy is only governed by the electric field.

The results of the primary ionization are shown in Fig. 5.2. A first quantity to discuss is the amount of clusters created, described by a Poisson distribution with a mean $\mu = L/\lambda$. For this configuration $L = d_{\text{drift}} = 0.2 \text{ cm}$ and $\lambda^{-1} = 37.78 \text{ cm}^{-1}$, yielding a mean of 7.556 clusters. This is in good agreement with the simulated value $\mu = 7.66$ (see Fig. 5.2(a)). A slightly higher mean value equal to 8.521 is obtained when the distribution is fitted to a Poisson distribution. From the distribution of the z -coordinate of the clusters, plotted in Fig. 5.2(b), it is clear that the clusters are nearly uniform spread over the drift region. Because most of the primary electrons are liberated in the vicinity of the cluster position (except δ -rays), the primary electrons are nearly uniform distributed over the drift region. In Fig.

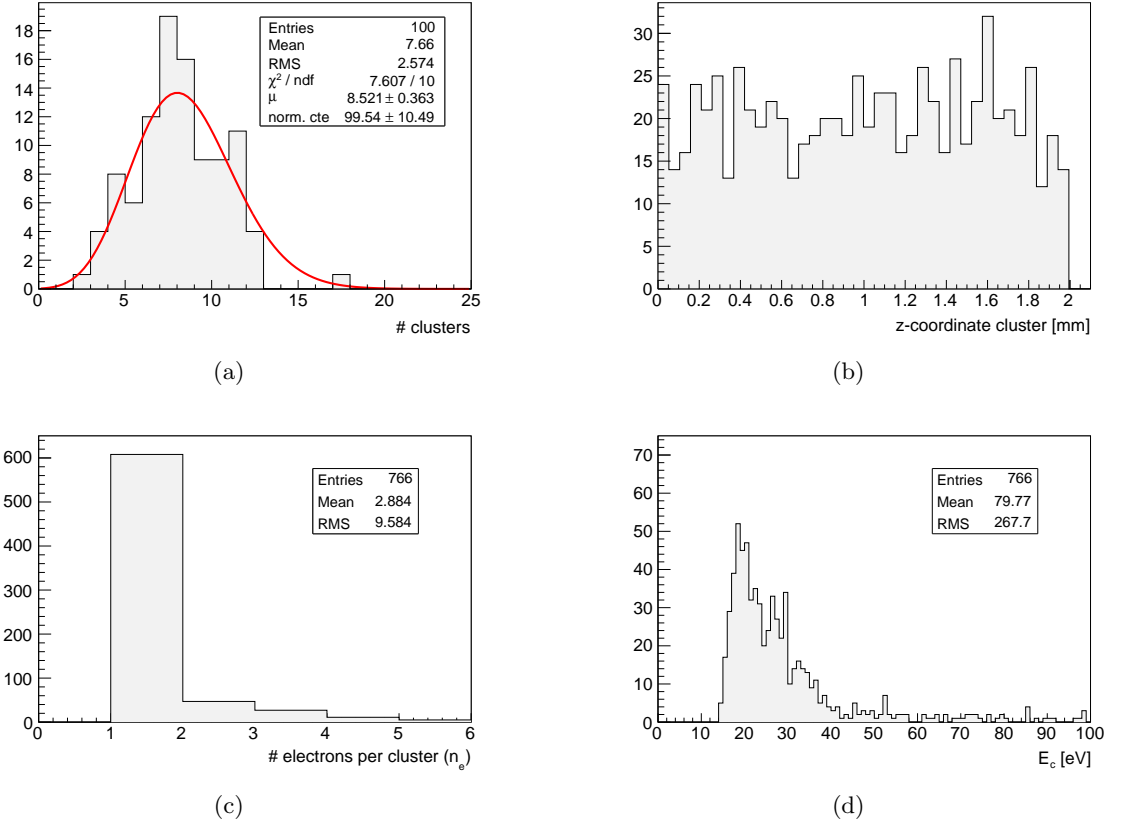


Figure 5.2: Primary ionization simulation results: total cluster distribution (a), cluster-size distribution (b), z-coordinate of the clusters (c) and energy transfer E_c to the primary electrons per cluster (d).

5.2(c) the amount of electrons per cluster n_e , or the cluster-size distribution is plotted up to $n_e = 6$. In most of the clusters one or two electrons are liberated but there is a probability to liberate more than two electrons yielding a mean of $\langle n_e \rangle = 2.884$ electrons. Indeed, due to δ -rays (having energies in the order of keV) the amount of liberated electrons can be in the order of 10–200 electrons. The mean number of electrons depends on the gas mixture (and the incident particle) and is preferably as high as possible to have many primary electrons per cluster to maximize the signal.

In general, the amount of liberated electrons per cluster depends on the energy transfer E_c per cluster from the charged particle to the gas atoms, shown in Fig. 5.2(d). The distribution is terminated at $E_c = 100$ eV, though higher values due to δ -electrons are present but not shown in the histogram. The cut-off at low energies is equal to the minimal ionization potential $I_{\min} = 13.79$ eV because lower energy transfers will not induce (primary) ionizations. The mean value $\langle E_c \rangle \approx 79.77$ is related to the W -value as follows. Because $\langle E_c \rangle$ is the mean energy transfer to one cluster, the mean energy transfer to a single electron is given by $\langle E_c \rangle / \langle n_e \rangle = 27.66 \approx W$. The energy of the primary electrons is then equal to the individual energy transfer¹ minus the binding energy of the liberated electron. It is possible that a primary electron has an energy above I_{\min} which can cause further ionizations on its path in the drift region. In such a case, the initial energy of the electron is distributed over a few secondary electrons until the energy of the secondary produced electrons is lower than I_{\min} (the transport of δ -electrons is analogue but more secondary electrons are produced). The

¹HEED is able to calculate the per-electron energy transfer, which was not originally implemented in the PAI model.

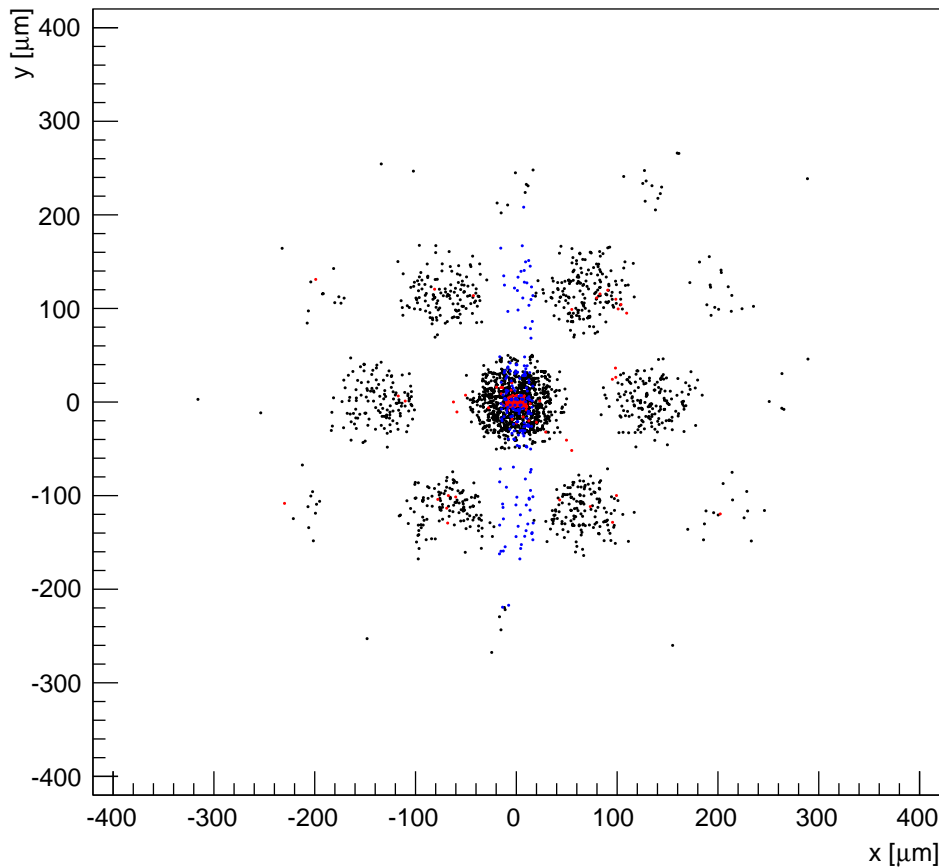


Figure 5.3: (x, y) -distribution of the ionization processes without the primary ionization. The red dots indicates ionization in the drift region, the black dots in the GEM holes and the blue dots in the induction region. Note that the data of the histogram contains 100 initial events.

drift field is assumed to be too weak in order to increase the electron energy above I_{\min} and no further ionizations will occur. This result is shown in Fig. 5.3, where the (x, y) coordinates of the ionization positions are plotted in a two-dimensional histogram for each region (drift, holes, induction). Ionizations in the drift region are colored in red.

The mean amount of electrons liberated in one event is equal to $\langle n_e \rangle \cdot L/\lambda = 2.675 \cdot 7.84 = 22.61$, i.e. the average amount of electrons per cluster times the average amount of clusters in the event. This number can easily be calculated with the stopping power and the W -value, according to Eq. 2.4. From the stopping power, the average energy deposit of one muon in the drift region is equal to $Q = dE/dx \cdot d_{\text{drift}} = 610 \text{ eV}$, yielding an average of $\langle n \rangle = Q/W = 21.97$ electrons. This is in close agreement with the simulated value.

5.1.3 Charge amplification and effective gain

The primary and secondary electrons drift to the GEM holes following the drift lines. As already discussed in the previous section, energetic electrons can induce a little amount of ionization on their path, as shown in Fig. 5.3 with the dots. Once arrived in the holes, the strong electric field will induce an avalanche, shown as black dots on the figure. In this ideal scenario where the muons are perpendicularly incident at the origin, the transverse (x, y) -distribution is nearly symmetric around the central hole. The avalanche-size distribution is shown in Fig. 5.4, containing a total of 2167 avalanches. This number corresponds to the

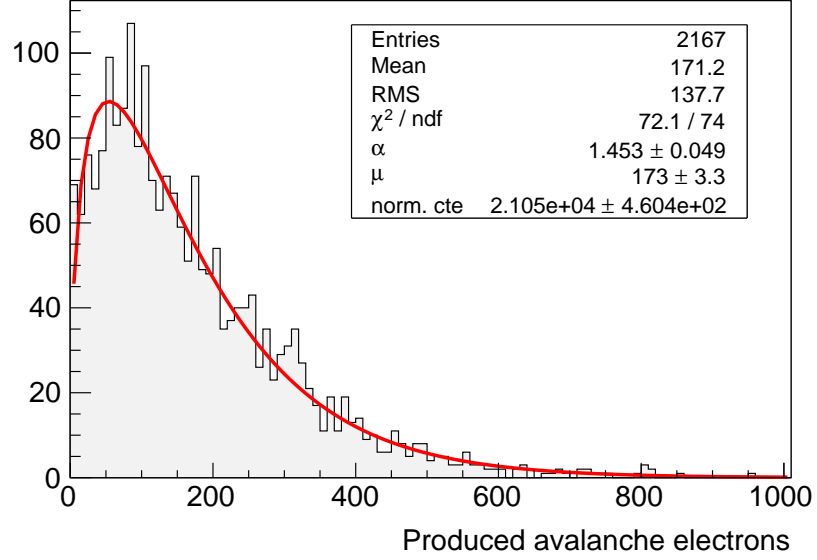


Figure 5.4: Avalanche-size distribution induced by primary and secondary electrons. The distribution is fitted to a Polya distribution.

mean number of primary and secondary electrons, being 22, multiplied by 100 events. The distribution reflects the variation of the avalanche or the gain variation and is described with a Polya distribution with mean $\mu = 167.6$ and RMS $\sigma = 136.5$. After fitting to a Polya distribution (see Eq. 2.31), the mean is equal to $\mu = 166.5$ and $\alpha = 1.482$, yielding an RMS of $\sigma = \mu/\sqrt{\alpha} = 136.77$, in good agreement with the simulated values. The gain fluctuations are indeed well described with a Polya distribution, despite the fact that the distribution was originally derived for wire chambers.

The drift of the electrons in each avalanche is governed by the electric field in the hole and induction region. As discussed in section 3.2.2, the field lines do not always terminate on the anode but also on the kapton and GEM metal electrodes. As a result, the z -coordinate of the arrival electrons is spread over the anode and the metal-kapton-layer, as shown in Fig. 5.5(a). In this histogram, the arrival z -coordinate of the electrons is plotted and one can see that only a minority will reach the anode at $z = 0.306$ cm. A complete list of the arrival electrons, including attachment in the induction region, is given by:

- anode electrons (signal): 40.484%,
- kapton electrons: 3.8%,
- attachment in drift region: 2.588%,
- top GEM electrode electrons: 0.001%,
- bottom GEM electrode electrons: 53.065%.

Only 40.484% of the produced avalanche electrons will drift towards the anode and induce a signal. Indeed, the other electrons are captured very fast on the GEM electrodes or on the kapton, inducing a negligible signal. As a result, the total gain will be lower and the effective gain can be calculated as (see Eq. 3.6):

$$G_{\text{eff}} = \xi G = 0.40484 \cdot 171.2 = 69.31. \quad (5.1)$$

In Fig. 5.5(b), the initial z -coordinate of the avalanche electrons is plotted in GEM holes. The hole starts at $z = 2000 \mu\text{m}$ and ends at $z = 2060 \mu\text{m}$, and it follows that most of the electrons are produced in the lower region of the GEM hole. This can be seen from

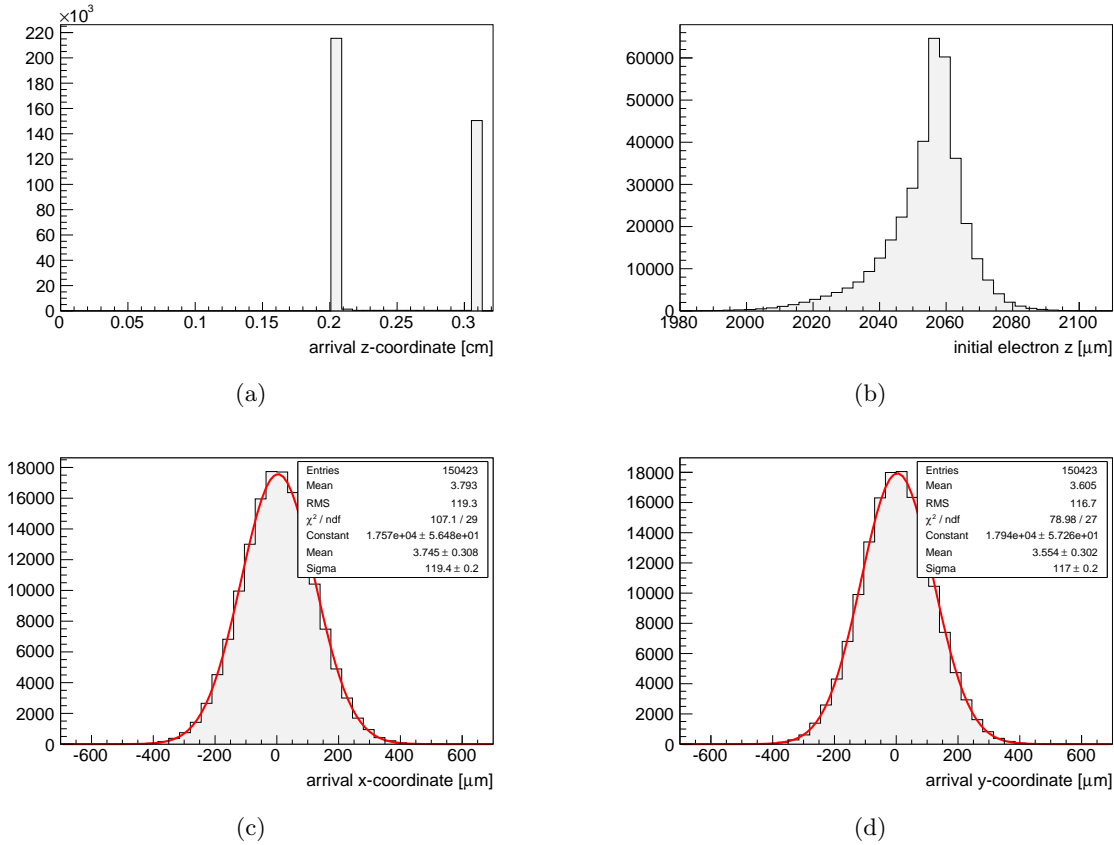


Figure 5.5: z -coordinate of the arrival electrons after the avalanche (a), close-up of the initial electrons produced in the GEM holes (b) and (x, y) spread of the electrons arriving at the anode readout plane (c and d).

the Townsend equation (Eq. 2.28), which can be solved if we assume a constant Townsend coefficient α :

$$N(z) = N_0 \exp\left(\int_{s=z_0}^{s=z} \alpha ds\right) = N'_0 \exp(\alpha z), \quad (5.2)$$

with N_0 the initial amount of electrons and N'_0 the amount of electrons at $z = 2000 \mu\text{m}$. The exponential behavior is clearly visible in the interval $2000 \leq z \leq 2060 \mu\text{m}$. For $z > 2060 \mu\text{m}$, the magnitude of the electric field is lower, resulting in a decrease of Townsend coefficient and the amount of produced electrons decrease. At $z = 2095 \mu\text{m}$, the Townsend coefficient is zero and no additional electrons are produced.

One last interesting result to investigate is the transverse spread of the arrival electrons on the anode. For both x and y directions, the distributions are shown in Fig. 5.2(c) and 5.2(d) respectively. Due to the symmetry, the mean of both distributions is almost equal to zero. The RMS of the distributions is related to the position resolution because readout strips with transverse dimensions equal to the RMS value is the upper limit to determine the position of the incident muon. An RMS of $120.3 \mu\text{m}$ is obtained and proves the excellent position resolutions that can be achieved with GEM detectors. It must be stressed that these results are obtained with perpendicularly incident muons yielding an absolute minimum of the RMS value. Non-perpendicular muons will spread out the avalanche in more holes, resulting in a higher RMS value.

5.1.4 Signal creation

According to the Shockley-Ramo theorem, a signal will be induced on the anode during the time the swarm of electrons created in the avalanche drift from the GEM hole to the anode. The induced signal from the drift of the primary and secondary electrons towards the GEM holes is negligible because the charge is masked by the top GEM foil. A single electron drifting towards an electrode will induce a constant current in time, provided the electric field and the drift velocity is constant (see Eq. 2.38). This is valid in the induction region, where the electric field and thus the drift velocity can be regarded as constant (see Fig. 3.3(b)). To investigate the signal, we start by simulating the induced current from a single electron in the drift region with initial coordinates $\mathbf{r}_0 = (0, 0, d_{\text{drift}}/2)$, zero energy and a random velocity direction. This electron can be regarded as a primary electron, drifting towards the GEM holes and producing n_e electrons in the avalanche. The induced signal is shown in Fig. 5.6(a), where the collected charge in bins of 0.5 ns is plotted in an histogram.

The induced current is negative because the motion of the electrons is opposite to the electric field, yielding $\mathbf{E} \cdot \mathbf{v} < 0$ and thus $I(t) < 0$. The shape of the pulse can be regarded as a block pulse, which is in agreement with the Shockley-Ramo theorem where a constant current is expected due to the drift of the electrons in the induction region. The timing characteristics of this pulse can be calculated from the drift velocities of the gas. Time zero ($t_0 = 0$) is defined as the time when the electron is released at its initial position. The signal only appears at $t_1 = 19$ ns, which is approximately equal to the time needed for the electron to drift towards the GEM hole:

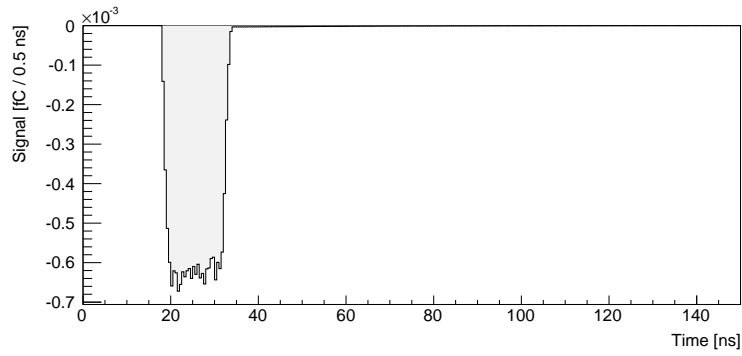
$$\Delta t_1 = t_1 - t_0 = \frac{d_{\text{drift}}/2}{v_{d,\text{drift}}} = \frac{0.1 \text{ cm}}{45 \mu\text{m} \cdot \text{ns}^{-1}} = 22.22 \text{ ns}. \quad (5.3)$$

This calculated value is a few ns higher than the actual signal time t_1 because the electric field increases when approaching the GEM hole. The drift velocity increases when the field increase (see Fig. 5.1), resulting in a lower drift time. The time needed to develop the avalanche and the drift inside the GEM hole can be neglected in first order as the drift velocity is very high and the GEM foil is very thin. From the figure, the signal stops at $t_2 = 34$ ns, yielding a total width of 15 ns. The duration of the induced signal is equal to the time needed for the avalanche electrons to drift to the anode and can be calculated as:

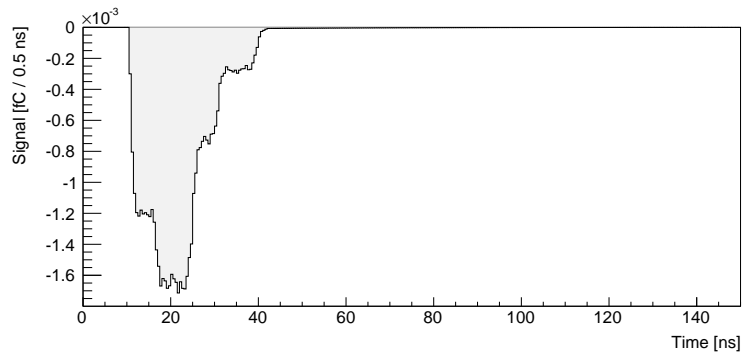
$$\Delta t_2 = t_2 - t_1 = \frac{d_{\text{induct}}}{v_{d,\text{induct}}} = \frac{0.1 \text{ cm}}{70 \mu\text{m} \cdot \text{ns}^{-1}} = 14.29 \text{ ns}, \quad (5.4)$$

which is in good agreement with the simulated value. The height of the pulse is proportional to the collective charge created in the avalanche and to the product $\mathbf{E} \cdot \mathbf{v}$. The electrons collected on the GEM foil do not induce a noticeable signal on the anode because they are collected very fast. From this discussion we can conclude that the induced signal of a single primary or secondary electron is block shaped, with a time offset determined by the drift velocity in the drift region and its initial position, a width determined by the induction region drift velocity and a height proportional to the avalanche size and the induction field.

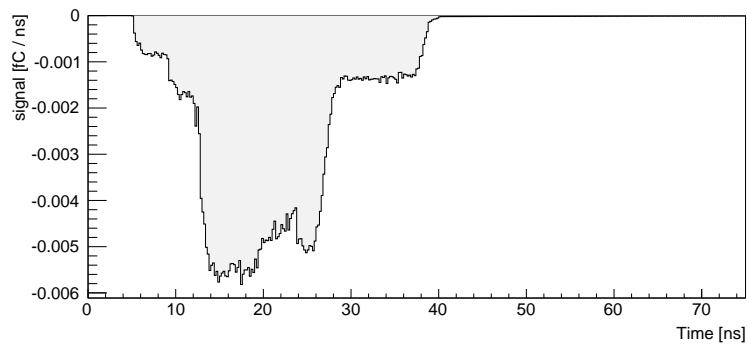
In a more realistic scenario, multiple primary and secondary electrons almost instantaneously created in the drift region and drift towards the GEM holes, each triggering an avalanche and inducing a current on the readout electrode. The total induced charge is a superposition in time of the individual induced charges. The individual block pulses will in general overlap and a random signal is induced depending on the drift velocities and the initial primary electron coordinates. For example, in Fig. 5.6(b), the induced signal is plotted when primary electrons at $(0, 0, 0.3 \cdot d_{\text{drift}})$, $(0, 0, 0.5 \cdot d_{\text{drift}})$ and $(0, 0, 0.7 \cdot d_{\text{drift}})$ are simultaneously released. Three pulses having equal widths overlap symmetrically and four plateaus (four different overlaps in total) are visible, as expected. In Fig. 5.6(c), a pulse resulting



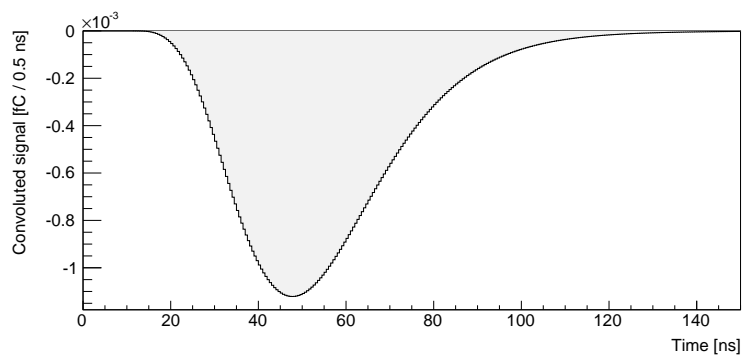
(a)



(b)



(c)



(d)

Figure 5.6: Induced signal from a single electron in the drift region (a), induced signal from three electrons in the drift region (b), random pulse from an incident muon (c) and the convoluted signal with the VFAT3 transfer function (d).

from a perpendicularly incident muon is shown. Multiple primary electrons distributed over the drift region each contributes to this signal with different time offsets and gains, resulting in a random pulse. To characterize such a random pulse, the following quantities can be extracted:

- the time offset Δt_1 ,
- the width of the pulse Δt_2 ,
- the mean and
- the RMS of the pulse.

The ions also induce a current on the anode from the time they are produced in the avalanche. However, because the ion drift velocity is several orders lower than the electron drift velocity, the total width of the ion induced current is in the order of μm . Due to charge conservation, the areas under the electron pulse and the ion pulse must be equal to each other and the amplitude of the ion signal is several order lower than the electron signal and can be neglected.

For completeness, the convoluted signal of 5.6(b) is shown in Fig. 5.6(d). The transfer function applied is the VFAT3 transfer function², given by [29]:

$$H(s) = 0.46G \left(\frac{s}{s_0} \right)^3 \exp(-3s/s_0), \quad (5.5)$$

with $G \approx 2$ the gain of the last differential stage and $s_0 = 27.5$ if the peaking time is 25 ns. The shape is characteristic for detector electronics as all of them use the same building blocks such as amplifiers and integrators. Depending on the desired measurement, the electronics can be modified to adjust the signal pulse such as the gain, peak and rise time.

5.2 Gain measurements and energy calibration

In this section, the gain of a CMS triple GEM prototype is measured together with the energy calibration using a photon source. This is useful to understand the interactions of photons in the drift region and how GEMs are practically operating. The same experimental setup is used in the next section where the simulation results are compared to experimental gain measurements.

5.2.1 Experimental setup

The triple GEM detector is a small prototype measuring an area of $10 \times 10 \text{ cm}^2$ and having a two-dimensional grid of readout strips at the readout plane. Because no position measurements were performed, the strips were electrically connected to each other acting as a single readout plane connected to the electronics. A static gas mixture of Ar-CO₂ was used with a composition of 70-30%. Instead of the traditional double-mask production process for the GEM foils, here a single masked GEM foil was used which was manufactured at CERN. Care has been taken during the production process to obtain approximately the bi-conical hole shape with its standard dimensions. The separation of the gaps is 3:1:2:1 mm, beginning with a drift region of 3 mm. The electric fields over the gaps and GEM foils were established by using a voltage divider with resistor values of respectively 1.25, 0.5625, 0.4375, 0.55, 0.872, 0.525 and 0.625 M Ω . A High Voltage filter of 0.3 M Ω was installed at the beginning of the voltage divider, before the connection to the drift plane. This results in a total resistance of 5.112 M Ω . The total voltage across the GEM was controlled by a CAEN High Voltage power supply, ranging from 3 kV up to 3.5 kV. Between the branches of the voltage divider,

²The VFAT3 chip is proposed as the readout chip for the CMS triple GEM detector but is still under development.

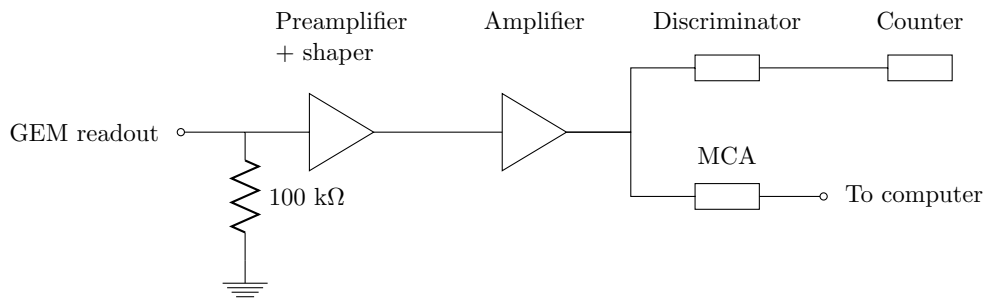


Figure 5.7: Schematic overview of the electronics used to measure the spectrum and the operating plateau. To measure the gain, a picoamperemeter was directly connected to the GEM anode.

a resistor of $10\text{ M}\Omega$ was placed in order to correctly drain the collected charge on the GEM metal foils. The entire setup was housed in a box covered with soft copper plates for reducing external electronic noise.

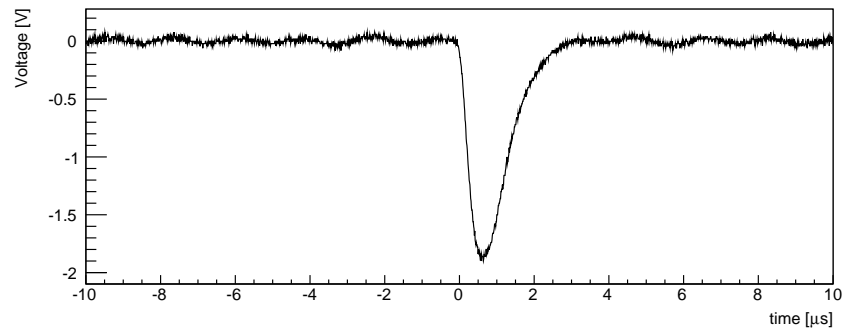
The source used in the experiment was a Fe-55 source, emitting X-rays with a main energy peak at 5.9 keV . The strength was approximately 2.5 MBq which is equivalent to 2.5 decays each ns. The photons were emitted isotropically from the source and only a small fraction of the total solid angle reaches the detector, yielding a radiated area in the order of 0.5 cm^2 . Hence, the photon rate incident on the detector is much lower than 2.5 per ns.

The electronic setup for measuring the energy spectrum and the operating plateau is shown in Fig. 5.7. The first stage is the preamplifier and shaper. This device amplifies the very weak current from the GEM and shapes the signal. It was located directly behind the GEM readout inside the copper box. Because the preamplifier contains a capacitor, the charge must be drained in order to avoid saturation when the capacitor is fully charged. Hence, a resistor of $100\text{ k}\Omega$ is placed between the GEM readout and the preamplifier. A second amplifier is located after the preamplifier. The pulse shape is shown in Fig. 5.8(a), recorded with an oscilloscope, connected directly after the second amplifier. Both amplifiers were adjusted to optimize the signal-to-noise ratio. The noise increases with higher voltages and the signal-to-noise ratio must be optimized with the applied voltage of 3.5 kV . As can be seen from the figure, the noise (superimposed on the signal) is minimized and the signal is clearly visible. After the amplifier, different electronics are used depending on the type of measurement. For measuring the operation plateau, a discriminator and counter was used. For measuring the spectrum, a multichannel analyzer (MCA) was used which is connected to the computer whereas for measuring the gain a picoamperemeter was used.

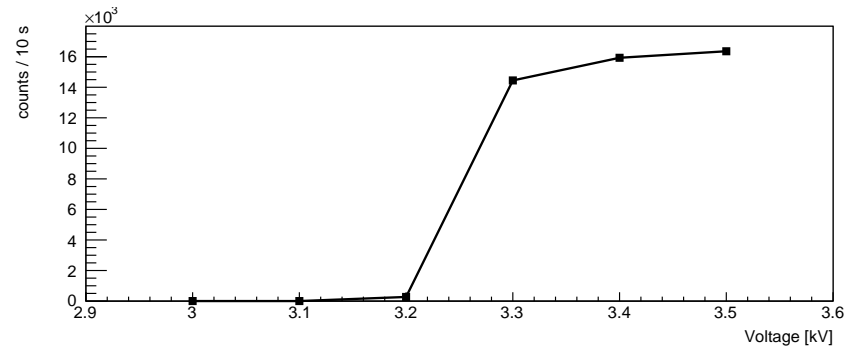
5.2.2 Operating plateau and interaction rate

In order to calculate the gain of the detector, the photon interaction rate R with the gas medium must be known. Indeed, the detector is not designed for single photon detection and not every incident photon will interact with the gas medium. From simulations it follows that for a 3 mm drift region thickness and a Ar-CO_2 (70–30) gas mixture, only 20% of the photons is converted in the drift region or 3 mm . The photon energy is almost completely transferred to the gas atoms to generate primary electrons and ions (see section 5.2.4). In order to measure the interaction rate, it is possible to count the amount of events on the readout electrode, provided each photon interaction yields a detectable signal above the threshold. The amplitude of the signal depends on the voltage applied over the GEM foils and must be sufficient high in order to detect every photon interaction.

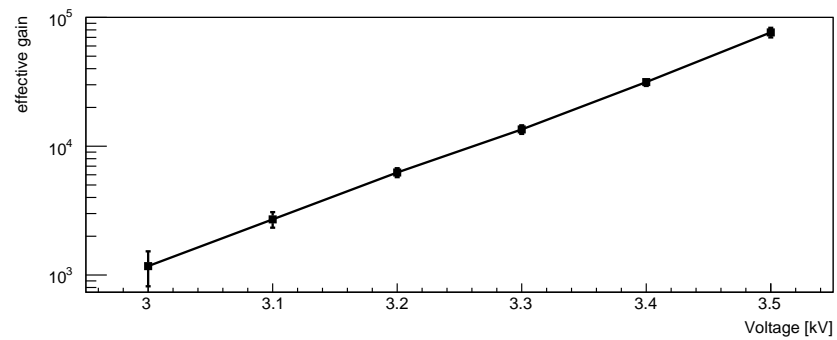
The amount of events was counted with the counter module as described in the previous section, within a time interval of 10 s . The measurement was repeated for each voltage



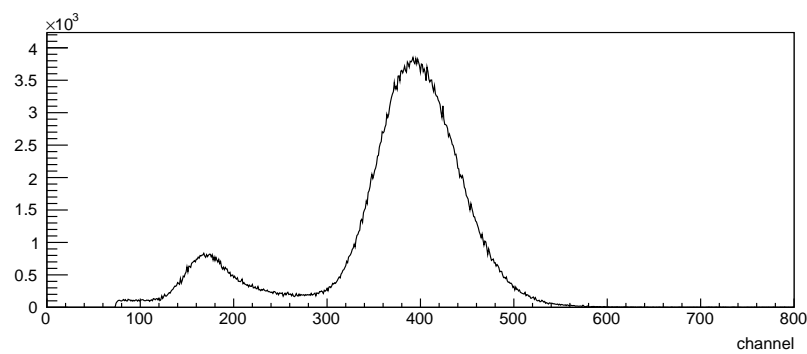
(a)



(b)



(c)



(d)

Figure 5.8: Pulse shape of the readout electronics measured with an oscilloscope (a), counted photons interactions in a 10 s time window as a function of the applied voltage (b), the effective gain as a function of the applied voltage (c) and the Fe-55 spectrum measured by the GEM (d).

($3 \leq V \leq 3.5$ kV) applied on the detector and the result is plotted in Fig. 5.8(b). For low voltages, the signal is too weak and no counts are observed. When the voltage increases, the counts are increased because some of the photon interactions generates a detectable signal. At high voltages, the counts saturate to a value of 16144 events per 10 ns, where the last two points were averaged. This plateau region corresponds to a photon interaction rate of $R = 1614.4$ Hz.

5.2.3 Effective gain

To measure the gain of the detector, the total charge collected on the anode must be measured. A picoammeter was directly connected to the readout electrode measuring the current in a certain time range. The device is connected to a computer from where the current values can be processed. As a function of the applied voltage, the current I_1 was measured for 30 s. Because the noise is not negligible at such high voltages, the signal was corrected in order to obtain the net collected charge on the anode. This was done by subtracting the average noise level, obtained by measuring the current without source (dark current) in a time interval of 30 s.

Because only the collected charge on the anode was measured, it was only possible to obtain the effective gain G_{eff} . The gain is defined as the total charge w.r.t. one primary electron and the following formula was used to calculate G_{eff} as a function of the net current I (measured in Amperes):

$$G_{\text{eff}} = \frac{I\Delta t}{R\Delta t \cdot n_i \cdot e} = \frac{I}{R \cdot n_i \cdot e}, \quad (5.6)$$

with:

$I\Delta t$ the measured charge on the anode in the time window Δt ,
 $R\Delta t$ the amount of photon interactions in the time window Δt ,
 n_i the amount of electrons released per photon interaction and
 e the unit charge.

n_i can be calculated with the W -value and the assumption that the total photon energy is deposited in the gas medium. This approximation is not completely valid as not every photon deposits its full energy in the drift region (see next section). Notwithstanding the total primary electrons can be calculated as:

$$n_i = \frac{E_\gamma}{W} = \frac{5.9 \text{ keV}}{27.77 \text{ eV/primary}} = 212.48. \quad (5.7)$$

Inserting this value and the previous obtained rate $R = 1614.4$ Hz in Eq. 5.6, the formula can be simplified to $G_{\text{eff}} = 18.197 \cdot I$, when I is expressed in pA.

For every high voltage step between 3 and 3.5 kV, the current and dark current was measured and the gain is extracted. The result is plotted in Fig. 5.8(c) on a log-scale. Expected gains for triple GEMs up to 10^5 are obtained and a linear curve as a function of the voltage is visible. This is a result from the exponential solution of the Townsend equation and the fact that at high fields α is proportional to the electric field.

5.2.4 Energy resolution and calibration

With the multichannel analyzer, the spectrum of the source can be measured and the energy resolution can be extracted. Because this device measures the spectrum in units of ADC counts or channel number, the conversion to the energy scale needs to be done. This calibration process is rather easy because the energy of the gamma source is known and the spectrum can easily be correlated with the energy scale.

The Fe-55 spectrum was directly measured with a multichannel analyzer connected to the computer via USB. This device records the signal pulse from the readout plane within a short time interval and converts the pulse amplitude to a digital number. The memory location or channel corresponding to this digital number is increased by one unit. After the measurement the values of memory locations are read by the computer and the contents are plotted in an histogram as a function of the channel number. Because the time between two received pulses is around $R^{-1} = 1616.4^{-1} = 618.7 \mu\text{s}$, a lot of noise is recorded in the intermediate intervals and will make a large contribution to the histogram for low channel numbers. Hence, a channel threshold value of 80 is applied to remove this noise. Furthermore, an internal gain of the pulse amplitude is set to 3 to reduce additional noise.

The pulse-height spectrum for Fe-55 is shown in Fig. 5.8(d). It starts at the threshold value of 80 and two peaks are visible. The main peak at channel 400 corresponds to the full photon peak of 5.9 keV where the full photon energy is converted into primary electrons. The second peak at channel 170 is the so called escape peak. As explained in chapter 2, the ionized atoms can relax by emitting a fluorescence photon which can escape from the gas volume. This photon energy is lost and not available to create primary electrons, resulting in a lower pulse height. In this case, the 5.9 keV photons can easily ionize the K-shell of Ar (with a binding energy of 3.2 keV) emitting a photon of $5.9 - 3.2 = 2.7$ keV. Hence, the escape peak corresponds to a deposited energy of 3.2 keV.

The main peak at channel 400 corresponds to an energy deposit of 5.9 keV and one expect a Dirac-peak focused at one channel, corresponding to a constant pulse height. Due to gain fluctuations and other processes such as attachment, the pulse height will fluctuate around a central value. These fluctuations reflects in an uncertainty of the energy measurement and is described with the energy resolution of the detector. The energy resolution is defined as the FWHM divided by the main peak position. From the spectrum in Fig. 5.8(d), an energy resolution of 25% is achieved.

5.3 Comparison gain measurements with simulation

Up to now we only discussed the behavior of GEMs with the use of simulations and simple calculations were able to verify these results. However, the level of the simulation with Garfield++ is very high and one might wonder if the combination of the different simulated processes (ANSYS, HEED and Garfield++) are in agreement with experimental results. Gain measurements provide appropriate data to test the simulations because all the individual processes are involved, except the timing characteristics such as the simulation of the induced current.

The experimental results are extracted from the paper *Energy Resolution of a Single GEM Detector*, published in the Journal of the Korean Physical society by S.Y. Ha et al [30]. In this paper, the gain and energy resolution of a single GEM is measured with an experimental setup equivalent as described in the previous section. The GEM foil dimensions and structure are described in detail making it possible to simulate an exact copy of the GEM used in the measurements. Two simulations have been performed: calculating the effective gain as a function of the GEM and drift voltage. The first simulation uses dimensions given in Table 5.1. The gain measurements as a function of the drift voltage is performed with a fixed GEM voltage of 470 V, the induction region at 400 V and a drift region thickness of 3 mm.

In the simulations, the photons are not simulated but the primary electrons are directly generated in the drift region. The initial position is chosen to be random in the unit cell provided the electron is in the drift region ($z < d_{\text{drift}}$). This approximation has been validated by simulating a high amount of incident photons and the distribution of the z -coordinate of the primary electrons tend to be approximately uniform. The uniformity in the transverse plane

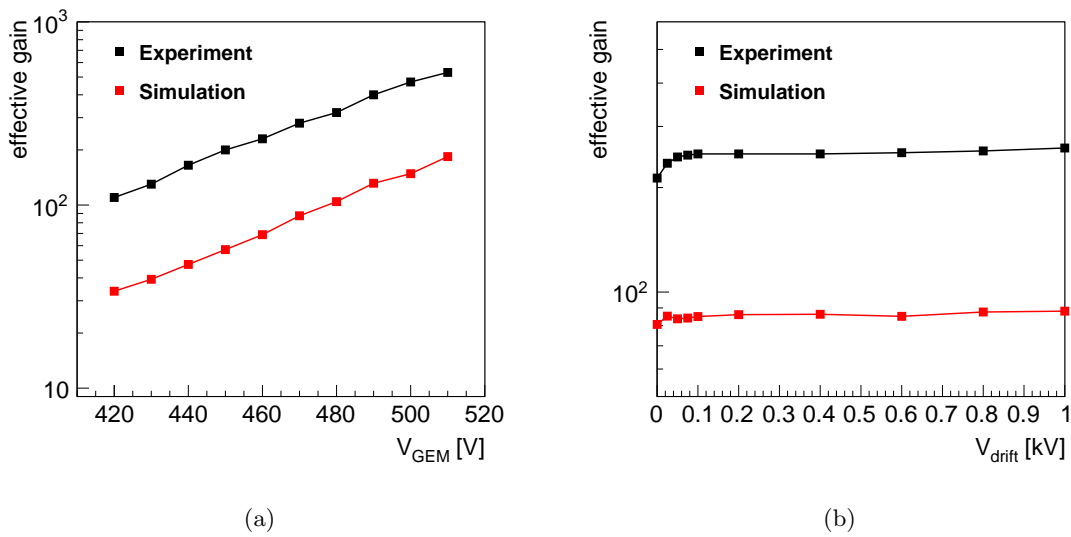


Figure 5.9: Comparison of the gain with simulated results: gain as a function of the GEM voltage (a) and as a function of the drift voltage (b).

(x, y) depends on the collimation of photon source but is in general true. The simulations were repeated over 1000 iterations to increase the statistics.

Both simulation results are shown in Fig. 5.9 where the measured data are also shown for comparison. As a function of the GEM voltage, shown in Fig. 5.9(a), the gain is again approximately exponential due to the exponential solution of the Townsend equation. The simulated gain has the same behavior as the measured gain, though is reduced with an average factor of 3.22. The same behavior is obtained when the gain is measured as a function of the drift voltage (see 5.9(b)). The gain is constant, as expected, because it is only governed by the GEM voltage. However, when the drift voltage is too low, the primary electrons do not reach the GEM hole due to recombination and the gain drops (see figure). The simulated gain is on average reduced with a factor of 2.88.

The reason why the gain is reduced with a factor of 3 is due to different approximations in the simulation. Although it is not the purpose to investigate the accuracy of the simulations, we can cite some shortcomings. For example, it is possible that too many electrons are captured by the lower GEM metal electrode due to inaccuracies when calculating the potential near the GEM holes. Another possibility is the cluster-size distribution which can be too low yielding a lower gain. However, the penning transfer rate is assumed to be correctly matched with the Ar-CO₂ gas mixture and it is believed no significant errors are addressed to this process.

Chapter 6

Time resolution

In the previous chapter, the shape of the raw signal induced on the anode was discussed on the basis of the GEM and gas properties. The pulse is processed by the electronics and information of the time coordinate when a charged particle passed through the detector can be extracted. Because of the stochastic processes inside the detector, the pulse and the time coordinate measurement are subjected to uncertainties and it is necessary to understand the cause of these uncertainties in order to reduce them. Furthermore, the measurement of the time coordinate strongly depends on the electronics used and therefore it is difficult to define an intrinsic time resolution, independent of the electronics. It is possible, however, to gain some qualitative knowledge to reduce the uncertainties based on methods for time coordinate measurements. From this discussion, a method is developed to search for gas mixtures which reduces the uncertainty on time measurement. This method is applied to some gas mixtures in ideal circumstances. The last section is devoted to a discussion of the time resolution in non-ideal circumstances and those nonidealities are applied to the CMS GEM detector.

6.1 Time resolution

6.1.1 Determination of the time offset

The raw signal pulse is processed by the electronics to amplify and deform the signal to a desired shape (e.g. Gaussian). The output is a voltage $v(t)$ or a current $i(t)$ signal as a function of time. Most electronics used in particle detectors yield a signal shape as shown in Fig. 6.1(a), where a large noise contribution is superimposed. The electronic equipment is followed by a discriminator which imposes a threshold on the signal. The time when the signal exceeds the threshold value is registered and can be used as a reference to determine the time when a charged particle passed through the detector. The value of the discriminator depends on the electronics and must be as low as possible to obtain high accurate time measurements. Moreover, the electronics noise must be kept as low as possible because it introduces an uncertainty (i.e. time jitter, see figure) on the time measurement. These requirements need a detailed design of the electronics as a whole and mostly imply the use of expensive electronic components.

The signal shape can be characterized with the peaking time t_p and the rise time t_r . t_p is defined as the time needed to go from zero signal to the signal maximum whereas t_r is defined as the time needed to go from 10% to 90% of the signal maximum. Both quantities are often mixed because they represent nearly the same information.

Depending on the desired quantity to measure (e.g. timing or charge), different methods exist to impose the threshold on the signal. Two basic methods are the constant fraction discriminator (CFD) and the leading edge trigger. In the latter, a fixed threshold is imposed independent of the signal and is therefore rather easy to implement. This method is used when

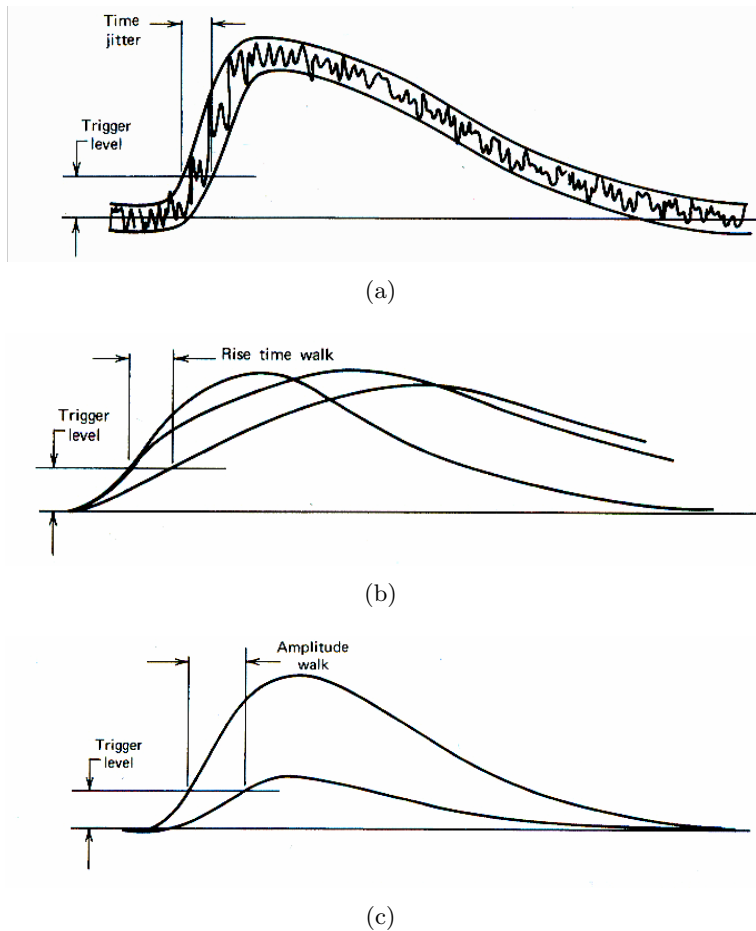


Figure 6.1: Typical voltage or current signal processed by the electronics with superimposed noise (a), rise time walk effect due to drift and diffusion fluctuations (b) and amplitude-walk effect due to gain variations (c). The images are adapted from [8].

the shape and characteristics as peaking time and amplitude remains the same. When the signal amplitude fluctuates from event to event, the constant fraction discriminator method is preferred. In this method the threshold is defined as a constant fraction of the signal amplitude. Different operations such as signal inverting, delays, etc. needs to be implemented for this method and is therefore more difficult to achieve.

6.1.2 Stochastic nature of a gaseous detector

After having discussed the method to extract time information from the signal, it is needed to investigate how the signal deviates from event to event. Indeed, because the processes in a gaseous detector are stochastic, uncertainties are introduced which are transferred to the signal. It is the purpose of this section to investigate the origin of these uncertainties for GEM detectors and how to reduce them. The total uncertainty arises from the different processes such as primary ionization and avalanche and can therefore be treated separately. The emphasis lies on the uncertainty on the primary ionization, which will be our major concern in the next sections when the timing characteristics are improved. As a guide through this section, we will use a GEM detector with 1 mm drift and induction region thickness and having standard GEM foil dimensions given in Table 3.1. The gas mixture is set to Ar-CO₂ with a composition of 75–25%. Events are generated from perpendicularly incident muons at initial coordinates $\mathbf{r}_0 = (0, 0, 0)$. Variations of these ideal circumstances will be discussed in section 6.4 at the end of this chapter.

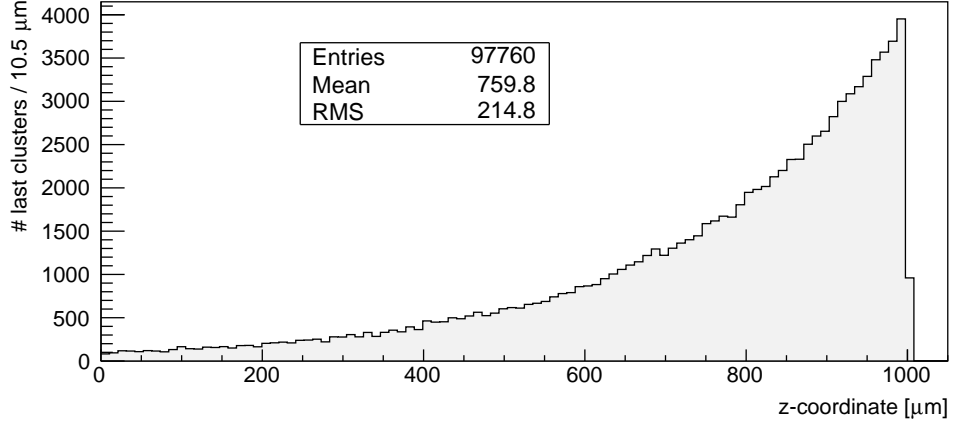


Figure 6.2: Simulated distribution $P(z, \theta, L, \lambda)$ describing the distribution of the z -coordinate of the last cluster. Simulations obtained with HEED using 10^5 100 GeV muons perpendicular incident on a GEM detector with gas composition Ar–CO₂ (75–25) (STP). Only 97760 events were registered yielding an efficiency of 97.76%.

Time jitter due to primary ionization

The dominant effect on the uncertainty of the time measurement is devoted to the primary ionization process. The amount of primary ionization encounters, or clusters, is described by Poisson statistics with mean and RMS equal to L/λ , with L the drift region thickness and λ^{-1} the cluster density, depending on the gas mixture. It is clear that the last cluster in the drift region, close to the GEM foil, will induce the first signal on the readout electrodes. Indeed, a noticeable signal is only induced from the time t_1 when the primary electron has entered the GEM hole because the signal induced when drifting to the hole is masked by the top metal electrode (see section 5.1.4). At $t \approx t_1$, the primary electron will trigger an avalanche and a collective charge will drift to the anode. Because the primary ionization is a stochastic process, the position of the last cluster differs from event to event as well as the time t_1 (mainly because the drift distance fluctuates) and thus the initial time of the induced pulse. A quantity related to these fluctuations is given by the spread of the z -coordinate of the last cluster, denoted as σ_z^I . Analogue, $\sigma_{t_0}^I$ is defined as the spread in time and depends on the kinematics of the charged particle. Both quantities are related through $\sigma_{t_0}^I = \sigma_z^I/v$, with v the speed of the charged particle. More generally, σ_z^I arises from a probability density function $P(z, \theta, L, \lambda)$ describing the probability of finding the last cluster in the interval dz . The distribution depends on the charged particle and incident angle, the gas and the thickness L of the drift region. For a Ar–CO₂ (75–25) gas mixture, the simulated distribution is shown in Fig. 6.2, compiled with HEED. Because HEED simulations are fast, a high amount of entries could be obtained yielding an accurate value of σ_z^I equal to $263.3 \mu\text{m}$. In the calculation 10^5 events were generated but only 97760 events were registered, yielding an ionization efficiency of 97.76%. The spread in time of the last cluster can be calculated as $\sigma_{t_0}^I \approx \sigma_z^I/c = 0.8783$ ps, with $v \approx c$ equal to the speed of light, because 100 GeV muons are relativistic. This very small spread in time can be neglected and the primary ionization encounters can be considered as instantaneous.

If the primary electrons of the last cluster are assumed to be liberated instantaneously at the same position (i.e. in the absence of δ -electrons or UV photons), they all arrive at the same time in the GEM hole (neglecting diffusion effects) and hence inducing a collective signal at the same time. In the first instance, we can assume the primary electrons drift towards the GEM hole with a constant drift velocity v_d . Furthermore, if the spread in time of the avalanche and drift process is neglected, the spread of the initial time of the induced signal

σ_t^I is equal to the spread in time of the last ionization cluster. The latter can be written as a function of σ_z^I and v_d according to:

$$\sigma_t^I = \frac{\sigma_z^I}{v_d}. \quad (6.1)$$

We will call σ_t^I the intrinsic¹ time resolution of the GEM detector and it represents a value for the global time resolution. Indeed, it does not represent an upper limit on the global time resolution because it does not incorporate drift, diffusion and gain variations which, in general, increases the value of σ_t^I . Furthermore, it is assumed the electrons in the last cluster create a detectable signal and are not lost due to attachment, recombination or trapping on the top electrode. In such cases the penultimate cluster must be used to create the signal, yielding a larger spread in time. Moreover, σ_t^I does not represent a lower limit because the drift velocity is not constant and must be averaged over its path to the GEM hole, yielding in general a higher drift velocity. Hence, σ_t^I neutralizes these opposite effects yielding a good first result of the (intrinsic) time resolution. Furthermore, it does not require a detailed simulation of the GEM detector which is very time consuming.

To continue the Ar-CO₂ example, the drift velocity is equal to $v_D = 45 \mu\text{m}/\text{ns}$ if the drift field in the drift region is 1.35 kV/cm (see Table 5.2). With these values, the intrinsic time resolution can be calculated as:

$$\sigma_t^I = \frac{214.8 \mu\text{m}}{45 \mu\text{m} \cdot \text{s}^{-1}} = 4.77 \text{ ns}. \quad (6.2)$$

Drift and diffusion variations

The drift process is accurately described with the electron mobility through the relation $\mathbf{v}_d = \mu\mathbf{E}$ and statistical fluctuations on the underlying process can be neglected. Due to diffusion, however, the concentrated swarm of electrons in the avalanche tend to spread in both longitudinal and transverse direction. The transverse diffusion yields a slightly broader signal because the electrons need more time to drift to the anode, though the time offset remains unattached. However, the broadening of the signal give rise to the time-walk effect as shown in Fig. 6.1(b) and introduces an additional uncertainty on the time measurement. The longitudinal diffusion directly influences the time offset but is negligible as the induced pulse already started just after the avalanche and before longitudinal diffusion could occur. It therefore only has a (small) contribution to the time-walk effect.

Gain variations

The contribution of (effective) gain variations on the time measurement is shown in Fig. 6.1(c). Because the avalanche process is a stochastic process with fluctuations described by a Polya distribution, the induced signals will fluctuate in amplitude. This effect is called amplitude-walk and can be reduced by obtaining a stable GEM gain. However, the effect on the time measurement can be reduced by using the CFD method, as described in the previous section. Another important effect concerning gain variations is the probability that the primary electrons from the last cluster will not induce a detectable signal because the avalanche is too weak. This effect can be resolved by obtaining a higher gain. However, higher gains results in larger fluctuations because $\sigma \propto \mu$ (see section 2.4.2) and a balance between both effects has to be determined.

¹Intrinsic is referred as independent of electronics.

6.1.3 Definition time resolution

Other effects also contribute to the uncertainty of the time measurement such as the incident angle and the energy of the charged particle. These contributions as well as the effect on the drift region thickness will be described in section 6.4. Moreover, the discussion up to now was based on single GEM detectors. When more GEM foils are added, the drift path of the charge carriers increases and diffusion will become more important. The uncertainty on the time measurement can be combined for all processes in one quantity $\sigma_{t,i}$, which we will call the intrinsic time resolution² as it only reflects uncertainties in the GEM detector. Furthermore, the electronics and noise will introduce an additional spread, denoted as $\sigma_{t,e}$. Both effects are independent and if the uncertainties are Gaussian, the total spread in time can be calculated as:

$$\sigma_t = \sqrt{\sigma_{t,e}^2 + \sigma_{t,i}^2}. \quad (6.3)$$

The total spread σ_t is called the time resolution and reflects the total uncertainty of the time measurement. In practice, the time resolution is measured with a large sample of events, e.g. with the use of cosmic muons. Two scintillators are installed above and below the GEM detector, both measuring the time when a muon passes through the scintillators. Scintillators have an excellent time resolution in the order of 100 ps resulting in an accurate measurement of the time when the muon hits the GEM detector. This time serves as a reference time and the time resolution can be extracted. Other methods for measuring the time resolution involves particle beams (pions or muons), generated with an accelerator.

It must be stressed that the intrinsic time resolution $\sigma_{t,i}$ describes all the uncertainties resulting from the stochastic processes in the GEM detector, independent of the electronics. As we discussed before, the introduced quantity σ_t^I is a good approximation of the total intrinsic time resolution $\sigma_{t,i}$. In the next sections we try to optimize $\sigma_{t,i}$ by calculating and comparing the values of σ_t^I , and where will identify σ_t^I with the intrinsic time resolution.

6.2 Time resolution optimization method

A lot of parameters such as the gas mixture and composition, environmental effects, GEM dimensions and voltages are able (or not) to optimize the time resolution. When taking all of these parameters into account, a tremendous amount of possibilities needs to be investigated and therefore an oriented approach is necessary. We first explain the optimization routes and deduce afterwards an optimization method or algorithm which will be applied in the next section.

6.2.1 Optimization routes

Cluster density. The dominant effect on the time resolution arises from the primary ionization time jitter and can be reduced by using gas mixtures with high cluster densities. Indeed, as more clusters will be created in the drift region, the spread σ_z^I of the last cluster will be reduced. Furthermore, the ionization efficiency will be increased.

Drift velocity. Using a gas with a high drift velocity results in a lower intrinsic time resolution as can be seen from Eq. 6.1. The drift region voltage and/or thickness must be adjusted in order to achieve the highest possible drift velocity. However, the electric field in the drift region is in general limited to 10 kV/cm in order to limit the total voltage across the GEM

²This definition of intrinsic time resolution contains all the stochastic effects including gain and diffusion variation. The intrinsic time resolution defined in the previous section was only defined with the uncertainty on the primary ionization (see further in the text).

detector. Furthermore, a fast signal is achieved when the drift velocity in the induction region is high, resulting in a fast charge collection and the time-walk effect is reduced. As a result, the electric field in the induction region is preferably equal to the field in the drift region, having both a maximized drift velocity.

Attachment. The attachment coefficient η must be chosen to be as low as possible over the entire electric field in the GEM detector. Attachment coefficients in the order of 100–1000 cm^{-1} will attach electrons even before the avalanche develops and no signal is induced. Lower attachment coefficients in the order of 10–100 cm^{-1} partially attach electrons resulting in weak signals. Furthermore, the probability that a primary electron from the last cluster will be attached is higher and the time resolution is increased because the penultimate cluster is used to create the first signal.

Gain. The electrons in the last cluster must induce a signal above the threshold and therefore the effective gain must be sufficient high. A stable gain is desired to minimize the amplitude walk and is achieved when the gain is not too high because $\sigma \propto \mu$, with μ the mean gain.

6.2.2 Optimization method

Taking the previous considerations into account, the optimization of the time resolution can be formulated in the following steps:

1. Select a gas mixture. Preferable mixtures are those with a high cluster density, high drift velocity, high Townsend coefficient and low attachment coefficient.
2. Generate the gas table with Magboltz, i.e. calculate gas parameters as a function of the electric field.
3. In the electric field region of 1–10 kV/cm, find the field value where the drift velocity is (locally) maximal.
4. Calculate σ_z^I with HEED and calculate the intrinsic time resolution σ_t^I .
5. Select a GEM geometry and determine the drift and induction voltages needed to achieve the electric fields in the previous step.
6. Select a GEM voltage based on the Townsend coefficient to achieve an appropriate gas and effective gain.
7. Generate the ANSYS files with the file generator and simulate the GEM with Garfield++.
8. Extract the effective gain. Adjust the GEM voltage if necessary if the gain is too low and repeat the previous step.
9. Extract timing information from the induced and convoluted pulses and compare to σ_t^I .

Step 1 and 2 are somewhat overlapping because the gas table is needed to select an appropriate gas mixture. In the first instance, the selection is based on the cluster density from single gases. The cluster density is generated with HEED for the available single gases of interest and is shown in Fig. 6.3. For gas mixtures, the cluster density is linear with the composition, i.e.:

$$\frac{1}{\lambda} = \sum_i \frac{n_i}{\lambda_i}, \quad (6.4)$$

Table 6.1: GEM dimensions used for optimizing the time resolution.

Drift region thickness	1 mm	Inner hole diameter	50 μm
Induct region thickness	1 mm	Outer hole diameter	70 μm
Pitch	140 μm	Rim	70 μm
Kapton thickness	50 μm	Metal thickness	5 μm

with n_i the fraction and λ_i^{-1} of constituent i . The other desired gas properties such as a high Townsend, a high drift velocity and low attachment coefficient are achieved by adding other gas constituents and the gas table must be calculated for the selected gas mixture. Because this process is very time consuming (in the order of 12 hours per gas table), the gas tables were generated in parallel on the STEVIN Supercomputer.

The Townsend coefficient is crucial to adjust the gain and effective gain of the detector. The Ar-CO₂ mixture can serve as a reference value to obtain a gas gain in the order of 170 with a Townsend coefficient of 1850 cm⁻¹. However, the Penning effect is incorporated in the simulation which leads to a higher gain. Because the Penning effect is disabled in the following simulations due to missing information of the Penning transfer rates, Townsend coefficients in the order of 2000 cm⁻¹ will be sufficient. Though, the GEM voltage must be adjusted as the effective gain can be considerably lower than the gas gain, depending on the electrostatics.

The extraction of timing information from the raw and convoluted pulses always requires the introduction of a threshold. A threshold value on the charge is implemented in the analysis of the pulses, but it turns out the time resolution is very sensitive to the threshold value. Therefore it is not possible to extract accurate timing information and other methods must be implemented in order to obtain the time resolution. Due to lack of time, other methods are not implemented and we settle with the intrinsic time resolution σ_t^I .

6.3 Time resolution optimization

The optimization method deduced in the previous section is now applied on a single GEM detector. The GEM dimensions used are listed in Table 6.1. To reduce computation time, the drift region was set to 1 mm to reduce the amount of primary electrons and hence to reduce the calculation of the avalanches. The environmental parameters are set to standard temperature and pressure (STP). For each simulation, 100 events were calculated consisting of 100 GeV muons, perpendicularly incident at $\mathbf{r}_0 = (0, 0, 0)$. The calculation of σ_t^I is repeated over 10⁴ times to achieve an accurate result. The local maximum of the drift velocity is visually determined using the ROOT browser by selecting the highest drift velocity in the electric field region below 10 kV/cm. This is accurate up to a few $\mu\text{m}/\text{ns}$. The drift velocities of the gases used in this section are plotted in Appendix C.

In principle, every gas mixture can be used which is available in the Garfield++ database. In practice, however, not every gas mixture is suitable for gas detectors as some gases are flammable or are expensive. Such constraints are not taken into account in the following discussion. However, recent policies supported by research organizations such as CERN discourage the use of greenhouse gases. In later stages the use of strong greenhouse gases will be even forbidden. To tackle this, we separate our search for optimal gas mixtures in non-greenhouse and greenhouse gas mixtures.

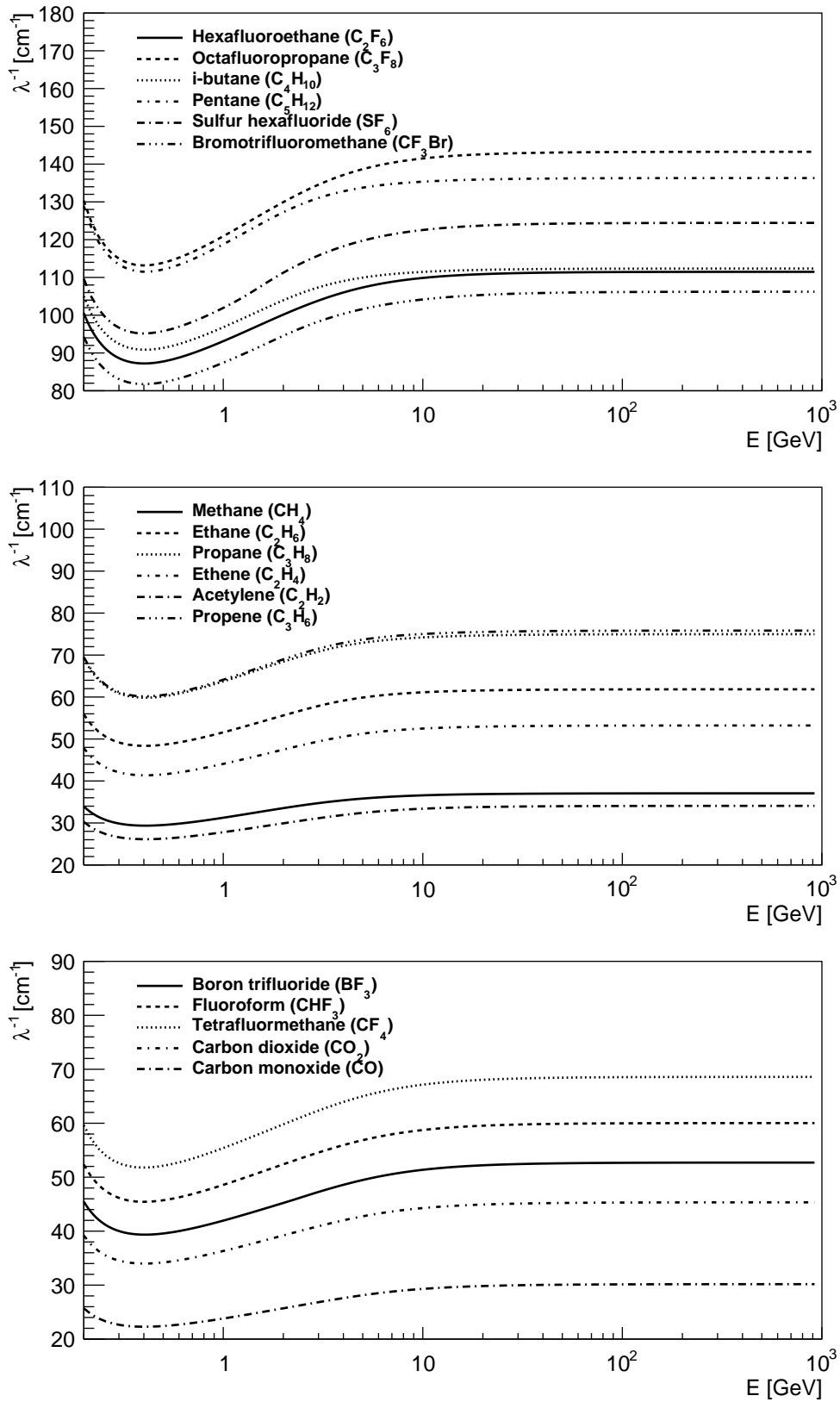


Figure 6.3: Cluster densities for the gases of interest as a function of the muon energy. Plots obtained with HEED simulations at STP.

6.3.1 Non-greenhouse gas mixtures

A number of non-greenhouse gas mixtures were calculated and the intrinsic time resolution was extracted. The results, listed in Table 6.3, will now be briefly discussed and a general conclusion will be drawn at the end of this section.

Ar-CO₂ mixtures

In the first sections of this chapter, the Ar-CO₂ (75-25) gas mixture was used as an example to calculate the intrinsic time resolution equal to 4.77 ns, given a drift region electric field of 1.35 kV/cm. As shown in Fig. 5.1, the local maximum of the drift velocity is equal to 74 $\mu\text{m}/\text{ns}$ at an electric field of 7 kV/cm. Hence, the intrinsic time resolution can be improved to:

$$\sigma_t^I = \frac{214.8 \mu\text{m}}{74 \mu\text{m} \cdot \text{s}^{-1}} = 2.90 \text{ ns.} \quad (6.5)$$

The corresponding drift and induction region voltages are equal to 700 V. Two single GEMs have been simulated with GEM voltages of 400 and 450 V respectively. In the first case, the Townsend coefficient α is equal to 1450 cm^{-1} , yielding a gas gain of 215.384 and an effective gain of 68.864 ($\xi \approx 0.32$). In the latter a gas gain of 72.734 and an effective gain of 20.727 is obtained ($\xi \approx 0.32$) with a Townsend coefficient equal to 1750 cm^{-1} . It must be stressed that the Penning effect is enabled in these calculations yield higher gains w.r.t. the magnitude of α .

C₅H₁₂

Based on the cluster density λ^{-1} , C₅H₁₂ (pentane) is the best non-greenhouse gas with a cluster density of 137 cm^{-1} for 100 GeV muons (see Fig. 6.3). A local maximum of the drift velocity 55 $\mu\text{m}/\text{ns}$ is observable at an electric field of 4 kV/cm. The spread of the last cluster is simulated and is equal to $\sigma_z^I = 74.29 \mu\text{m}$, resulting in an intrinsic time resolution of $\sigma_t^I = 1.35 \text{ ns}$. The Townsend coefficient is low compared to Ar-CO₂ (75-25) as can be seen from Fig. 2.5 and it is expected large GEM voltages must be applied to achieve an appropriate gain.

Table 6.2: Simulation results for C₅H₁₂.

V_{GEM} [V]	E_{GEM} [kV/cm]	α [cm^{-1}]	G	G_{eff}
500	100	623.0	1.623	1.150
600	120	1039.6	3.195	2.125
700	140	1456.2	9.28	5.773
800	160	1872.8	55.26	19.816

Four GEMs have been simulated with a drift and induction voltage of 400 V to investigate the gain as a function of this GEM voltage. The results are shown in Table 6.2. The Townsend coefficients were linear extrapolated with the data available from Fig. 2.5 and evaluated at the GEM hole field magnitude. Large GEM voltage above 800 V are indeed needed to achieve acceptable gains.

C₄H₁₀

The second suitable non-greenhouse gas is C₄H₁₀ (butane), again based on the cluster density. The drift velocity is comparable to C₅H₁₂ and shows a local maximum of 54 $\mu\text{m}/\text{ns}$ at 6 kV/cm. The Townsend coefficient (see Fig. 2.5) is double w.r.t. the C₅H₁₂ coefficient and

therefore lower GEM voltages will be needed. On the other hand, because the cluster density is lower, a higher intrinsic time resolution of $\sigma_t^I = 1.65$ ns is obtained, with σ_z^I equal to 89.14 μm . With the given parameters for the drift and induction voltages, a single GEM is simulated with $V_{\text{GEM}} = 600$ V, yielding a gas gain of 18 and an effective gain of 9.82. Again, high GEM voltages in the order of 600–800 V needed to operate with an appropriate gain.

C₄H₁₀–C₅H₁₂

Although high GEM voltages were needed in the previous simulated gas mixtures, both gases are now combined and an optimal composition is determined. In Table 6.3, the calculated compositions are listed and both gas table and σ_z^I were determined for each composition. The best time resolution is obtained with a high amount of C₅H₁₂, but the Townsend coefficient is subsequently lower. To compromise both, the C₄H₁₀–C₅H₁₂ (60–40) composition is selected with a time resolution of 1.49 ns. Two GEMs were simulated with $V_{\text{GEM}} = 600$ V and 700 V, both having $V_{\text{drift}} = V_{\text{induct}} = 420$ V. Only the second GEM with $V_{\text{GEM}} = 700$ V results in a more acceptable gas gain of 42.9 and an effective gain of 20.92.

CO₂–C₅H₁₂

Compared to C₄H₁₀, CO₂ has a slight lower drift velocity, a lower cluster density and a nearly equal Townsend coefficient in the high field regime. Therefore, CO₂–C₅H₁₂ mixtures are able to operate at lower GEM voltages but the time resolution will be increased. Different compositions were calculated (see table) and based on the Townsend coefficient the (40–60) composition is selected having a time resolution of 1.73 ns. A GEM with $V_{\text{drift}} = V_{\text{induct}} = 800$ V is simulated with a GEM voltage equal to 650 V. The gas gain is equal to 64.55 with an effective gain of 34.06.

Ar–C₅H₁₂ and Xe–C₅H₁₂

Both Argon and Xenon have large Townsend coefficients up to 2500 cm^{-1} at 100 kV/cm and are therefore also suitable to increase α of pure C₅H₁₂. Furthermore, the Townsend coefficient of Ar and Xe is higher than CO₂ and it is thus expected that α is increased w.r.t. CO₂–C₅H₁₂ mixtures. Unfortunately, the Townsend coefficient of both Ar–C₅H₁₂ and Xe–C₅H₁₂ is reduced to 1200 cm^{-1} at 100 kV/cm and no advantage based on α is achieved. From the table, the Ar–C₅H₁₂ (40–60) and Xe–C₅H₁₂ (40–60) were selected and simulated with the corresponding optimal drift and induction voltages. The first mixture, having a time resolution of 1.93 ns, is simulated with a GEM voltage of 600 V yielding a gas and effective gain of 32.47 and 10.77 respectively. The time resolution of the second selected mixture is 1.86 ns and is simulated with a GEM voltage of 650, yielding a higher gas gain of 58.23 and effective gain of 25.39 which is indeed slightly lower than the CO₂–C₅H₁₂ (40–60) gain.

Ar–C₄H₁₀ and Xe–C₄H₁₀

The same gas mixtures as in the previous paragraph were calculated with C₅H₁₂ replaced by C₄H₁₀ to obtain a higher Townsend coefficient. Indeed, after generating the gas tables, a Townsend coefficient 1500 cm^{-1} is achieved for both Ar–C₄H₁₀ (20–80) and Xe–C₄H₁₀ (20–80) at 100 kV/cm. The intrinsic time resolution of both gas mixtures are very close to each other in the order of 1.9 ns. No simulations has been performed on these gas mixtures, however.

Table 6.3: Results of gas tables and σ_z^I for various non-greenhouse gas mixtures. The intrinsic time resolution σ_t^I is calculated from the parameters by using Eq. 6.1. (*) no local maximum was found for these gases; a field of 8 kV/cm was used.

Gas mixture	$v_{d,\max}$ [$\mu\text{m}/\text{ns}$]	$E(v_{d,\max})$ [kV/cm]	σ_z^I [μm]	σ_t^I μm [ns]
Ar-CO ₂ 75-25	75	7.0	214.8	2.90
C ₅ H ₁₂	55	4.0	74.29	1.35
C ₄ H ₁₀	54	6.0	89.17	1.65
Xe-CO ₂ 75-25	45	2.1	178.2	3.96
CO ₂ *	90	8.0	193.6	2.15
C ₃ H ₈	50	4.5	126.8	2.54
C ₄ H ₁₀ -C ₅ H ₁₂ 80-20	53	4.5	85.05	1.60
C ₄ H ₁₀ -C ₅ H ₁₂ 60-40	55	4.2	82.0	1.49
C ₄ H ₁₀ -C ₅ H ₁₂ 40-60	55	4.1	77.53	1.41
C ₄ H ₁₀ -C ₅ H ₁₂ 20-80	55	4.1	74.21	1.34
CO ₂ -C ₅ H ₁₂ 80-20*	70	8.0	158.7	2.27
CO ₂ -C ₅ H ₁₂ 60-40*	63	8.0	119.8	1.9
CO ₂ -C ₅ H ₁₂ 40-60	58	8.0	100.5	1.73
CO ₂ -C ₅ H ₁₂ 20-80	58	6.0	84.84	1.46
Ar-C ₅ H ₁₂ 80-20	46	2.1	172.9	3.76
Ar-C ₅ H ₁₂ 60-40	55	2.1	130.1	2.36
Ar-C ₅ H ₁₂ 40-60	55	2.1	105.9	1.93
Ar-C ₅ H ₁₂ 20-80	55	4.0	84.11	1.53
Xe-C ₅ H ₁₂ 80-20	40	2.0	135.6	3.39
Xe-C ₅ H ₁₂ 60-40	48	3.0	112.3	2.34
Xe-C ₅ H ₁₂ 40-60	51	4.1	94.88	1.86
Xe-C ₅ H ₁₂ 20-80	55	4.1	82.76	1.50
Ar-C ₄ H ₁₀ 80-20	50	1.0	182.9	3.66
Ar-C ₄ H ₁₀ 60-40	50	2.1	149.6	2.99
Ar-C ₄ H ₁₀ 40-60	53	4.0	124.2	2.34
Ar-C ₄ H ₁₀ 20-80	54	4.5	101.7	1.88
Xe-C ₄ H ₁₀ 80-20	38	2	141.9	3.7
Xe-C ₄ H ₁₀ 60-40	44	2.05	122.4	2.78
Xe-C ₄ H ₁₀ 40-60	50	4.2	109.7	2.19
Xe-C ₄ H ₁₀ 20-80	52	4.5	99.43	1.91

Xe-CO₂ mixtures

For 100 GeV muons, the cluster density of Xenon is around 1.6 times higher than the cluster density of Argon. Therefore, it might be possible to improve the Ar-CO₂ (75-25) time resolution by replacing Ar with Xe. In this mixture, the local maximal drift velocity is 45 $\mu\text{m}/\text{ns}$ at a field of 2.1 kV/cm. The spread of the last cluster σ_z^I is equal to 178.2 μm , yielding an intrinsic time resolution of $\sigma_t^I = 3.96$ ns. This value is higher than the optimized Ar-CO₂ mixture (with $\sigma_t^I = 2.90$ ns) due to its lower drift velocity. Hence, no improvement is made and this mixture is not further simulated.

Summary

From the previous discussion it is clear that the presence of both C₅H₁₂ and C₄H₁₀ led to improved values of the time resolution. However, the Townsend coefficients of both gases are relative small and therefore other gas constituents such as Ar, Xe or CO₂ must be added to

increase α . The $\text{CO}_2\text{-C}_5\text{H}_{12}$ (40–60) and $\text{Xe-C}_5\text{H}_{12}$ (40–60) mixtures provides time resolutions in the order of 1.8 ns operating at GEM voltages of 650–750 V to achieve an appropriate gain. However, the last gas mixture is more suitable because the drift and induction fields must be 4.1 kV/cm. The total gain can be increased by adding more GEM stages with transfer fields equal to 4.1 kV/cm in order to obtain fast signals. The $\text{C}_4\text{H}_{10}\text{-C}_5\text{H}_{12}$ (60–40) mixture is also a possible candidate with a time resolution of 1.5 ns but higher GEM voltages are needed in the order of 700–800 V. A third possible candidate is $\text{Ar/Xe-C}_4\text{H}_{10}$ (20–80) with a time resolution of 1.9 ns. Based on the Townsend coefficient, it is expected that such gas mixtures could operate with lower GEM voltages, but these simulations still needs to be performed.

6.3.2 Greenhouse gas mixtures

In this section three additional greenhouse gases are introduced: CF_4 , C_3F_8 and C_2F_6 . Because the high amount of fluorine atoms, attachment has to be taken into account and the attachment coefficient is plotted in Fig. 2.4 for the three pure gas mixtures as a function of the electric field. The drift velocities for the different calculated gas mixtures are again plotted in appendix C. Table 6.5 summarizes all the calculated gas mixtures and a brief discussion is given below.

CF_4

The drift velocity of pure CF_4 is plotted in Fig. 2.3 and a large maximum of 145 $\mu\text{m}/\text{ns}$ at 5 kV/cm is visible. Of all the common gases used in particle detectors, CF_4 is by far the fastest gas in the low electric field region. At an electric field magnitude of 100 kV/cm, Townsend coefficient is in the order of 2000 cm^{-1} and is almost equal to the effective Townsend coefficient as the attachment coefficient is around 50 cm^{-1} at 100 kV/cm. A manageable maximal η value of 110 cm^{-1} is observed at 35 kV/cm (see Fig. X). These excellent properties make it possible to use CF_4 as a pure gas mixture. The spread is calculated to be $\sigma_z^I = 145.3\ \mu\text{m}$, yielding an intrinsic time resolution of 1.00 ns. Three GEMs have been simulated with $V_{\text{drift}} = V_{\text{induct}} = 500\text{ V}$ and the results are listed in Table 6.4. Appropriate gains are obtained with acceptable GEM voltages, resulting in an excellent gas with good time resolution.

Table 6.4: Simulation results for CF_4 . (*) linear extrapolated from the available data.

V_{GEM} [V]	E_{GEM} [kV/cm]	α [cm^{-1}]	G	G_{eff}
400	80	1300	7.16	1.22
500	100	1950	40.97	7.32
600	120	2632*	324.41	52.91

$\text{C}_5\text{H}_{12}\text{-CF}_4$

W.r.t. the previous $\text{Xe-C}_5\text{H}_{12}\text{-CF}_4$ mixtures, the time resolution can be improved if the Xe constituent is removed because it has a low cluster density. After the calculation of the gas tables and σ_z^I , such gas mixtures indeed yield a time resolution in the order of 1–1.2 ns (see Table). On the other hand the removal of Xe will reduce the Townsend coefficient and higher GEM voltages are needed. The 40–60 composition is calculated with $V_{\text{drift}} = V_{\text{induct}} = 550\text{ V}$ and V_{GEM} equal to 550 V. The gas gain is simulated to be 26.06 with an effective gain of 8.32. Hence, the GEM voltage needs to be increased up to 650–750 V in order to achieve suitable gains. Such simulations have not been performed yet.

Table 6.5: Results of gas tables and σ_z^I for various greenhouse gas mixtures. The intrinsic time resolution σ_t^I is calculated from the parameters by using Eq. 6.1.

Gas mixture	$v_{d,\max}$ [$\mu\text{m}/\text{ns}$]	$E(v_{d,\max})$ [kV/cm]	σ_z^I [μm]	σ_t^I μm [ns]
CF ₄	145	5.0	145.3	1.00
C ₃ F ₈	113	12.0	69.90	0.62
CHF ₃	20.00	8.0	159.2	7.96
BF ₃	100.0	8.5	182.5	1.83
C ₃ F ₈ -CO ₂ 50-50	75.0	8.0	104.6	1.39
C ₅ H ₁₂ -CF ₄ 80-20	71	4.1	83.4	1.17
C ₅ H ₁₂ -CF ₄ 60-40	87	5.0	92.22	1.06
C ₅ H ₁₂ -CF ₄ 40-60	100	5.5	103.5	1.04
C ₅ H ₁₂ -CF ₄ 20-80	118	5.5	119.8	1.02
C ₅ H ₁₂ -C ₂ F ₆ 80-20	70	6.0	76.42	1.09
C ₅ H ₁₂ -C ₂ F ₆ 60-40	82	6.0	78.59	0.96
C ₅ H ₁₂ -C ₂ F ₆ 40-60	90	6.2	82.47	0.92
C ₅ H ₁₂ -C ₂ F ₆ 20-80	100	7.5	84.93	0.85
Xe-C ₅ H ₁₂ -CF ₄ 60-20-20	66	4.0	128.7	1.95
Xe-C ₅ H ₁₂ -CF ₄ 60-10-30	80	4.0	144.2	1.8
Xe-C ₅ H ₁₂ -CF ₄ 60-30-10	58	4.0	120.7	2.08
Xe-C ₅ H ₁₂ -CF ₄ 40-20-40	90	4.1	127.8	1.42
Xe-C ₅ H ₁₂ -CF ₄ 40-40-20	70	4.1	109.6	1.56
Xe-C ₅ H ₁₂ -CF ₄ 40-30-30	80	4.1	118.8	1.49
Xe-C ₅ H ₁₂ -CF ₄ 50-25-25	75	4.1	127.7	1.66
Xe-C ₅ H ₁₂ -C ₃ F ₈ 60-20-20	70	4.1	108.9	1.56
Xe-C ₅ H ₁₂ -C ₃ F ₈ 60-10-30	80	6.2	110.6	1.38
Xe-C ₅ H ₁₂ -C ₃ F ₈ 60-30-10	62	4.0	109.1	1.75
Xe-C ₅ H ₁₂ -C ₃ F ₈ 40-20-40	85	6.2	88.97	1.04
Xe-C ₅ H ₁₂ -C ₃ F ₈ 40-40-20	70	5.0	95.09	1.36
Xe-C ₅ H ₁₂ -C ₃ F ₈ 40-30-30	78	6.15	95.16	1.22
Xe-C ₅ H ₁₂ -C ₃ F ₈ 50-25-25	75	6.0	98.2	1.31

Xe-C₅H₁₂-CF₄

To reduce the amount of greenhouse gas, a mixture of Xe-C₅H₁₂-CF₄ is proposed. Xenon is used as the basis with a high value of α , and additional gas constituents are added to increase the cluster density (C₅H₁₂) and the drift velocity (CF₄). Different compositions were calculated and the results are listed in Table 6.5. The gas composition (40-20-40) is chosen based on its low time resolution (equal to 1.42 ns), taking the Townsend coefficient into account ($\alpha = 2200 \text{ cm}^{-1}$ at 100 kV/cm). The GEM is simulated with $V_{\text{drift}} = V_{\text{induct}} = 410 \text{ V}$ and $V_{\text{drift}} = 500 \text{ V}$, yielding a gas gain equal to 64.73 and an effective gain of 18.92.

C₃F₈ and C₂F₆

Theoretically, the best time resolution is achieved with C₃F₈. Indeed, with a local maximal drift velocity of 113 $\mu\text{m}/\text{ns}$ and $\sigma_z^I = 69.9$, an intrinsic time resolution 619 ps is obtained. However, the eight fluoride atoms result in a high maximal attachment coefficient of 840 cm^{-1} at an electric field magnitude of 40 kV/cm. Furthermore, in the field region of 20–130 kV/cm, the attachment coefficient is higher than 300 cm^{-1} . It is thus expected that many electrons will be attached leading to low values of the gain. Indeed, when simulating the GEM in the optimized configuration (i.e. with matched drift and induction electric fields),

all the primary electrons were attached, independent of the GEM voltage. As a result, the usage of pure C_3F_8 is limited because every primary electron will be attached, independent of the electric fields. The same conclusion can be drawn for pure C_2F_6 which has a maximal attachment coefficient of 600 cm^{-1} at 33 kV/cm .

Xe- C_5H_{12} - C_3F_8 and C_5H_{12} - C_2F_6

Because C_3F_8 is proved to be not useful as a gas mixture for particle detectors, it is possible to form combinations with this constituent. For example, the intrinsic time resolution for different gas compositions of Xe- C_5H_{12} - C_3F_8 were calculated and shown in the table. The best time resolution is obtained with a high amount of C_3F_8 . However, the attachment coefficient remains very high, up to a maximal η of 200 cm^{-1} for the 60-30-10 mixture. After simulating the 40-40-20 composition, it was found all the electrons were attached and a gain of zero is obtained. The same conclusions can be drawn for C_5H_{12} - C_2F_6 were the intrinsic time resolution is calculated and listed in the table. After simulating with the 80-20 gas mixture, all the electrons were attached and a effective gain of zero is obtained.

Summary

Based on the cluster density, the C_3F_8 and C_2F_6 gases were promising to improve the time resolution. However, it turns out the large attachment coefficient makes both gases unsuitable because too much electrons were attached, yielding very low gain values. On the other hand, CF_4 is proven to be a gas with excellent properties such as Townsend coefficient, drift velocity and attachment. It can be used as a standalone gas or used in composition with, for example, C_5H_{12} , yielding a time resolution in the order of 1-1.2 ns. Further investigation needs to be done to reduce the amount of CF_4 as it is a strong greenhouse gas.

6.4 Non-ideal circumstances

In the previous section, the ideal circumstances were defined as events with 100 GeV muons perpendicularly incident on a GEM detector with 1 mm drift region thickness. Three nonidealities, being the effect of the drift region thickness, the incident muon energy and angle will affect σ_z^t and therefore the time resolution and are discussed in this section. This knowledge will be applied on the CMS GEM detectors in the last section of this paragraph.

6.4.1 Drift region thickness

Based on the Poisson statistics, it is possible to derive an analytic expression for the distribution $P(z, \theta, L, \lambda)$ and therefore the calculation of the RMS as a function of the drift region thickness and the gas parameter λ is possible. However, the approach used here is to investigate directly the effect of the drift region thickness with the use of simulations. Five GEMs with a drift region thickness of 1, 2, 3, 4 and 5 mm were simulated with different gases. The result is shown in Fig. 6.4. For gases with a high cluster density (Ar- C_5H_{12} in the figure) the spread σ_z^I is almost independent of the drift region thickness. On the other hand, the spread σ_z^I of gases with a low cluster density (Ar- CO_2) tend to decrease at a small drift region thickness of 1-2 mm. The spread σ_z^I for intermediate cluster densities such as Xe and CF_4 only tend to decrease at a low drift region thickness of 1 mm. The dependence on σ_z^I on the drift region thickness for a specific gas mixture clearly converges to a constant value at large thicknesses and this value can be used as an upper limit of σ_z^I .

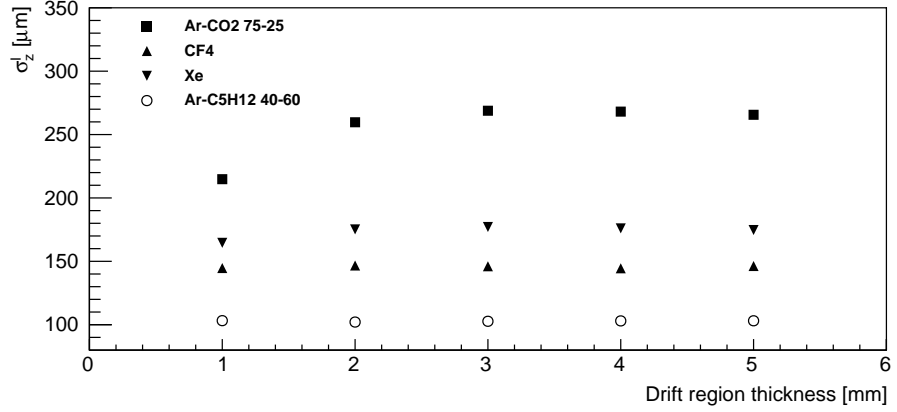


Figure 6.4: Simulated last cluster spread σ_z^I for different gas mixtures. The data points were obtained by using five single GEMs with different drift region thickness. For each point 10^5 100 GeV muons were perpendicular incident at STP.

6.4.2 Muon energy

As already discussed in section 6.1.2, the spread σ_z^I increases when the cluster density is increased. The latter is related to the muon energy with the curves obtained in Fig. 6.3. As a result, the spread σ_z^I and the time resolution is related to the muon energy but this dependence is rather low for high relativistic muons as the cluster density is almost constant in this high energy region. For low energy particles below 1 GeV, the cluster density increases yielding low values for σ_z^I . This behavior is obtained with simulations for three gas mixtures and muon energies ranging from 100 MeV to 1 TeV. The results are listed in Table 6.6.

Table 6.6: Spread of the last cluster σ_z (units: μm) as a function of the energy for different gas mixtures. The simulations were performed on a single GEM with 1 mm drift region thickness and 10^4 perpendicularly incident muons at STP.

	Ar-CO ₂	CF ₄	C ₅ H ₁₂
100 MeV	191.6	111.6	70.14
1 GeV	234.2	165.5	71.16
10 GeV	215.9	139.6	70.76
100 GeV	211.7	136.4	70.41
1 TeV	211.6	141.9	69.61

6.4.3 Incident angle

The incident direction of the charged particle can be described by the angle θ w.r.t. the normal of the GEM detector (z -direction) and the angle ϕ describing the transverse direction. Because the GEM detector is symmetric in the transverse direction, the simulation and measurements are, on average, independent of ϕ . When θ increases, more ionizations occur in the drift region because the ionization track length L_I increases according to:

$$L_I = \frac{d_{\text{drift}}}{\cos \theta}. \quad (6.6)$$

Hence, both σ_z^I and σ_t^I decreases when θ increases. This result is obtained with single GEM simulations with $d_{\text{drift}} = 3$ mm and incident muons with different θ angles. The results are shown in Table 6.7. The decrease in time resolution is only valid if the events are generated with a constant known incident angle, which is for example not the case in CMS where

Table 6.7: Spread of the last cluster σ_z (units: μm) as a function of the angle θ for a Ar-CO₂ (75–25) gas mixture. The simulations were performed on a single GEM with 3 mm drift region thickness and 10^4 100 GeV perpendicularly incident muons at STP.

Angle [°]	0	15	30	45	60	75
σ_z^I [μm]	269.0	255.5	227.0	188.7	132.1	69.3
σ_t^I [ns]	3.6	3.45	3.07	2.55	1.78	0.94

muons are spread with different θ angles (see next section). Furthermore, large θ values tend to spread out the primary ionization in the transverse direction yielding a degradation of the spatial resolution and the charge collected on the readout strips. These effects, as well as others, will also affect the time resolution and more investigation is needed, however.

6.4.4 CMS GEM detectors

The previous nonidealities are manifested as follows in the CMS GEM GE1/1 detectors:

- drift region: the drift region thickness of the GEM detectors is equal to 3 mm;
- incident angle: the GE1/1 sector covers the high η -region ($1.6 < \eta < 2.1$) and therefore the incident muons have an isotropic angle in the interval $\theta \in [13.96^\circ, 22.38^\circ]$;
- energy: the energies of interest are in the 1–1000 GeV muon energy region.

The two proposed gas mixtures for operation, Ar-CO₂ (75–25) and Ar-CO₂-CF₄ (45–15–40), were simulated including these nonidealities. The muons are isotropic generated in the high η -region yielding a value for σ_z^I of 251.7 and 186.2 μm respectively. The corresponding intrinsic time resolutions obtained are 3.4 ns and 1.77 ns respectively.

6.5 Summary

The algorithm developed in section 6.2 is applied to several gas mixtures, where a distinction was made between greenhouse and non-greenhouse gas mixtures. The intrinsic time resolution is compared with the Ar-CO₂ (75–25) as a reference gas mixture. Pure C₅H₁₂ and C₄H₁₀ led to improved values of the time resolution but high GEM voltage were needed due to the low Townsend coefficient. By adding Ar, Xe or CO₂, the Townsend coefficient was increased. Gas mixtures such as Xe-C₅H₁₂ and Ar/Xe-C₄H₁₀ (20–80) were promising with an intrinsic time resolution below 2 ns and having reasonable Townsend coefficients. Based on the cluster density, the C₃F₈ and C₂F₆ gases were promising to improve the time resolution but due to their high attachment coefficient, very low gains were observed and therefore are not suitable. On the other hand, CF₄ is proven to be a gas with excellent properties such as Townsend coefficient, drift velocity and attachment. It can be used as a standalone gas or used in composition with, for example, C₅H₁₂, yielding a time resolution in the order of 1–1.2 ns. Further investigation needs to be done to reduce the amount of CF₄ because it is a strong greenhouse gas. Afterwards, the nonidealities were briefly discussed. A small dependence of σ_z^I on the drift region thickness was observed with gases having low cluster densities, but almost immediately converged to a constant value when higher drift region thicknesses were used. The dependence of the muon energy was found to be negligible as the cluster density λ^{-1} is almost constant for muons with energies above 1 GeV. The incident angle clearly influences the spread σ_z^I because non-perpendicularly incident muons leave a larger ionization track length in the drift region, hence decreasing the value of σ_z^I . However, large incident angles tend to spread out the primary ionization in the transverse direction, yielding a degradation of the spatial resolution and the charge collected on the readout strips.

Chapter 7

Summary and outlook

7.1 Summary

High Energy Particle physics nowadays make use of powerful accelerators to accelerate beams with elementary particles in order to collide them head on. In such collisions, the energy available materializes with the production of many particles distributed over the total solid angle. Sophisticated detectors are needed which must be fast and accurate to detect and identify these particles, from which physical results can be extracted. A new promising type of detector is the Gas Electron Multiplier (GEM), developed in the late nineties by F. Sauli. The triple GEM is proposed for the upgrade of the Compact Muon Solenoid (CMS) at the CERN Large Hadron Collider. Due to its excellent rate capabilities, excellent spatial and time resolutions, radiation resistance and capability to operate in high magnetic fields, it can cope with the expected high radiation environment in the CMS forward region during the high luminosity phase of the collider. Further research is ongoing to improve the properties and performance.

In this paper, the time response of GEM detectors has been studied using several simulation packages. ANSYS Inc. is used to define the GEM geometry in terms of a unit cell. Making use of the Finite Element Method, the potential is calculated in the gas medium for a fixed set of boundary conditions, i.e. for a fixed set of voltages applied on the electrodes. Garfield++ is then used for the calculations of the primary ionization, charge transport and signal creation. This software package combines different standalone programs such as HEED and Magboltz. Finally, ROOT is used to analyze the results. To work efficiently with these programs, a local simulation environment is set up which acts as an interface between the different software packages. A program is written in HTML/PHP where the GEM dimensions and potentials can be submitted via a browser-based graphical user interface. The necessary ANSYS files are generated as well as a file containing the geometry and potentials in a human-readable format. This file can be imported in Garfield++ such that the GEM dimensions are accessible. The simulations were performed on two supercomputers, the CERN computing grid and the STEVIN supercomputer at Ghent University.

A single GEM with standard gas mixture Ar-CO₂ (75–25) was simulated with perpendicularly incident 100 GeV muons. The gas gain was calculated from the avalanche size which was recorded for each primary electron. The gain variations are described with a Polya distribution and a mean gain of 171.2 was observed. However, not every electron in the avalanche will induce a signal because it is possible that electrons are collected on the GEM foil electrodes or trapped on the kapton layer. This results in a lower gain and the effective gain is defined as the total amount of electrons which are captured by the anode. In the simulations, an effective gain of 69.31 is obtained, corresponding with 40.84% of the total gas gain. In order to understand the total induced signal from a muon, the induced signal

of a single primary electron is investigated. A block pulse is observed, as expected from the Shockley-Ramo theorem, with a time offset equal to the drift time of the primary electron towards the GEM hole. A noticeable signal is induced when the avalanche starts in the GEM hole. The duration of the pulse is equal to the drift time in the induction region. It turns out the time offset and pulse duration can be described with the drift velocity kinematics of electrons, assuming a constant field in the drift and induction region. The total pulse from several primary electrons is a superposition in time of the individual pulses from the primary electrons. The simulations have been compared to experimental data. The gain of a single GEM was calculated as a function of the GEM voltage and the drift field. Consistent behavior with the experimental results were observed, though the simulated gain was reduced with a factor 3.

The measurement of the time coordinate when a charged particle passed through the detector is obtained by imposing a threshold value on the signal processed by the electronics. Because the processes in a gaseous detector are stochastic, the time measurement is subjected to uncertainties which defines the time resolution of a detector. The dominant contribution of the time resolution is the time jitter derived from the primary ionization. Indeed, the electrons from last cluster in the drift region will induce the first signal on the anode. Due to the stochastic process of primary ionization described by Poisson statistics, the spread of the last cluster σ_z^I (along the z -axis, perpendicular to the GEM plane) is related to the spread the time measurement. The intrinsic time resolution is then defined as $\sigma_t^I = \sigma_z^I/v_d$, with v_d the drift velocity in the drift region. With this definition of the time resolution, effects such as gain and diffusion variations as well as the electronics are not taken into account. Together with other general considerations, an algorithm is developed to search for optimal gas mixtures and to adjust the GEM voltages and/or dimensions with the aim of optimizing the intrinsic time resolution. It is based on finding a gas mixture with a high cluster density (reducing σ_z^I) and to optimize electric field in the drift region such that the drift velocity is maximal (increase v_d). Afterwards, a suitable the GEM voltage is obtained by simulation.

The algorithm developed is applied to several gas mixtures, where a distinction was made between greenhouse and non-greenhouse gas mixtures. The intrinsic time resolution is compared with the Ar-CO₂ (75-25) as a reference gas mixture. Pure C₅H₁₂ and C₄H₁₀ led to improved values of the time resolution in the order of 1.5 ns, but high GEM voltage were needed due to the low Townsend coefficient. By adding Ar, Xe or CO₂, the Townsend coefficient was increased. Gas mixtures such as Xe-C₅H₁₂ and Ar/Xe-C₄H₁₀ (20-80) were promising with an intrinsic time resolution below 2 ns and having reasonable Townsend coefficients. Based on the cluster density, the C₃F₈ and C₂F₆ gases were promising to improve the time resolution but due to their high attachment coefficient, very low gains were observed and therefore are not suitable. On the other hand, CF₄ is proven to be a gas with excellent properties such as Townsend coefficient, drift velocity and attachment. It can be used as a standalone gas or used in composition with, for example, C₅H₁₂, yielding a time resolution in the order of 1-1.2 ns. Further investigation needs to be done to reduce the amount of CF₄ because it is a strong greenhouse gas.

Afterwards, non-ideal circumstances such as the GEM drift region thickness, the muon energy and the incident angle were investigated. A small dependence of σ_z^I on the drift region thickness was observed with gases having low cluster densities whereas the dependence on the muon energy was found to be negligible. The incident angle clearly influences the spread σ_z^I because non-perpendicularly incident muons leave a larger ionization track length in the drift region, hence decreasing the value of σ_z^I . However, large incident angles tend to spread out the primary ionization in the transverse direction, yielding a degradation of the spatial resolution and the charge collected on the readout strips.

7.2 Outlook

In this study, the intrinsic time resolution was taken as a reference to compare different gas mixtures and to optimize the time resolution of GEMs. This concept does not take any electronic equipment into account, as well as gain and diffusion variations were neglected. It is clear that the intrinsic time resolution must be compared to experimental results and the algorithm deduced in this chapter must be verified.

In the first instance, the time resolution as a function of the electric field in the drift region must be measured and compared to the algorithm. At the optimal drift field value, a minimum of the time resolution must be visible which corresponds maximized drift velocity in the drift region. The electronics used to extract the time resolution must be optimized and the threshold value must be as low as possible. Furthermore, the time resolution as a function of the GEM voltage (or gain) and the induction field can be studied, which was not completely incorporated in the algorithm. In the next step, the measurement of the time resolution must be executed (under ideal circumstances) with different gas mixtures in order to study the behavior of the cluster density. Because the time jitter due to primary ionization is the dominant effect on the time resolution, it is expected that the same ordering is experimentally obtained as the ordering of the time resolution in Tables 6.3 and 6.5 (i.e. gases with a high cluster density will result in a lower time resolution).

After comparing experimental time resolutions with the intrinsic time resolutions, it is useful to separate the intrinsic and the contribution of electronic time resolution (i.e. $\sigma_{t,i}$ and $\sigma_{t,e}$ respectively). This can be achieved by considering two GEM configurations (e.g. with two gas mixtures or with different voltages), which have the same electronics. In both configurations, the intrinsic time resolution is determined, denoted as $\sigma_{t,i,1}$ and $\sigma_{t,i,2}$, with the algorithm in chapter 6. Again, the intrinsic time resolution is identified with σ_t^I as defined in Eq. 6.1. Furthermore, the time resolutions for both configurations, $\sigma_{t,1}$ and $\sigma_{t,2}$, are measured. In this measurement, the GEM voltage must be adjusted in order to have the same effective gain for both configurations. By using Eq. 6.3, one obtains a system of two equations which can be solved to the electronic time resolution $\sigma_{t,e}$:

$$\sigma_{t,1} = \sqrt{\sigma_{t,e}^2 + \sigma_{t,i,1}^2}, \quad (7.1)$$

$$\sigma_{t,2} = \sqrt{\sigma_{t,e}^2 + \sigma_{t,i,2}^2}. \quad (7.2)$$

In this way, the intrinsic time resolution is scaled to the total time resolution with a value of the electronic time resolution. Because both configurations are measured with the same gain, the gain fluctuations are constant and incorporated in $\sigma_{t,e}$.

Besides the proposed experimental measurements and tests, a lot of other research can be performed by experiment such as:

- the influence on the angle of the incident muons by rotating the GEM detector in a muon beam,
- the influence on the muon energy and investigation with other charged particles and
- optimization of the GEM voltage and induction voltage.

Accordingly, further improvements of the simulations are needed and the following items needed to be investigated with regard to the time resolution:

- more accurate description of the time resolution taking gain and diffusion variations into account, independent of the electronics,
- detailed study on how to reduce the gain and diffusion variations and
- investigation of new and/or more complex gas mixtures.

Appendix A

Single GEM ANSYS input file

In this appendix the ANSYS input file is briefly described for a single GEM. Only the important instructions are explained in detail, other commands can be found in the ANSYS user manual. The dimensions and boundary conditions used are given in the code where the values must be entered in mm. In the text file, comments are preceded by the ! sign.

The file is initialized by the following instructions to clear the current session and to initialize a new session:

```
FINISH
/CLEAR,START
/PREP7
/PMETH,OFF,1 ! No polynomial elements

! Set electric preferences
KEYW,PR_ELMAG,1
KEYW,MAGELC,1
```

The FEM mesh must be set to the 10-tetrahedron:

```
ET,1,SOLID123 ! Select element
```

To make the code more readable, we first define some variables containing the dimensions and coordinates of the GEM geometry:

```
pitch = 0.14
kapton = 0.05
metal = 0.005
outdia = 0.07
middia = 0.05
rim = 0.08
drift = 2 ! 2 mm drift region
induct = 1 ! 1 mm induct region
totalth = drift + induct + 2*metal + kapton ! total thickness
```

However, the values of the drift, induction, metal and kapton thicknesses will be directly used rather than using the variables. In the next step, four materials are defined with their permittivity values:

```
! Material properties
MP, PERX, 1, 1e10 ! metal
MP, RSVX, 1, 0.0 ! set metal resistance to zero
MP, PERX, 2, 1.0 ! gas = vacuum
MP, PERX, 3, 4.0 ! kapton
```

In the next steps, the GEM geometry is defined. As described in chapter 4, four rectangular volumes are created with the BLOCK, x0, x1, y0, y1, z0, z1 instruction:

```
! GEM LAYER 1
BLOCK, 0, 0.14/2, 0, sqrt(3)*0.14/2, 2, 2.005 ! volume 1
BLOCK, 0, 0.14/2, 0, sqrt(3)*0.14/2, 2.005, 2.055 ! volume 2
BLOCK, 0, 0.14/2, 0, sqrt(3)*0.14/2, 2.055, 2.06 ! volume 3

! TOTAL GAS GAP
BLOCK, 0, 0.14/2, 0, sqrt(3)*0.14/2, 0, 3.06 ! volume 4
```

When volumes are created, each volume acquires an unique ID. This number is the lowest available number, starting from 1. As a result, the previous step generates four volumes with IDs 1 to 4. The volumes 1 to 3 representing the metal-kapton-metal layer, are shown in Fig. 4.2(a). In the next step, the double-conical cut-out pieces are generated. With the command WPOFFS, x0, y0, z0, the origin is moved to the given coordinates. To make the cut-out pieces, we move the origin to the midpoint of the hole, i.e. at $z = 2.03$. Afterwards, two cones and cylinders are generated with the CONE and CYL4 instructions respectively:

```
! Make cut-out pieces in layer 1 at x=y=0
WPOFFS, 0, 0, 2.03 ! set z offset to middle of kapton layer
CONE, outdia/2, middia/2, -kapton/2, 0, 0, 360 ! volume 5
CONE, middia/2, outdia/2, 0, kapton/2, 0, 0, 360 ! volume 6
WPOFFS, 0, 0, kapton/2 ! set z offset to end of kapton layer
CYL4, 0, 0, rim/2, ,, , metal ! volume 7
WPOFFS, 0, 0, -kapton ! set z offset to beginning of kapton layer
CYL4, 0, 0, rim/2, ,, , -metal ! volume 8
WPOFFS, 0, 0, kapton/2
WPOFFS, 0, 0, -2.03 ! return z offset to beginning
VADD, 5, 6, 7, 8 ! combine volumes to volume 9 and delete 5, 6, 7, 8
```

At the end, the VADD instruction is called to merge all the created volumes and create a new merged volume. The existing volumes 5, 6, 7 and 8 will be deleted and these IDs become free. The same cones and cylinders must be made for the other GEM hole at the opposite side of the unit cell. This will create volumes 10, where 5, 6, 7 and 8 are again becomes available. Volume 9 and 10 are shown in Fig. 4.2(b). In the next step, volumes 9 and 10 must be subtracted from the metal-kapton-metal layer volumes 1 to 3:

```
VSBV, 1, 9, , DELETE, KEEP ! 1 - 9, keep 9 and vol. 1 becomes 5
VSBV, 5, 10, , DELETE, KEEP ! 5 - 10, keep 10 and vol. 5 becomes 1
VSBV, 2, 9, , DELETE, KEEP ! 2 - 9, keep 9 and vol. 2 becomes 5
VSBV, 5, 10, , DELETE, KEEP ! 5 - 10, keep 10 and vol. 5 becomes 2
VSBV, 3, 9, , DELETE, DELETE ! 3 - 9, keep 9 and vol. 3 becomes 5
VSBV, 5, 10, , DELETE, DELETE ! 5 - 10, keep 10 and vol. 5 becomes 3
```

At the end of this sequence, no volume IDs are changed. The result after subtraction is shown in Fig. 4.2(c). Analogue, the volumes 1, 2 and 3 are subtracted from the gas. This new volume, shown in Fig. 4.3 will have ID no. 7 and the other volumes 4 to 6 are deleted. The empty volumes are then removed and volume 7 becomes volume 4:

```
! Subtract the kapton and metal from the gas
VSBV, 4, 1, , KEEP, KEEP ! 4 - 1, vol. 4 becomes 5
VSBV, 5, 2, , KEEP, KEEP ! 5 - 2, vol. 5 becomes 6
VSBV, 6, 3, , KEEP, KEEP ! 6 - 3, vol. 6 becomes 7
VDEL, 4
VDEL, 5
VDEL, 6
NUMCMP, VOLU ! delete empty volumes: vol. 7 becomes 4
```

Up to now, we have volume 1, 2 and 3 as the metal-kapton-metal layer and volume 4 as the total gas volume with the metal-kapton-metal layer removed.

In the next step, the metal-kapton-metal layer are glued, i.e. fusing the boundary planes. The fusion of the metal-kapton-metal layer with the gas gap is already done with the subtraction. Furthermore the different volumes are painted:

```
! Gluing the pieces metal-kapton-metal
VGLUE, 1, 2 ! becomes
VGLUE, 5, 3

! Paint the pieces
/COLOR, VOLU, RED, 4 ! gas
/COLOR, VOLU, BLACK, 1 ! metal
/COLOR, VOLU, ORANGE, 2 ! kapton
/COLOR, VOLU, BLACK, 3 ! metal
```

Before solving the potential, the volumes must be assigned to the materials:

```
! Assign materials
VSEL, S, , , 4 ! select volume 4
VATT, 2, , 1 ! assign material no. 2
VSEL, S, , , 1 ! select volume 1
VATT, 1, , 1 ! assign material no. 1
VSEL, S, , , 2 ! select volume 2
VATT, 3, , 1 ! assign material no. 3
VSEL, S, , , 3 ! select volume 3
VATT, 1, , 1 ! assign material no. 1
```

Furthermore, the voltage boundary conditions on the anode, cathode and GEM electrodes must be defined. Because the GEM metal electrodes can be treated as perfect conductors, the total surface must be an equipotential surface and all the surfaces must be assigned to the same potential:

```
! Voltage boundaries on the drift and induction plane
ASEL, S, LOC, Z, 0 ! select the cathode plane
DA, ALL, VOLT, 0 ! cathode zero potential (i.e. grounded)
ASEL, S, LOC, Z, 3.06 ! select the anode plane
DA, ALL, VOLT, 1300 ! anode potential to 1300 V

! Voltage boundary condition on the metal (layer: 1)
VSEL, S, , , 1 ! select volume top metal
ASLV, S ! select all the surfaces of the selected volume
DA, ALL, VOLT, 400 ! set potential to 400
VSEL, S, , , 3 ! select volume top metal
ASLV, S ! select all the surfaces of the selected volume
DA, ALL, VOLT, 900 ! set potential to 900
```

The last step before computing the potential is applying the periodic boundary conditions. Each plane in x and y direction of the gas and kapton volume must be assigned to such a boundary condition, except for the metal volumes which already was defined to be a perfect conductor and ANSYS takes this boundary condition into account.

```
! Symmetric boundary conditions on the sides: GAS
VSEL, S, , , 4 ! select the gas volume
ASLV, S ! select all the the surfaces of the selected volume
ASEL, R, LOC, X, 0 ! select plane at x=0
DA, ALL, SYMM ! set boundary condition for this plane
VSEL, S, , , 4 ! select the gas volume
ASLV, S ! select all the the surfaces of the selected volume
ASEL, R, LOC, X, 0.14/2 ! select plane at x=0.14/2
DA, ALL, SYMM ! set boundary condition for this plane
VSEL, S, , , 4 ! select the gas volume
ASLV, S ! select all the the surfaces of the selected volume
ASEL, R, LOC, Y, 0 ! select plane at y=0
DA, ALL, SYMM ! set boundary condition for this plane
VSEL, S, , , 4 ! select the gas volume
ASLV, S ! select all the the surfaces of the selected volume
ASEL, R, LOC, Y, sqrt(3)*0.14/2 ! select plane at y=sqrt(3)*0.14/2
DA, ALL, SYMM ! set boundary condition for this plane
```

```

! Symmetric boundary conditions on the sides: KAPTON (layer: 1)
VSEL, S, , , 2
ASLV, S
ASEL, R, LOC, X, 0
DA, ALL, SYMM
VSEL, S, , , 2
ASLV, S
ASEL, R, LOC, X, 0.14/2
DA, ALL, SYMM
VSEL, S, , , 2
ASLV, S
ASEL, R, LOC, Y, 0
DA, ALL, SYMM
VSEL, S, , , 2
ASLV, S
ASEL, R, LOC, Y, sqrt(3)*0.14/2
DA, ALL, SYMM

```

In a last step, the ga volume must be mesued and the field can be solved and displayed:

```

! Meshing options
VSEL, S,,, 1, 4
ASLV, S
MSHKEY,0
SMRT, 1
VSEL, S, , , 4
VSEL, A, , , 2
VMESH, ALL

! Solve the field
/SOLU
SOLVE
FINISH

! Display the solution
/POST1
/EFACET, 1
PLNSOL, VOLT, , 0

```

The nodal solutions and coordinates, the FEM elements and materials are written to text files, which can be imported into Garfield++:

```

! Write the solution to files
/OUTPUT, PRNSOL, lis ! save potential solution in PRNSOL.lis
PRNSOL
/OUTPUT
/OUTPUT, NLIST, lis ! save node coordinates in NLIST.lis
NLIST,,,,COORD
/OUTPUT
/OUTPUT, ELIST, lis ! save mapping FEM elements in ELIST.lis
ELIST
/OUTPUT
/OUTPUT, MPLIST, lis ! save materials in MPLIST.lis
MPLIST
/OUTPUT

```

Appendix B

Source code

Different programs are written in C++ based on the Garfield++ and ROOT classes. The source code can be found on GitHub: <http://github.com/jeyserma/GEMSimulations>. The different files stored in this repository are briefly explained below.

ANSYS

This directory contains the files for the ANSYS file generator which generates the necessary files to import in ANSYS and Garfield++. The code is written in HTML/PHP and two files are available. The first file, `index.php`, contains the input fields and the layout. After processing, the dimensions and values are stored in the `$GEM` array which is sent to the second file `multiGEM.php`. This file is the actual core and generates the ANSYS code from the values in the `$GEM` array. Additional code for the calculation of the weighting fields is also incorporated. The ANSYS code is saved to `output/GEM.inp`. Two additional files are created in this folder, `volumes.txt` and `geometry.txt`, which respectively contains a list of the ANSYS volumes and a list of the geometry and potentials. The latter file can be imported in Garfield++ which will be discussed later on.

GEMSimulation

The main program calculates the GEM from incident muons or other particles (except photons). For each GEM needed to be calculated, a directory must be made in the `includes/` folder. In this directory, the six ANSYS files as well as the `volumes.txt` and the `geometry.txt` files must be present. The name of this directory must be given in the program and is saved in the `filename` string. With the function `loadGEMconfig(std::string filename, struct GEMConfig gem)`, the `geometry.txt` is parsed and loaded into the `gem` struct. The GEM dimensions and electrostatics are then easily accessible from this structure.

The information of every muon which is simulated, is stored in the `particle` struct. It contains the energy, position and initial direction information as well as an array of `cluster` structs. Indeed, every cluster is stored in this array, which contains all the information such as position, energy transfer, amount of primary electrons, etc.

The information of every created electron and ion is saved in the `avalancheE` and `avalancheI` structs respectively. All the available information is stored such as initial/final position, energy and time of the electrons and ions.

At the end of the program, the structs are written to a ROOT file which is afterwards accessible to analyze. For each event, the induced pulse is also written to the file, and optionally the convoluted pulse with the VFAT3 transfer function.

clusterDensity

The scripts in this folder calculate the cluster density λ^{-1} as a function of the gas mixture and the muon energy. Although this quantity is independent of the electric field and dimensions of the active medium, an active medium is needed by Garfield++ and a solid rectangular box is created with an electric field of 100 V/cm in the x direction. Muons are perpendicularly incident in the x direction with different energies. In each step, the cluster density is calculated by HEED and stored in a **TGraph** object. Afterwards, the cluster density is plotted as a function of the muon energy and is saved to disk.

gasTable

The file `gasTable.c` calculates the gas table for a given gas mixture. Garfield++ invokes the Magboltz program which calculates the gas table. The results are stored in a `.gas` file, which can be imported in Garfield++ afterwards. However, the extraction of the Townsend, attachment and diffusion coefficients from the `.gas` file is not working properly. The solution is to extract the parameters from the program output generated by Garfield++ and Magboltz. This program output must be written to a file, and contains all the information of the calculation and the parameters. The parameters are extracted with the scripts available in the `plotGasTable`, which does not need to be compiled but is directly processed with ROOT. The output is a `.root` file which contains the five plots: the drift velocity, Townsend, longitudinal, transverse diffusion and attachment coefficient as a function of the electric field. Furthermore, each plot is saved to disk in pdf format.

primaryIonization

This script calculates the last cluster spread σ_z^I where the gas mixture, initial muon energy and incident angle must be given. It also requires the ANSYS files for the to be simulated GEM. The cluster positions are stored in an array, which is sorted at the end of the program. The last cluster is stored in a **TGraph** object from where the RMS value can be extracted.

singlePrimaryElectron

In chapter 6, the induced pulse for single primary electrons was investigated. The pulse was obtained by using this script, where the primary electron coordinates must be manually inserted in an array. Afterwards, the primary electrons are simultaneously simulated and all the information as described in the GEMSimulation section is stored in a ROOT file.

gain

This program simulates the single GEMs to calculate the gain. As described in chapter 5, the primary electrons were randomly generated in the drift region of the unit cell. Hence, no `particle` and `cluster` structs are needed. Again, all the information of the electrons and ions is stored `avalancheE` and `avalancheI` structs, which is saved afterwards to a ROOT file.

Appendix C

Drift velocities of used gases

The following plots shows the drift velocity as a function of the electric field for the gas mixtures used in chapter 6. Only the low electric field region is plotted in order to determine the local maximum drift velocity, needed to optimize the time resolution.

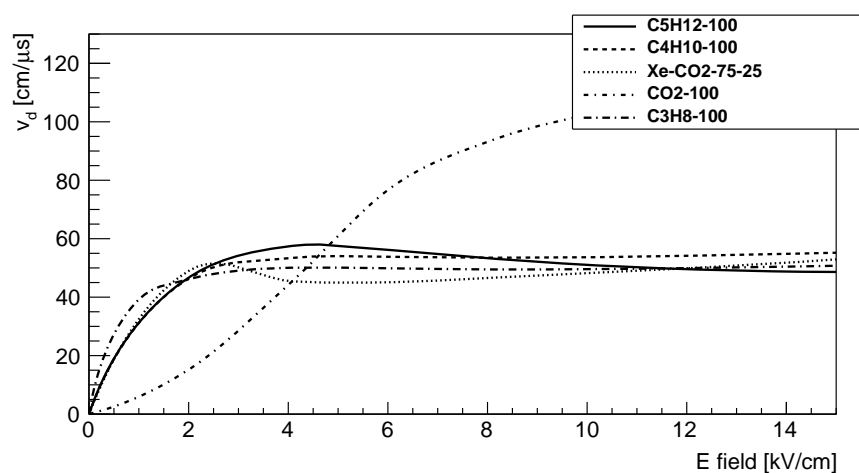


Figure C.1

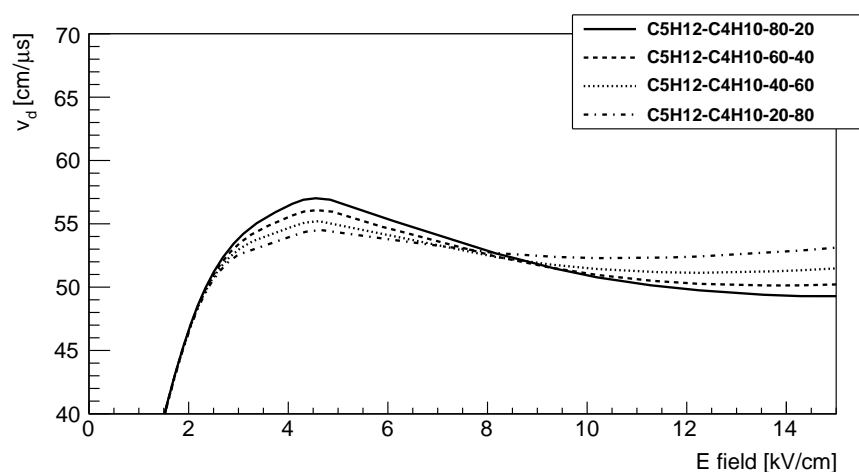


Figure C.2

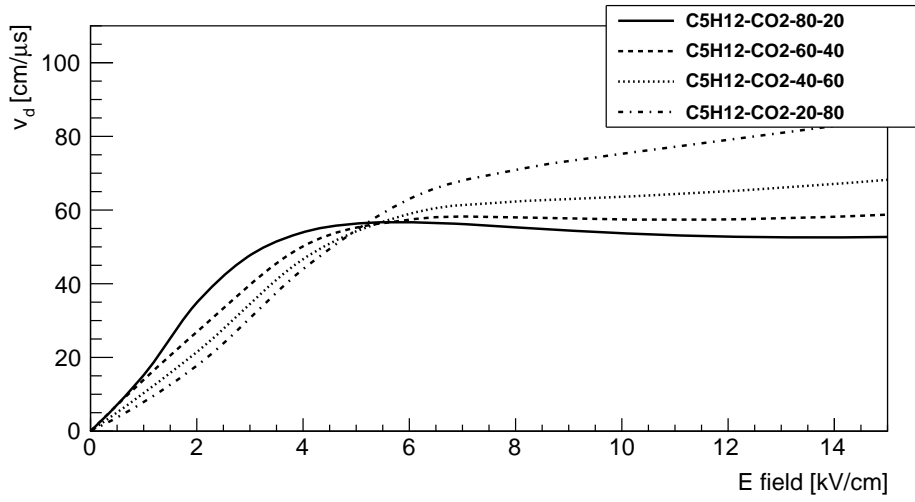


Figure C.3

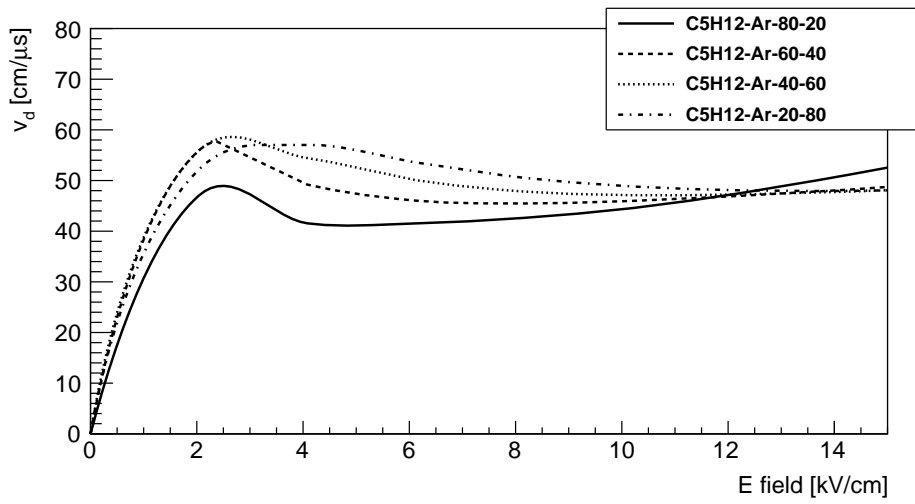


Figure C.4

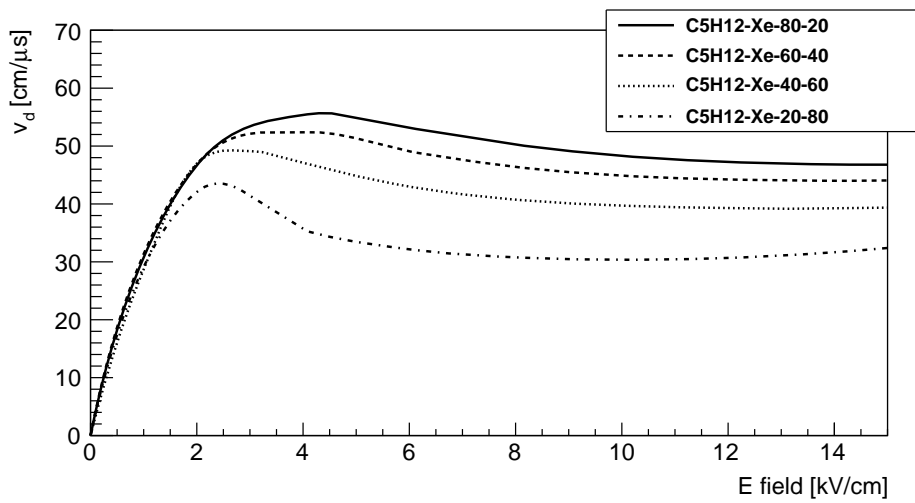


Figure C.5

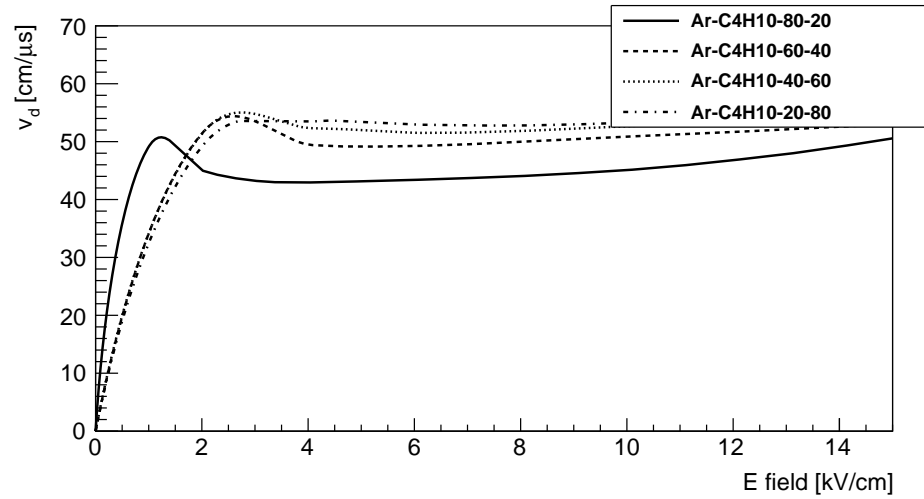


Figure C.6

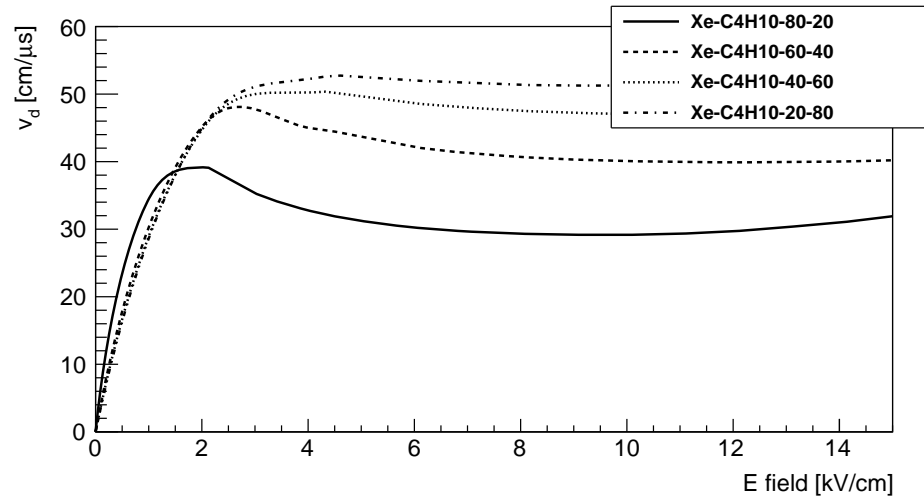


Figure C.7

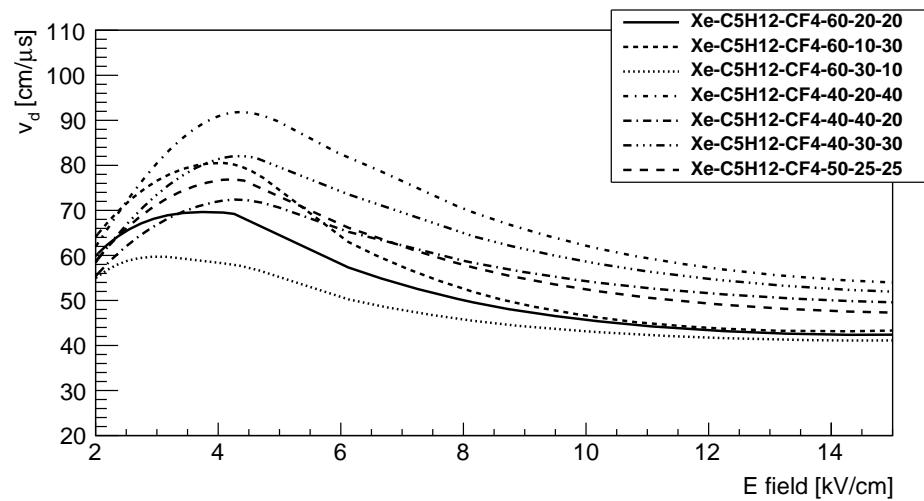


Figure C.8

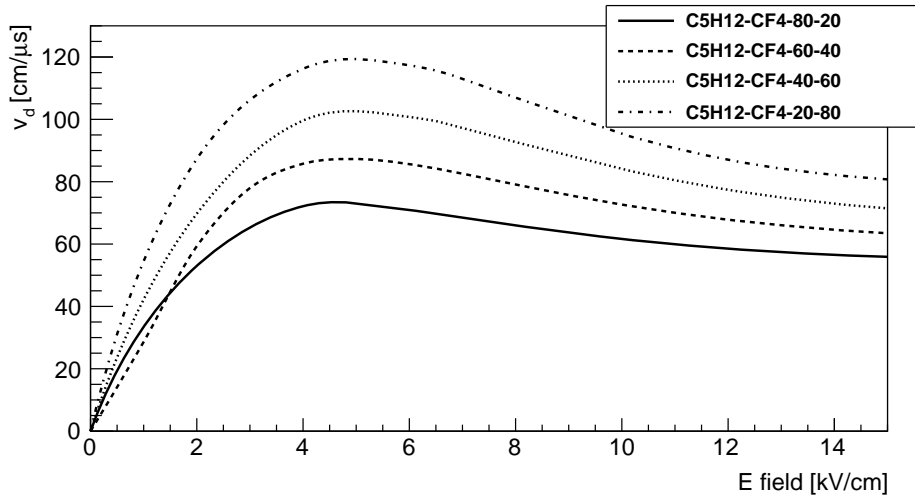


Figure C.9

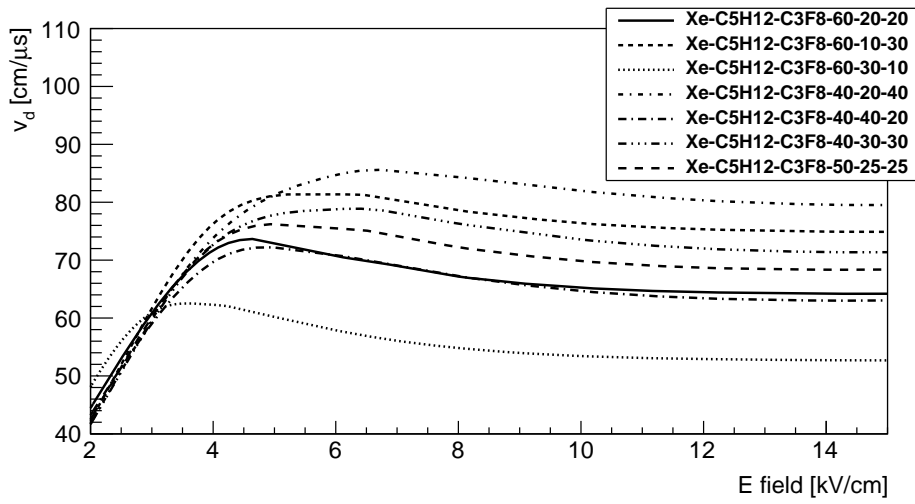


Figure C.10

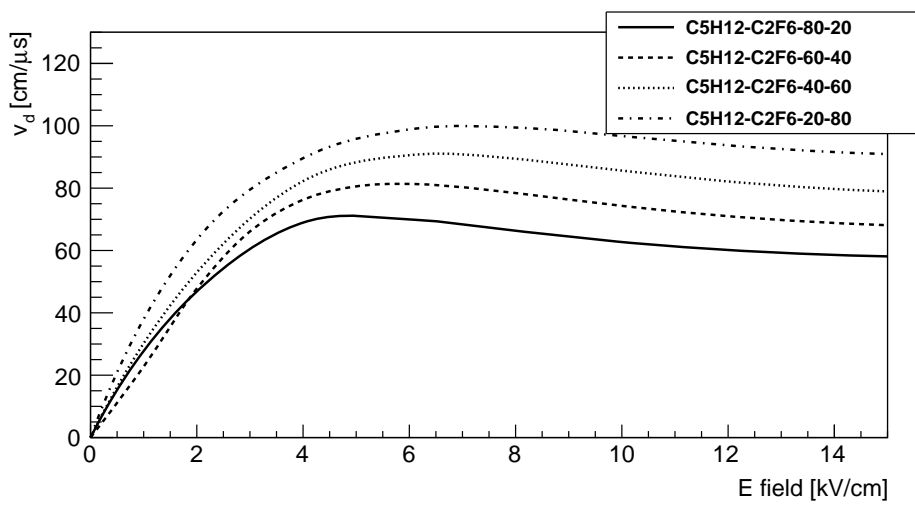


Figure C.11

Bibliography

- [1] C. Collaboration, *The CMS muon project: Technical Design Report*. Technical Design Report CMS, Geneva: CERN, 1997.
- [2] J. Moromisato and D. Garelick, “A spark chamber with improved time resolution,” *Nuclear Instruments and Methods*, vol. 101, no. 2, pp. 397 – 399, 1972.
- [3] F. Flakus, “Detection and measuring ionizing radiation – a short history,” *IAEA bulletin*, vol. 23, no. 4.
- [4] C. Lefevre, “LHC: the guide.” Jan 2008.
- [5] T. Sakuma, “3d sketchup images of the cms detector,” 2012. [Online; accessed 12-October-2013].
- [6] D. Abbaneo, M. Abbrescia, M. A. Akl, C. Armaingaud, P. Aspell, Y. Assran, S. Bally, Y. Ban, S. Banerjee, P. Barria, L. Benussi, V. Bhopatkar, S. Bianco, J. Bos, O. Bouhali, J. Cai, C. Calabria, A. Castaneda, S. Cauwenbergh, A. Celik, J. Christiansen, S. Colafranceschi, A. Colaleo, A. C. Garcia, G. D. Lentdecker, R. D. Oliveira, G. de Robertis, S. Dildick, S. Ferry, W. Flanagan, J. Gilmore, A. Gutierrez, K. Hoepfner, M. Hohlmann, T. Kamon, P. E. Karchin, V. Khotilovich, S. Krutelyov, F. Loddo, T. Maerschalk, G. Magazzu, M. Maggi, Y. Maghrbi, A. Marchioro, A. Marinov, N. Mazumdar, J. A. Merlin, S. Mukhopadhyay, S. Nuzzo, E. Oliveri, B. Philipps, D. Piccolo, H. Postema, A. Radi, R. Radogna, G. Raffone, A. Ranieri, A. Rodrigues, L. Ropelewski, A. Safonov, A. Sakharov, S. Salva, G. Saviano, A. Sharma, A. Tatarinov, H. Teng, N. Turini, J. Twigg, M. Tytgat, M. van Stenis, E. Verhagen, Y. Yang, N. Zaganidis, and F. Zenoni, “Studies on the upgrade of the muon system in the forward region of the cms experiment at lhc with gems,” *Journal of Instrumentation*, vol. 9, no. 01, p. C01053, 2014.
- [7] W. Blum, W. Riegler, and L. Rolandi, *Particle Detection with drift Chambers; 2nd ed.* Berlin: Springer, 2008.
- [8] G. F. Knoll, *Radiation detection and measurement; 4th ed.* New York, NY: Wiley, 2010.
- [9] D. E. Groom, N. V. Mokhov, and S. I. Striganov, “Muon stopping power and range tables 10-MeV to 100-TeV,” *Atom.Data Nucl.Data Tabl.*, vol. 78, pp. 183–356, 2001.
- [10] W. Allison and J. Cobb, “Relativistic Charged Particle Identification by Energy Loss,” *Ann.Rev.Nucl.Part.Sci.*, vol. 30, pp. 253–298, 1980.
- [11] G. L. T. Rita G. Lerner, *Encyclopedia of Physics, 2 Volumes, 3rd Edition*. Wiley, 2005.
- [12] G. Alkharov, “Statistics of electron avalanches and ultimate resolution of proportional counters,” *Nucl.Instrum.Meth.*, vol. 89, pp. 155–165, 1970.
- [13] F.Sauli, “Gem: A new concept for electron amplification in gas detectors,” *Nucl. Instrum. Methods Phys. Res., A*, vol. 386, no. CERN-EP-2000-031. CERN-SL-2000-008-EA. 1-2, pp. 531–534, 1997.

- [14] F. Sauli, “Development and applications of gas electron multiplier detectors,” *Nuclear Instruments and Methods in Physics Research Section A: Accelerators, Spectrometers, Detectors and Associated Equipment*, vol. 505, no. 1–2, pp. 195 – 198, 2003. Proceedings of the tenth Symposium on Radiation Measurements and Applications.
- [15] R. Bouclier, W. Dominik, M. Hoch, J.-C. Labbé, G. Million, L. Ropelewski, F. Sauli, A. Sharma, and G. Manzin, “New observations with the gas electron multiplier (gem),” *Nuclear Instruments and Methods in Physics Research Section A: Accelerators, Spectrometers, Detectors and Associated Equipment*, vol. 396, no. 1–2, pp. 50 – 66, 1997.
- [16] M. M. A. Chowdhury, *GEM: A comparison of Single and Double mask GEMs*. PHD thesis, 2011.
- [17] S. Duarte Pinto, M. Villa, M. Alfonsi, I. Brock, G. Croci, *et al.*, “Progress on large area GEMs,” *JINST*, vol. 4, p. P12009, 2009.
- [18] D. Abbaneo, S. Bally, H. Postema, A. Conde Garcia, J. Chatelain, *et al.*, “Characterization of GEM Detectors for Application in the CMS Muon Detection System,” *IEEE Nucl.Sci.Symp.Conf.Rec.*, vol. 2010, pp. 1416–1422, 2010.
- [19] D. Abbaneo, M. Abbrescia, M. A. Akl, C. Argamaingaud, P. Aspell, Y. Assran, S. Bally, Y. Ban, P. Barria, L. Benussi, V. Bhopatkar, S. Bianco, J. Bos, O. Bouhali, J. Cai, C. Calabria, A. Castaneda, S. Cauwenbergh, A. Celik, J. Christiansen, S. Colafranceschi, A. Colaleo, A. C. Garcia, G. D. Lentdecker, R. D. Oliveira, G. de Robertis, S. Dildick, S. Ferry, W. Flanagan, J. Gilmore, A. Gutierrez, K. Hoepfner, M. Hohlmann, T. Kamon, P. E. Karchin, V. Khotilovich, S. Krutelyov, F. Loddo, T. Maerschalk, G. Magazzu, M. Maggi, Y. Maghrbi, A. Marchioro, A. Marinov, J. A. Merlin, S. Nuzzo, E. Oliveri, B. Philipps, D. Piccolo, H. Postema, A. Radi, R. Radogna, G. Raffone, A. Ranieri, A. Rodrigues, L. Ropelewski, A. Safonov, A. Sakharov, S. Salva, G. Saviano, A. Sharma, A. Tatarinov, H. Teng, N. Turini, J. Twigger, M. Tytgat, M. van Stenis, E. Verhagen, Y. Yang, N. Zaganidis, and F. Zenoni, “Development and performance of large scale triple gem for cms,” *Journal of Instrumentation*, vol. 8, no. 11, p. C11017, 2013.
- [20] A. Breskin, A. Buzulutskov, R. Chechik, E. Shefer, and B. Singh, “Sealed gas uv-photon detector with a multi-gem multiplier,” *Nuclear Science, IEEE Transactions on*, vol. 48, pp. 417–420, Jun 2001.
- [21] ANSYS., “inc.” <http://ansys.com>. [Online; accessed 27-May-2012].
- [22] Garfield++, “.” <http://garfieldpp.web.cern.ch/garfieldpp>. [Online; accessed 27-May-2012].
- [23] ROOT, “.” <http://root.cern.ch>. [Online; accessed 27-May-2012].
- [24] Garfield, “.” <http://garfield.web.cern.ch/garfield/>. [Online; accessed 27-May-2012].
- [25] H. Schindler, “Garfield++ user guide,” 2014. [Online; accessed 8-May-2014].
- [26] I. Smirnov, “Modeling of ionization produced by fast charged particles in gases,” *Nuclear Instruments and Methods in Physics Research Section A: Accelerators, Spectrometers, Detectors and Associated Equipment*, vol. 554, no. 1–3, pp. 474 – 493, 2005.
- [27] S. Biagi, “Monte carlo simulation of electron drift and diffusion in counting gases under the influence of electric and magnetic fields,” *Nuclear Instruments and Methods in Physics Research Section A: Accelerators, Spectrometers, Detectors and Associated Equipment*, vol. 421, no. 1–2, pp. 234 – 240, 1999.

- [28] LXCAT, “.” http://fr.lxcat.net/data/set_type.php. [Online; accessed 27-May-2012].
- [29] T. Maerschalk, “.” [Private communication].
- [30] S. H. et al., “Energy resolution of a single gem detector,” *Journal of the Korean Physical Society*, vol. 55, no. 6, pp. 2366–2371, 2009.

